UAB
Universitat Autònoma de Barcelona

Solution-processing of organic semiconductors for achieving high mobility and reproducibility

LAMIAA FIHAJI

ADVERTIMENT. L'accés als continguts d'aquesta tesi queda condicionat a l'acceptació de les condicions d'ús establertes per la següent llicència Creative Commons: https://creativecommons.org/licenses/?lang=ca

ADVERTENCIA. El acceso a los contenidos de esta tesis queda condicionado a la aceptación de las condiciones de uso establecidas por la siguiente licencia Creative Commons: https://creativecommons.org/licenses/?lang=es

WARNING. The access to the contents of this doctoral thesis it is limited to the acceptance of the use conditions set by the following Creative Commons license: https://creativecommons.org/licenses/?lang=en

Solution-processing of organic semiconductors for achieving high mobility and reproducibility

LAMIAA FIJAHI

Doctoral Thesis

PhD Programme in Materials Science

Supervisor/Director: Prof. Marta Mas-Torrent

Molecular Nanoscience and Organic Materials (NANOMOL)

Institut de Ciència de Materials de Barcelona (ICMAB-CSIC)

September 2024

Acknowledgments

I would like to take this opportunity to express my heartfelt gratitude to all those who have contributed to the successful completion of this thesis.

First and foremost, I am deeply indebted to my thesis Supervisor, Prof. Marta Mas-Torrent, for your unwavering support, invaluable guidance, and mentorship throughout this journey. Your expertise, patience, kindness, and encouragement have been instrumental in shaping the direction of this research and enhancing my academic growth. Your support has been invaluable to me, and I am deeply grateful for your presence throughout my journey.

I would also like to express my gratitude to the faculty and staff of ICMAB for providing a stimulating academic environment and facilitating various resources that supported my research endeavors.I would like to acknowledge the financial support provided by UHMob Network, which made this research possible.

The work carried out in this thesis would not have been possible without collaborations with other research groups. Because of that, I would like to thank all the collaborators who have contributed to the research done in this thesis. Thanks to Prof. Roland Resel and Dr. Ann Maria James from the University of Graz and his group, for their collaboration in the study of the crystal structure of my organic thin films. Thanks Dr Esther Barrena, and Shunya Yan from ICMAB for the AFM measurements, thanks to Dr. Martina Volpi, Prof. Yves H. Geerts for providing some organic semiconductors and Dr. Marco Bardini and Prof. David Beljonne for providing DFT calculations.

I want to extend a special thank you to Dr. Adrian Tamayo for his support during my time in Barcelona. From the very beginning of my doctoral program, Dr.

Adrian Tamayo and Dr. Jinghai Li both of them have been consistently there for me. Our collaboration has not only led to a pleasant working experience but has also blossomed into a wonderful friendship. I already miss our interactions greatly and cherish the bond we've formed.

Also, I would like to thank the entire Nanomol group and eMolMat team: David Pina, Dr. Guillem Vargas, Dr.Jamila Jaafari, Dr.Samar Gharbi, Dr.Carme Martinez, Dr.Dean Kos, Jose Muñoz, Maria Jesus Ortiz, Maria Elisabetta Giglio, Min Zhang and all the members from Nanomol group. And special thanks to all the members of the UHMob network.

My deepest thanks go to my parents, my family back home, Montflorit Family, ICMAB Family and my good friends (Ghizlane, Mhaned, Zakaria, Cassandra, Mariel, and Jonathan...) for their constant encouragement, understanding, and patience during the challenging moments of this thesis journey. Their unwavering belief in my abilities has been a constant source of motivation.

In conclusion, this thesis would not have been possible without the collective support, encouragement, and inspiration from all those mentioned and countless others who have touched my life in various ways. I am truly grateful for their contributions, and I carry the lessons and experiences gained throughout this research with me as I embark on the next chapter of my academic and professional journey.

Abstract

This thesis explores various facets of organic field-effect transistors (OFETs) with a focus on their fabrication, electrical characterization, and applications within the field of organic electronics. The initial section highlights the widespread interest in organic electronics for its potential in low-cost and large-area applications, emphasizing the advantages of organic semiconductors (OSCs) deposited through solution-based techniques compatible with roll-to-roll processes. The significance of OSC film morphology and structure for device performance is underscored and OFETs have been identified as promising platforms for studying OSC transport properties.

Transitioning to the specific contributions of the thesis, the fabrication of OFETs using the bar-assisted meniscus shearing (BAMS) technique to deposit the OSCs has been the main focus of interest. This is a cost-effective printing method compatible with up-scaling that can provide large area crystalline films. In particular, Chapter 2 is based on the utilization of charge transfer complexes of a benzothienobenzothiophene derivative as active layer in OFETs, while Chapter 3 explores the processing of dinaphtho[2,3-*b*:2′,3′-*f*]thieno[3,2-*b*]thiophene (DNTT) derivatives. In both cases, the OSCs have been blended with polystyrene to enhance the solution processability, reduce charge traps and improve device mobility.

Moving forward, Chapter 4 delves into the investigation of the morphology and structure of evaporated and solution-processed thin films of the asymmetric OSC 2-decyl-7-phenyl[1] benzothieno[3,2-b][1]benzothiophene. Through modifications in coating parameters, solution formulations, and post-annealing treatments, a controlled formation of kinetic or thermodynamic polymorphs was achieved, resulting in an enhanced OFET performance.

Esta tesis explora varias facetas de los transistores orgánicos de efecto de campo

(OFETs) centrándose en su fabricación, caracterización eléctrica y aplicaciones dentro del campo de la electrónica orgánica. En el primer capítulo se destaca el amplio interés que existe en la electrónica orgánica por su potencial en aplicaciones de bajo costo y gran área, enfatizando las ventajas de los semiconductores orgánicos (OSC) depositados mediante técnicas basadas en soluciones compatibles con procesos de "roll-to-roll". Se remarca la influencia de la morfología y la estructura cristalina de las películas de OSC en el rendimiento de los dispositivos y se muestra como los OFETs son plataformas ideales para estudiar las propiedades de transporte de los OSC.

Las contribuciones más destacadas de la tesis se basan en la fabricación de OFETs utilizando la técnica de cizallamiento por menisco asistido por barra (BAMS) para depositar los OSC. Este es un método de impresión económico compatible con el escalado que puede proporcionar películas cristalinas de OSC recubrimiento grandes áreas. En particular, el Capítulo 2 se basa en la utilización de complejos de transferencia de carga de un derivado de benzotienobenzotiofeno como capa activa en OFETs, mientras que el Capítulo 3 explora el procesamiento de derivados de dinafto[2,3-b:2′,3′-f]tieno[3,2-b]tiofeno. En ambos casos, los OSC se han mezclado con poliestireno para mejorar la procesabilidad en solución, reducir las trampas de carga y aumentar la movilidad del dispositivo.

Finalmente, el Capítulo 4 profundiza en la investigación de la morfología y la estructura de películas delgadas del OSC asimétrico 2-decil-7-fenil[1]benzotieno[3,2-b][1]benzotiofeno evaporadas y procesadas en solución. A través de modificaciones en los parámetros de recubrimiento, las formulaciones de la solución y los tratamientos térmicos posteriores al procesado, se logró controlar la formación de polimorfos cinéticos o termodinámicos, dando lugar a OFETs con un mejor rendimiento.

La tesi explora diverses facetes dels transistors orgànics d'efecte de camp (OFETs) que van des de la seva fabricació, caracterització elèctrica i aplicacions dins del camp de l'electrònica orgànica. La secció inicial posa de manifest l'interès actual en l'electrònica orgànica per les seves aplicacions en dispositius de de baix cost i gran àrea, destacant les avantatges dels semiconductors orgànics (OSC) depositats mitjançant tècniques de processat en dissolució compatibles amb processos de "roll-to-roll". Es destaca la influència de la morfologia i l'estructura cristal·lina de les pel·lícules de OSC en el rendiment dels dispositius i es mostra com els OFETs són plataformes ideals per estudiar les propietats de transport dels OSC.

Les contribucions més destacades de la tesi es basen en la fabricació d'OFETs utilitzant la tècnica de cisalla per menisc assistit per una barra (BAMS) per depositar el OSC. Es tracta d'un mètode d'impressió econòmic compatible amb l'escalat i que pot proporcionar pel·lícules cristal·lines de OSC recubrint grans àrees. En particular, el Capítol 2 es basa en l'ús de complexes de transferència de càrrega d'un derivat de benzotienobenzotiofè com a capa activa en OFETs, mentre que el Capítol 3 explora el processament de derivats de dinafto[2,3-b:2′,3′-f]tieno[3,2-b]tiofè. En ambdós casos, els OSCs s'han barrejat amb poliestirè per millorar la processabilitat en solució, reduir les trampes de càrrega i augmentar la mobilitat del dispositiu.

Finalment, el Capítol 4 aprofundeix en la investigació de la morfologia i l'estructura de pel·lícules primes del OSC asimètric 2-decil-7-fenil[1]benzotieno[3,2-b][1]benzotiofè, tant evaporades com processades en solució. A través de modificacions en els paràmetres de recobriment, les formulacions de la solució i els tractaments tèrmics post-processat, es va aconseguir controlar la formació de polimorfs cinètics o termodinàmics, millorant el rendiment dels OFETs.

Publications included in this thesis

I. "Charge transfer complexes of a benzothienobenzothiophene derivative and their implementation as active layer in solution-processed thin film organic field-effect transistors."

Lamiaa Fijahi, Tommaso Salzillo, Adrian Tamayo, Marco Bardini, Christian Ruzie, Claudio Quarti, David Beljonne, Simone D'Agostino, Yves H. Geerts and Marta Mas-Torrent.
J. Mater. Chem. C, 2022, 10, 7319–7328

II. "High throughput processing of dinaphtho[2,3-b:2',3'-f]thieno[3,2-b]thiophene (DNTT) organic semiconductors."

Lamiaa Fijahi, Jinghai Li, Adrián Tamayo, Martina Volpi, Guillaume Schweicher, Yves H. Geerts and Marta Mas-Torrent.
Nanoscale, 2023,15, 230-236

III. "Enhancing charge transport in p-type organic semiconductors: the impact of post-annealing on evaporated Ph-BTBT-10."

Lamiaa Fijahi, Shunya Yan, Ann Maria James, Adrian Tamayo, Jinghai Li, Roland Resel, Esther Barrena, Marta Mas-Torrent, (Submitted).

Publications not included in this thesis

IV. "Synergistic effect of solvent vapour annealing and chemical doping for achieving high performance organic field-effect transistors with ideal electrical characteristics."

Jinghai Li, Adara Babuji, Lamiaa Fijahi, Ann Maria James, Roland Resel, Tommaso Salzillo, Raphael Pfattner, Carmen Ocal, Esther Barrena, Marta Mas-Torrent.
ACS Applied Materials & Interfaces, 2023, 15, 5521-5528

V. "From synthesis to device fabrication: elucidating the structural and electronic properties of C7-BTBT-C7."

Priya Pandey, Lamiaa Fijahi, Nemo McIntosh, Nicholas Turetta, Marco Bardini, Samuele Giannini, Christian Ruzié, Guillaume Schweicher, David Beljonne, Jérôme Cornil, Paolo Samorì, Marta Mas-Torrent, Yves Henri Geerts, Enrico Modena, Lucia Maini.
J. Mater. Chem. C, 2023, 11, 7345-7355

VI. "Impact of hydrophilic side chains on the thin film transistor performance of a benzothieno–benzothiophene derivative."

Mindaugas Gicevičius, Ann Maria James, Lukas Reicht, Nemo McIntosh, Alessandro Greco, Lamiaa Fijahi, Félix Devaux, Marta Mas-Torrent, Jérôme Cornil, Yves Henri Geerts, Egbert Zojer, Roland Resel and Henning Sirringhaus.
Mater. Adv, 2024,5, 6285-6294

Abbreviations

AFM	Atomic force microscopy
BAMS	Bar-assisted meniscus shearing
C_8-O-BTBT-O-C_8	2,7-Bis(4-octyloxyphenyl)[1]benzothieno[3,2-b][1]benzothiophene
C_8-BTBT	2,7-Dioctyl[1]benzothieno[3,2-b][1]benzothiophene
C_8-DNTT	2,9-Dioctylnaphtho[2,3- b]naphtha[2',3':4,5]thieno[2,3-d]thiophene
C_{10}-DNTT	2,9-Didecyldinaphtho[2,3- b:2',3'-f]thieno[3,2-b]thiophene
DB-TTF	Dibenzo-tetrathiafulvalene
diF-TES-ADT	2,8-difluoro-5,11bis (triethylsilylethynyl) anthradithiophene
F_4TCNQ	2,3,5,6-tetrafluoro-7,7,8,8-tetracyanoquinodimethane
HOMO	Highest occupied molecular orbital
KPFM	Kelvin probe force microscopy
LUMO	Lowest unoccupied molecular orbital
KPFM	Kelvin probe force microscopy
OFET	Organic field-effect transistor
OSC	Organic semiconductor
PFBT	Pentafluorobenzenethiol
Ph-BTBT-10	2-Decyl-7-phenyl[1]benzothieno[3,2-b][1]benzothiophene
PS	Polystyrene
SAM	Self-assembled monolayer
S-DNTT-10	dialkylated dinaphtho[2,1-b:2′,1′-f]thieno[3,2-b]thiophene
TGBC	Top-gate bottom-contact
TGTC	Top-gate top-contact
TIPS-Pn	6,13-Bis(triisopropylsilylethynyl) pentacene
TLM	Transfer-length method
ToF-SIMS	Time-of-flight secondary ion mass spectrometry

Symbols

C	Capacitance
Σ	Conductivity
E_F	Fermi energy
I_{off}	Off current
I_{on}	On current
I_D	Source-drain current
I_G	Source-gate current
L	Channel length
M	Field-effect mobility
N_t	Density of charge carrier traps
on/off	on/off current ratio (I_{on}/I_{off})
R_C	Contact resistance
R_{ch}	Channel resistance
SS	Subthreshold swing
V_{on}	Switch-on voltage
V_D	Source-drain voltage
V_G	Source-gate voltage
V_{th}	Threshold voltage
W	Channel width
E	Elementary charge
k_B	Boltzmann constant
E	Dielectric constant
P	Charge density in the semiconductor

Contents

Chapter 1: Introduction.....1

1.1 Organic Electronics 1

1.2 Organic semiconductors 3

1.3 Charge transport mechanisms 9

1.4 Organic semiconductors processing techniques.....14

1.4.1 Influence of the experimental parameters on the thin film properties during meniscus-guided coating.....18

1.4.2 Post-deposition annealing procedures.....22

1.5 Organic field-effect transistors (OFETs).....26

1.5.1. Operation principle.....26

1.5.2 Device geometries.....30

1.5.3 Electrical characterization and OFET parameters 31

1.6 Objectives.....43

1.7 References 44

Chapter 2: 49

Organic semiconductors based on charge transfer complexes of a BTBT derivative.....49

2.1 Introduction and Objectives 50

2.2 Summary of the results 54

2.3 Conclusions 57

2.4 References 58

Chapter 3: 62

High throughput printing of DNTT derivatives 62

3.1 Introduction and Objectives 64

3.2 Summary of the results 68

3.3 Conclusions 70

3.4 References 71

Chapter 4: 75

Crystal structure influence on the charge transport of Ph-BTBT-10 films 75

4.1 Introduction and Objectives 76

4.2 Summary of the results of the evaporated Ph-BTBT-10 films 79

4.3 Results on solution-processed Ph-BTBT-10 films 114

4.4 Conclusions 127

4.5 References 129

Chapter 5: Conclusions 131

Annex: Other contributions 134

Chapter 1: Introduction

1.1 Organic Electronics

Organic electronics is a field within modern electronics that focuses on the use of organic materials. like polymers or small molecules. These materials, which are carbon-based like living things, were traditionally considered excellent insulators for many technological applications. However, in 1862, Henry Letheby discovered a conductive material through anodic oxidation of aniline in sulfuric acid, marking the early understanding of electrical conduction in organic materials.[1]

In the 1970s, Heeger, MacDiarmid, and Shirakawa discovered that polyacetylene, when modified, could become conductive. This breakthrough, leading to the Nobel Prize in Chemistry in 2000,[2] laid the foundation for organic electronics. Over the next three decades, the field rapidly advanced, attracting physicists, chemists, and engineers, and transitioning from pure scientific inquiry to applied research.

In the mid-1980s, Tang and VanSlyke's work on organic light-emitting diodes (OLEDs) and Tsumura et al.'s presentation of the first organic solid-state field-effect transistor (OFET) marked significant milestones.[3] The introduction of vacuum sublimation methods for depositing thin films of semiconducting small molecules enabled further advancements. Nowadays, organic electronics have already made significant strides in various application areas (**Figure 1.1**). OLEDs have revolutionized display technology, offering vivid colors, high contrast ratios, and low power consumption compared to traditional liquid crystal displays (LCDs).[4] Organic photovoltaic (OPV) cells have emerged as a promising technology for solar energy harvesting, offering the potential for lightweight, flexible, and low-cost solar panels that can be integrated into buildings, vehicles,

and portable electronics.[5]

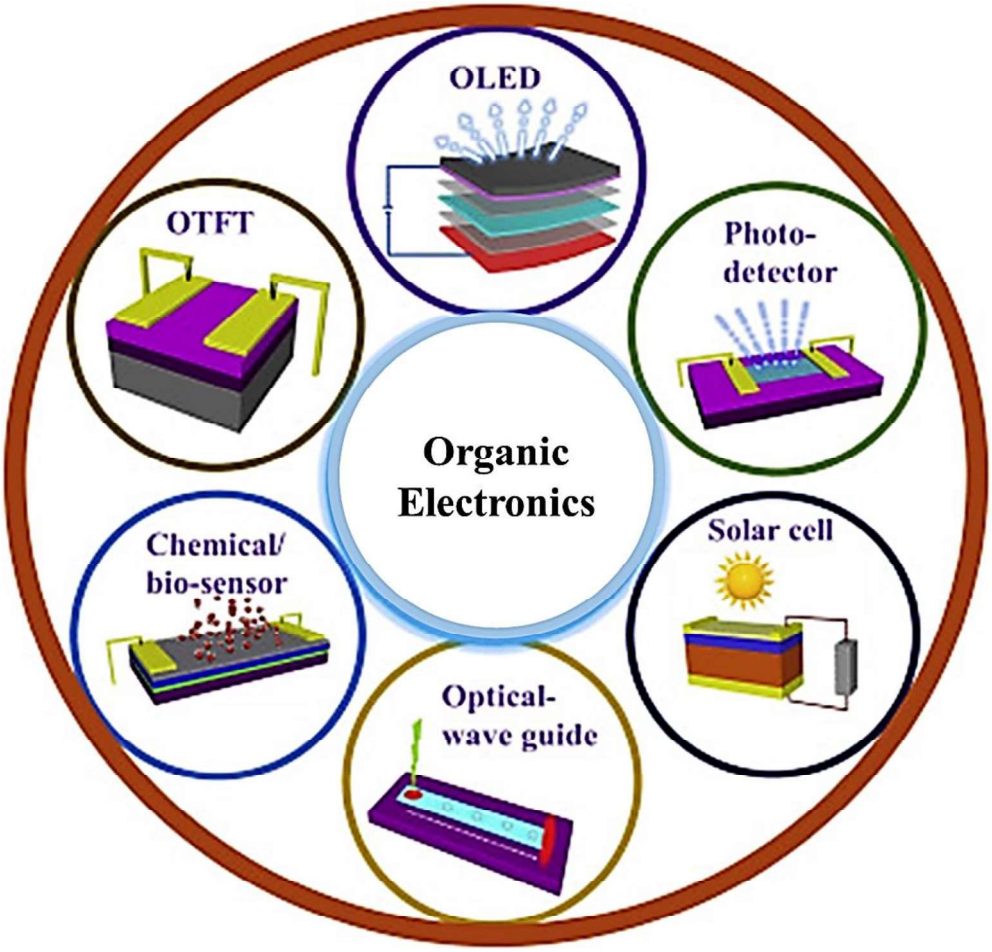


Figure 1.1. Applications of organic electronic devices. In the figure, OTFT stands for organic thin film transistor. Adapted from ref [6].

Organic field-effect transistors (OFETs) emerged in the late 1980s almost simultaneously with OLEDs. [7][8] Owing to their limited performance, OFETs are far from competing with silicon-based microelectronics. However, single-crystalline silicon is an expensive and brittle material. Commercial applications of OFETs can therefore be envisioned in fields where low cost is crucial, e.g., smart cards and electronic bar codes. In addition, organic electronics will

probably find their way into devices built on soft polymeric substrates. For example, applications like soft displays or an “electronic book” made of rewritable pages would constitute an attractive alternative to current computer displays.[9]

1.2 Organic semiconductors

Organic semiconductors (OSCs) represent a class of materials that have garnered significant attention in the field of electronics due to their unique properties and potential applications. Unlike traditional inorganic semiconductors like silicon, organic semiconductors are composed primarily of carbon-based molecules or polymers, but they can also contain other elements such as hydrogen, oxygen, nitrogen, and sulfur.

OSCs, whether molecular or polymeric, exhibit interesting optical and electronic properties, relying on the ability to move electrons through their π-conjugated structures, which consist of alternating single and double bonds that create a plane of sp^2 hybridized orbitals with the $2p_z$ orbitals perpendicular to that plane. These $2p_z$ orbitals overlap to form a network of π bonds that can move electrons across the plane of conjugation. In addition, if one forms a molecule from such carbon atoms in the sp^2 hybridization, the orbitals located in the plane can form bonds that have rotational symmetry along the line connecting the two atoms. These bonds are the so-called σ-bonds and are the strong covalent bonds in a molecule, as shown in **Figure 1.2 (a)**.

The impact of increasing the extent of conjugation on electronic properties can be well understood by the progression from ethylene to butadiene, octatetraene, and further, varying lengths of polyenes. As shown in **Figure 1.2(b)**, with an increasing number of overlapping $2p_z$ orbitals, there is a decrease in the energetic bandgap (E_g) between the highest-occupied molecular orbital (HOMO) and the

lowest-unoccupied molecular orbital (LUMO) of the system. The HOMO and LUMO energy levels can be visualized as the valence band (VB) and conduction band (CB) of inorganic semiconductors.

OSCs can be reduced or oxidized within an accessible potential. One can differentiate between three classes of OSCs by their polarity: p-type, n-type, and ambipolar OSCs. p-type OSCs typically consist of electron-donor molecules prone to easy oxidation, as a result of their high-energy HOMO level. The majority of p-type OSCs display a HOMO energy around -5.0 eV. Conversely, n-type OSCs comprise electron acceptor molecules that undergo reduction readily, with their LUMO energy levels generally around -4.0 eV. Lastly, ambipolar OSCs combine characteristics of both p-type and n-type materials. They show a low HOMO-LUMO band gap and can transport both holes and electrons.

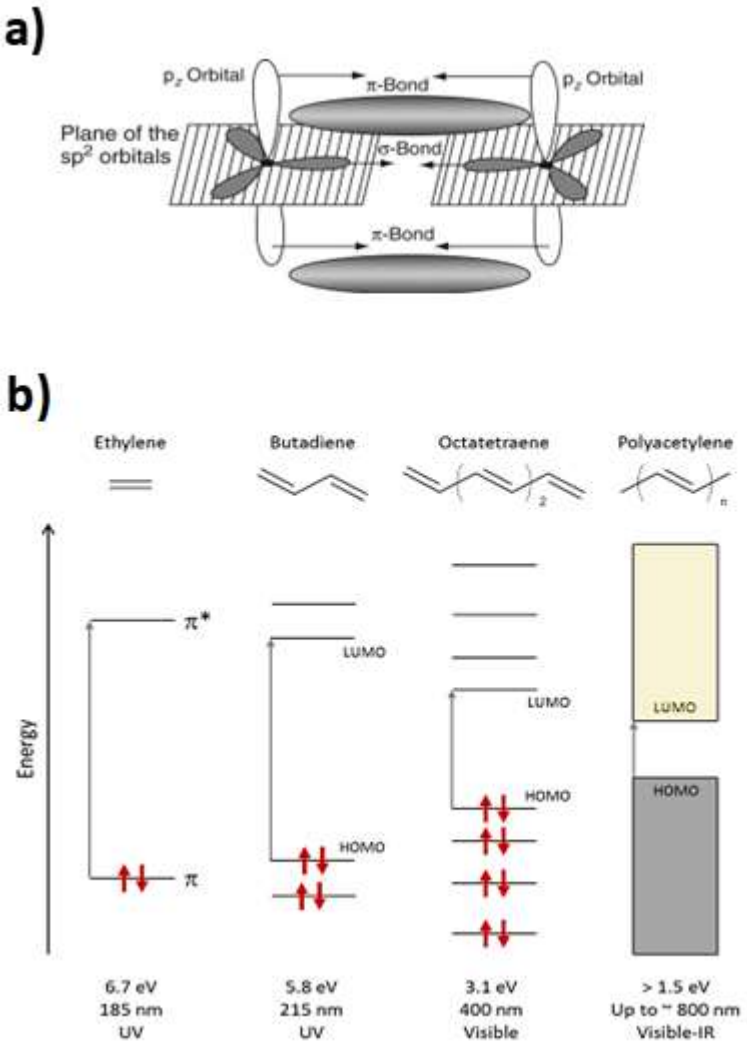


Figure 1.2 a) Bonding of two carbon atoms, with both σ- and π-bonds. b) Schematic of energy-level splitting and absorption in alkenes with increasing conjugation length, highlighting the lowest-energy optical transitions from HOMO to LUMO. The bandgap of polyacetylene depends on both the number of monomers n and the effective conjugation length in the polymer. Arrows represent spin-paired electrons. Reproduced from www.oe.phy.cam.ac.uk/research/materials/osemiconductors.html.

OSCs can be divided into two main categories: conjugated polymers and small conjugated molecules. Conjugated polymers comprise lengthy chains of electroactive and aromatic groups that are interconnected. Despite their high molecular weight, which renders them resistance to evaporation, conjugated polymers possess excellent solubility in organic solvents and demonstrate favorable film-forming properties, making them well-suited for solution processing applications. Inherent to conjugated polymer films is a significant degree of disorder, which hampers achieving efficient charge transport. Consequently, various post-treatment strategies have been devised to optimize the structural order and thin film morphology to enhance their electrical.[10] Poly(3-hexylthiophene) (P3HT) stands as one of the most extensively studied polymers for OFETs. Notably, P3HT exhibits a mobility of around 0.1 cm^2/V s,[11] highlighting its potential for electronic applications. Current research efforts continue to explore novel conjugated polymers and thin film processing methodologies to elucidate their full potential in electronic devices.

On the other hand, small molecule OSC materials exhibit a higher structural order compared to polymer OSCs, forming polycrystalline thin films or single crystals. Consequently, small molecule OSCs typically demonstrate greater field-effect mobility, with the best-reported values being around 10 $cm^2/V \cdot s$.[12], [13] Small molecule OSCs can be deposited through thermal evaporation or solution-based techniques. However, their solubility in common organic solvents is usually low. To address this, the conjugated rigid cores of the OSCs are often functionalized with side groups to enhance solubility without compromising structural order or transport properties. Some benchmark soluble small molecule OSCs used in this thesis include 2,9-dioctylnaphtho[2,3-b]naphtha[2′,3′:4,5]thieno[2,3-d]thiophene (C8-DNTT), 2,9-didecyldinaphtho[2,3-b:2′,3′-f]thieno[3,2-b]thiophene (C10-DNTT), 3,10-didecylnaphtho[2,1-

b]naphtha[1′,2′:4,5]thieno[2,3-d]thiophene (S-DNTT-10), 2,3,5,6-tetrafluoro-7,7,8,8-tetracyanoquinodimethane (F4-TCNQ), and the benzothiophene derivatives 2,7-bis(octyloxy)[1]benzothieno[3,2-b]-benzothiophene (C8O-BTBT-OC8), 2,7-dioctyl[1]benzothieno[3,2-b][1]benzothiophene (C8-BTBT), and 2-decyl-7-phenyl[1]benzothieno[3,2-b][1]benzothiophene (Ph-BTBT-10) **(Figure 1.3).**

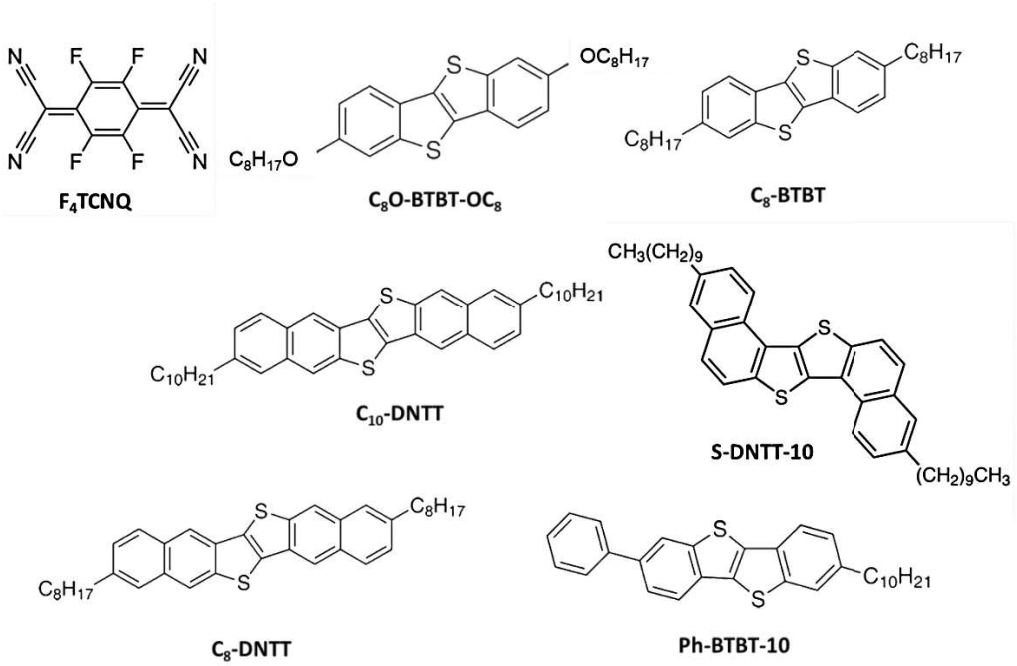


Figure 1.3. Chemical structures of soluble small molecule semiconductors used in this thesis.

The spatial arrangement of π-systems in the solid-state is of equal significance to molecular structure,[14] as it governs the extent of overlap of frontier orbitals, which is crucial for facilitating charge transport. Notably, for small molecule OSCs there exist four primary packing motifs of aromatic cores, as depicted in **Figure 1.4**. Among these motifs, herringbone and brick-wall packing configurations exhibit a propensity to yield the highest charge carrier mobility.

In these assemblies, charge transport predominantly occurs within the x,y plane, known as the transport plane, although some degree of transport along the z-direction may also manifest.

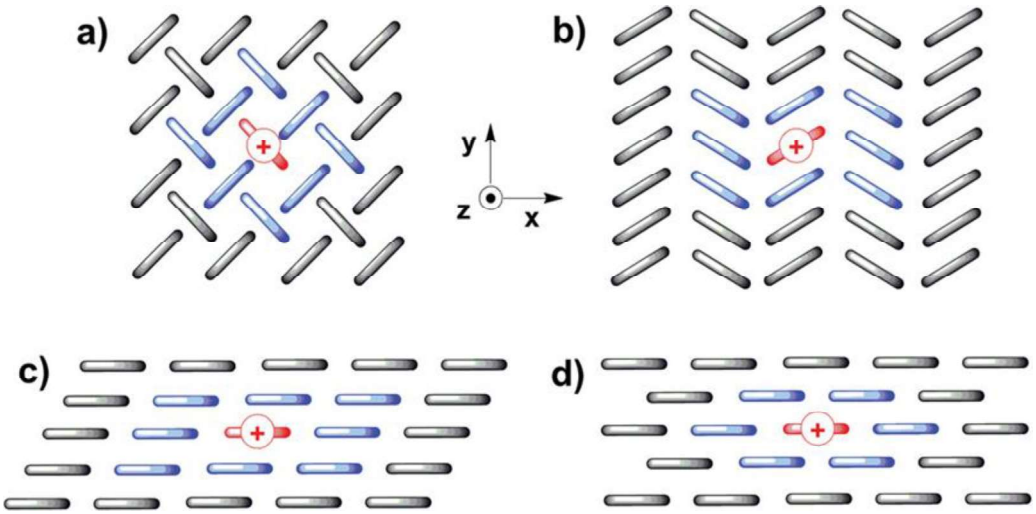


Figure 1.4. Schematic description of most encountered packing motifs of molecular semiconductors in crystals. Molecules bearing a hole are highlighted in red. First-neighbor molecules are colored blue. a) Herringbone arrangement with charge transport dominated by edge-to-face interactions (eight first neighbors). b) Slipped π-stacking (eight first neighbors). c) Slipped-stack packing (eight first neighbors). d) Brick-wall arrangement (six first neighbors). x–y plane is the transport plane. Extracted from [15].

Furthermore, it has been also observed that depending on the dimensionality of the crystal packing and the relative arrangement of the molecules in the solid state, i.e. the packing motif, the charge transport can be anisotropic in the different directions of the crystal.[16] This anisotropy can lead to differences of 2 and 3 orders of magnitude in the charge carrier mobility and, therefore, is a factor that should be considered when using OSCs as active layers in organic devices.

1.3 Charge transport mechanisms

Due to the nature of OSC materials, they reveal distinctive charge transport mechanisms compared to the one observed in inorganic semiconductors. In inorganic semiconductors, charge carriers move freely through delocalized energy states, a mechanism known as band transport. Conversely, charge transport mechanisms in organic solids have been a topic of debate for many years, as a result of their complexity. A clear description of the charge transport in solids exists in the two extreme limits of very low mobility and very high charge carrier mobility values, where transport can be described in terms of incoherent hopping of localized charges between sites and Boltzmann band transport of delocalized Bloch electrons, respectively.[14][15]

Two key parameters of charge transport at the microscopic length scale are: the electronic coupling or transfer integral (J, in meV) and the reorganization energy (λ, in meV). J corresponds to the wave function overlap of the orbitals of neighboring molecules and strongly depends on the chemical structure of the molecule and the packing motif adopted in the crystalline structure ($10 \leq J \leq 100$ meV).[19] λ represents the energy loss when a charge carrier passes through a molecule, and it depends on the conjugation length and degree, and the packing of the organic molecule ($50 \leq \lambda \leq 500$ meV).[18], [20] If $J \ll \lambda$ (weak coupling regime), the charge wavefunction is localized on a single molecule and transport takes place through a series of incoherent hopping events. On the contrary, if $J \gg \lambda$ (strong coupling regime), charge wave-function is delocalized over several molecules and transport proceeds through diffusion. The crucial point is when $J \approx \lambda$ in organic solids, highlighting the need to develop a theory for this crossover regime (**Figure 1.5**).

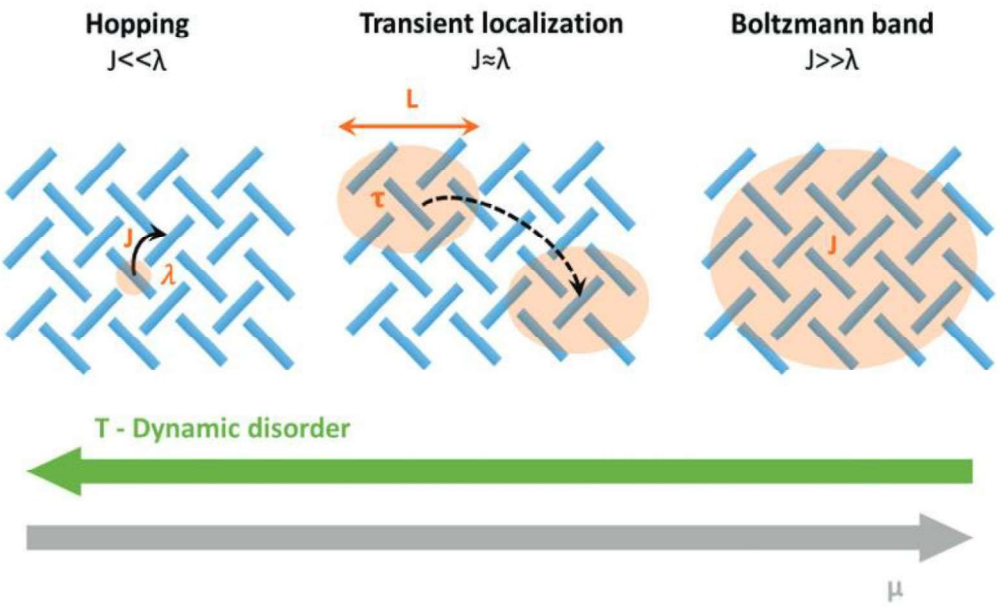


Figure 1.5. Schematic representation of the charge transport mechanisms taking place in the hopping, transient localization, and Boltzmann band model. The orange areas represent the charge delocalization. Extracted from[15].

The variety of transport mechanisms proposed for organic materials depends on their structural order, which can range from amorphous films to highly ordered single crystals. This diversity in structural order leads to a range of charge transport behaviors and poses both challenges (difficulties in correlating a specific mechanism) and opportunities for the development of organic electronic devices. These mechanisms are fundamental in various electronic and semiconductor devices. The most used transport models are described below:

Band-like Transport:

Band-like transport refers to the movement of charge carriers in a material through a band of states, rather than through localized states (**Figure 1.6**). Electrons in the conduction band and holes in the valence band can contribute to charge transport. This type of transport is often observed in highly crystalline semiconductors. The mobility of charge carriers within the band is determined by the material's band structure and the presence of impurities or defects that can cause carrier scattering.

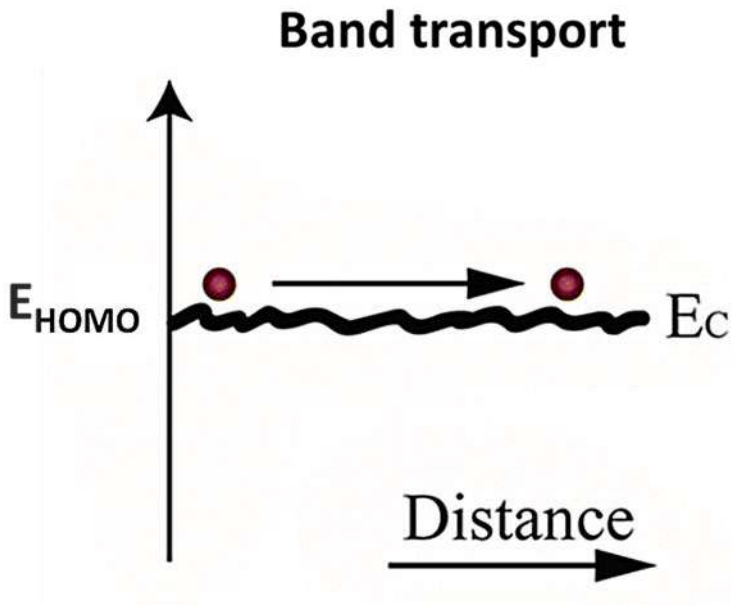


Figure 1.6. Schematic representation of the band transport mechanism. Extracted from [21].

The multiple trapping and release theory:

The multiple trapping and release theory (MTR) is a concept in the field of charge transport within polycrystalline semiconductor materials (**Figure 1.7**). This theory explains the behavior of charge carriers, such as electrons or holes, as they move through these materials and experience temporary trapping and subsequent release at various sites or energy levels. This model assumes that carriers arriving at a trap are instantaneously captured with a probability close to one and that a thermally activated process controls the release of the trapped carriers.

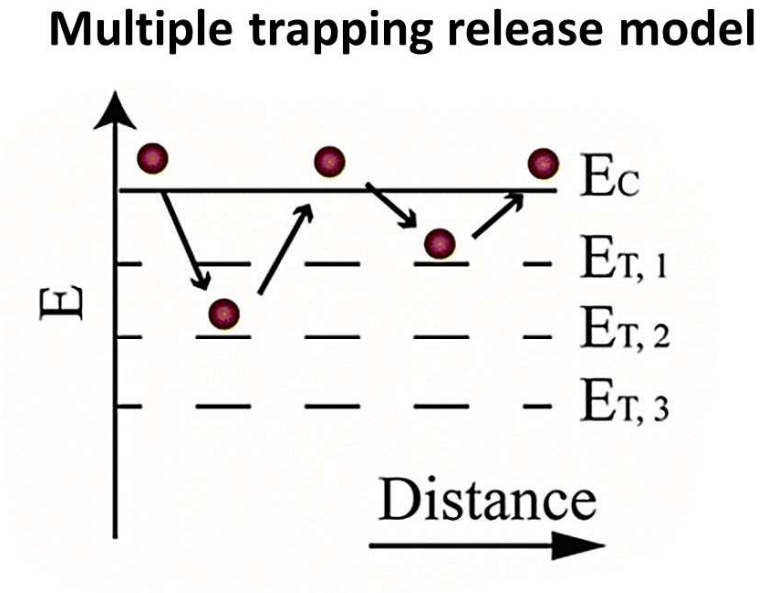


Figure 1.7. Schematic representation of the multiple trapping release model. Extracted from [21].

Hopping Transport:

Hopping transport is characteristic of disordered or amorphous materials. Charge carriers move by hopping from one site to another within the material. In contrast to band transport, hopping transport is thermally activated (**Figure 1.8**). It relies on the vibrations of the lattice to provide the necessary energy for charge carriers to overcome energetic barriers and move through the material. Phonons are quantized vibrational modes in a crystal lattice, and they facilitate the transfer of energy that enables charge carriers to hop from one site to another.

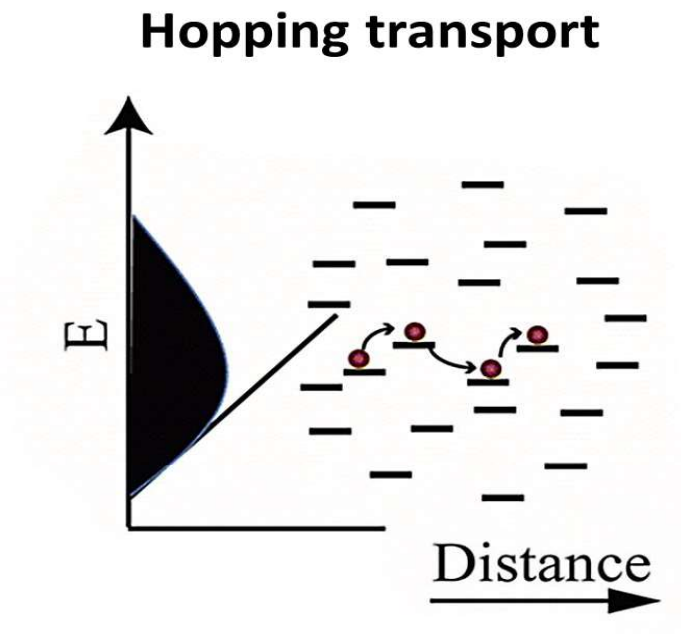


Figure 1.8. Schematic representation of the hopping transport mechanism. Extracted from [21].

1.4 Organic semiconductors processing techniques

Small molecule OSCs can be deposited through thermal evaporation or solution-based techniques. However, solution processing techniques are generally preferred for OSC thin film preparation due to their cost-effectiveness and suitability for large-area fabrication. Common solution-based deposition methods include drop-casting, spin-coating, spray coating, and meniscus-guided solution shearing. The latter techniques are gaining significant attention for their compatibility with roll-to-roll processes and will be discussed in detail below.[19]

Meniscus-guided coating techniques rely on the consistent and controlled movement of a solution meniscus in one direction across the substrate surface. This characteristic enables the precise manipulation of molecules assembly, leading to the desired morphology and crystallinity of the OSC thin films. In **Figure. 1.9**, some of the most employed meniscus-guided coatings that have been used for depositing thin films of small-molecule OSCs are illustrated.

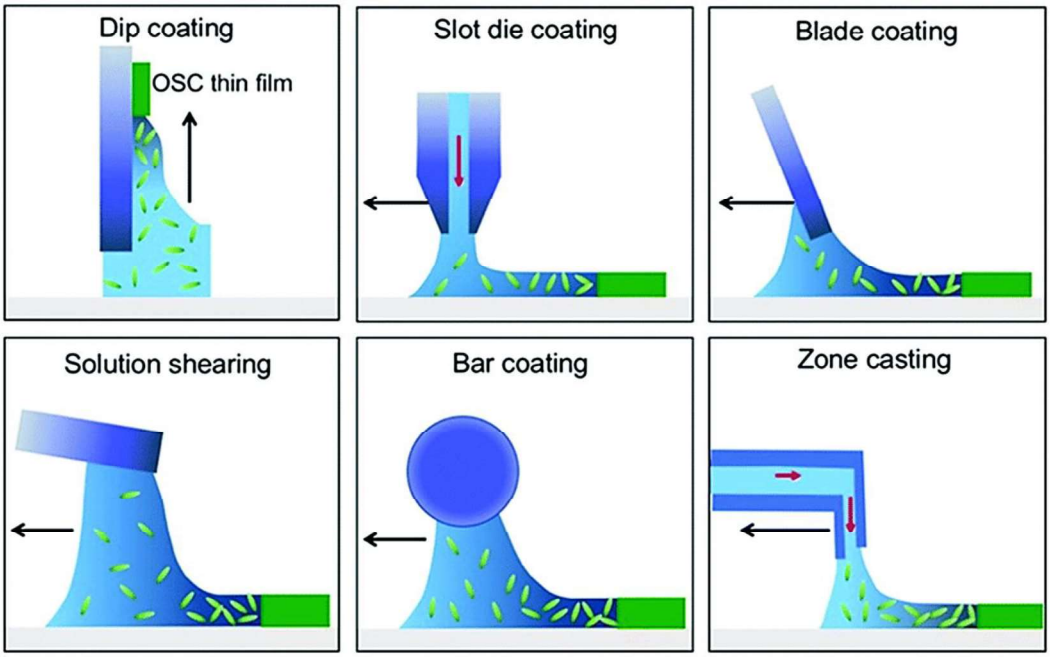


Figure. 1.9 Schematic summary of typical meniscus-guided coating techniques. Extracted from [22].

In this thesis, we have used the bar-assisted meniscus shearing (BAMS) technique. BAMS is a modified version of the traditional blade coating, distinguished by the formation of a liquid meniscus between the substrate and a rounded bar. It consists of injecting an OSC solution into the gap between a substrate on a hot plate and a metallic bar, creating a confined meniscus.[23] The bar (or substrate) is then horizontally moved at a constant speed, dragging the meniscus, and leaving behind a uniform, dry thin film. This process is illustrated in **Figure 1.10**. High-quality OSC thin films at speeds compatible with roll-to-roll processes have been reported employing this technique.[24]

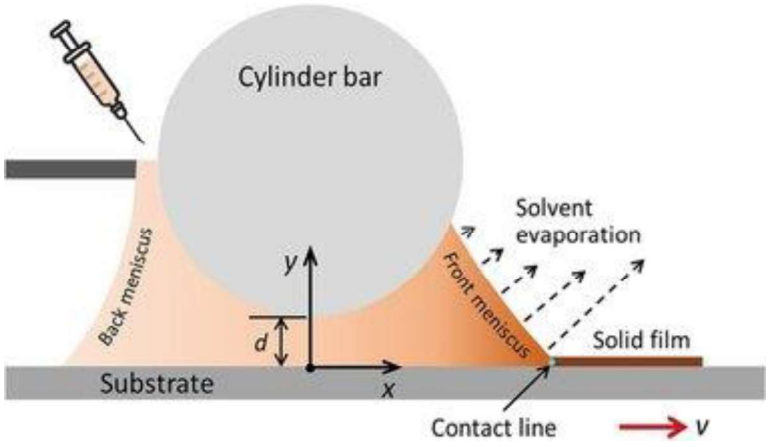


Figure 1.10 A schematic illustration of the meniscus during zone casting with the solute concentration field. The deposition head is formed between a cylinder bar and a substrate, which are separated by a gap distance d. The front meniscus shows predominant solvent evaporation as the substrate moves at a coating speed v. Extracted from [25].

Our research group initially pioneered the BAMS technique for processing the small semiconducting molecule dibenzo-tetrathiafulvalene (DB-TTF) blended with polystyrene (PS) from solution, resulting in highly crystalline films, as evidenced in the inset of **Figure 1.11 (a,b)**.[15] Thereafter, this method has been successfully applied to a diverse range of small molecule OSCs,[18] typically utilizing blends with PS. This blending approach facilitates the deposition of OSCs since it increases the solution viscosity yielding homogeneous and highly crystalline films. Moreover, the use of blends offers additional benefits due to the vertical phase separation of the OSC and PS that takes place during deposition (**Figure 1.11c**), in which the OSC crystalline film is formed on the top of a PS layer. This phase separation promotes the creation of more stable devices by passivating the polar hydroxyl groups at the SiO_2 dielectric interface by the PS layer, thereby reducing interfacial charge traps and enhancing environmental stability.

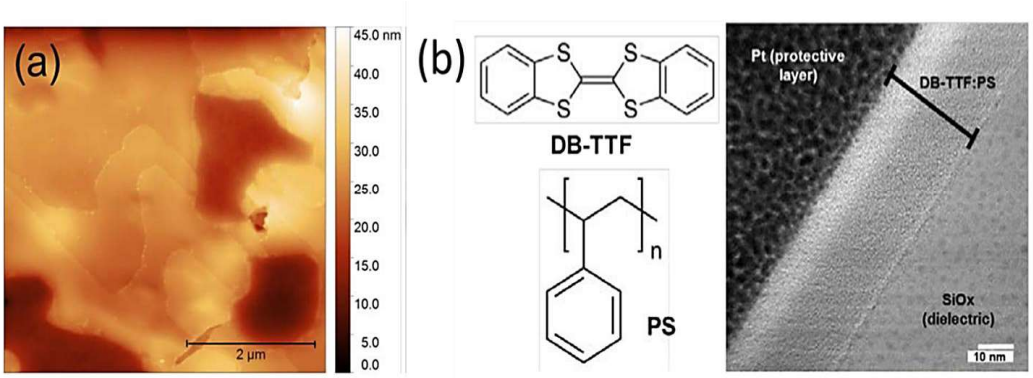


Figure 1.11. (a) AFM images (5×5 µm2) of the DB-TTF:PS blend on the channel. The root mean square roughness are 8.1 nm. (b) Left. Chemical formulas of DB-TTF and PS. Right. EF-TEM profile image of a dibenzo-tetrathiafulvalene: polystyrene (DB-TTF:PS) film showing the vertical phase separation [26].

1.4.1 Influence of the experimental parameters on the thin film properties during meniscus-guided coating

The morphology and structure of the OSC thin films play a pivotal role in determining the electrical properties of the films and hence, the performance of the devices in which they are implemented, such as OFETs. Optimal OFET performance is typically associated with OSC thin films characterized by large grain sizes, high surface coverage, and thin thickness. Likewise, the polymorph formed will be also key for achieving an optimized performance.[19][24] Therefore, during the OSC thin film preparation, it is imperative to control all the deposition parameters that are involved as well as to gain insights into their impact on the thin film properties. In this way, researchers can establish a solid foundation and practical guidelines for future endeavors in OSC thin-film morphology control, thereby advancing the field of organic electronics. Here, we will discuss some of the parameters that can be tuned during the thin film coating using meniscus-guided solution shearing techniques.

Coating Shearing speed:

The coating shearing speed has a strong influence on the crystallization and nucleation processes.[27] The most obvious effect is related to the thin-film texture. In several works, it has been demonstrated that at low speeds in the convective regime, oriented nearly single-crystalline films can be produced because crystallization takes place at the meniscus contact line as the solvent is evaporated. [28], [29], [30], [31] However, at higher speeds, the crystallization occurs thanks to nucleation and coalescence from a supersaturated solution.

In a deposition experiment where the solvent evaporates slowly, such as in drop-casting, the crystallization occurs near the substrate–liquid interface and the crystal growth is fed by molecules from the bulk of the solution as shown in **Figure 1.12 a**. On the contrary, under fast drying conditions, typically, the crystallization initiates at the air-liquid interface and proceeds toward the substrate, (**Figure 1.12 b)**) spatially confining the crystallization.[26]

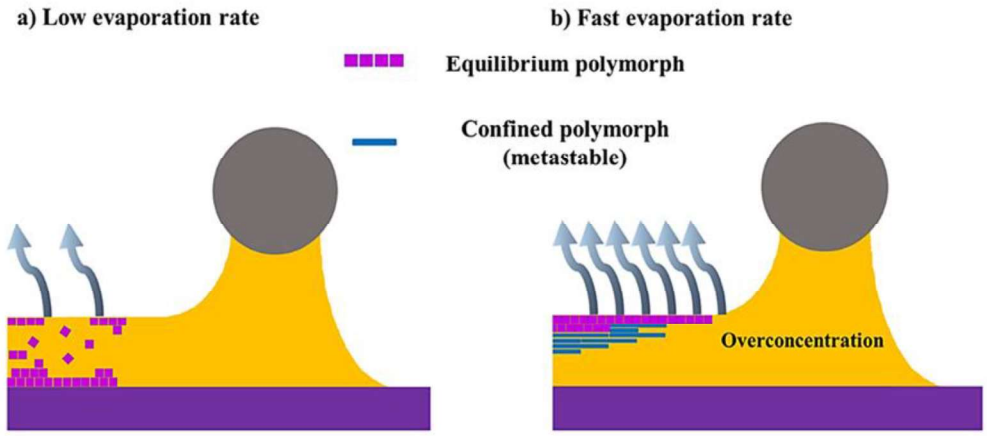


Figure 1.12. Scheme of the crystallization process that takes place in a) a low evaporation rate and b) a fast evaporation rate deposition experiment. Extracted from [32].

Generally, during solution shearing in the convective regime, the liquid film thickness decreases as the solution-shearing speed increases. However, when reaching the fast evaporation regime this tendency is reversed and the thin film thickness increases with the coating speed.[33] This was observed in our group when studying thin films of DB-TTF blended with PS and deposited by BAMS.[34] Further, it was found that at low speed (1 mm. s^{-1}), the layer of the OSC revealed a well oriented ribbon-shaped crystals, while at higher speed

(10 mm. s^{-1}) the layers were isotropic and were formed by uniform plate-like crystallites (**Figure 1.13**). Interestingly, at low coating speed, the films grown corresponded to the thermodynamic α-polymorph, while the kinetic γ-phase was formed at higher coating speeds. Thus, this work elucidates that the coating speed has a strong impact on the thin film crystallization and thin film morphology.

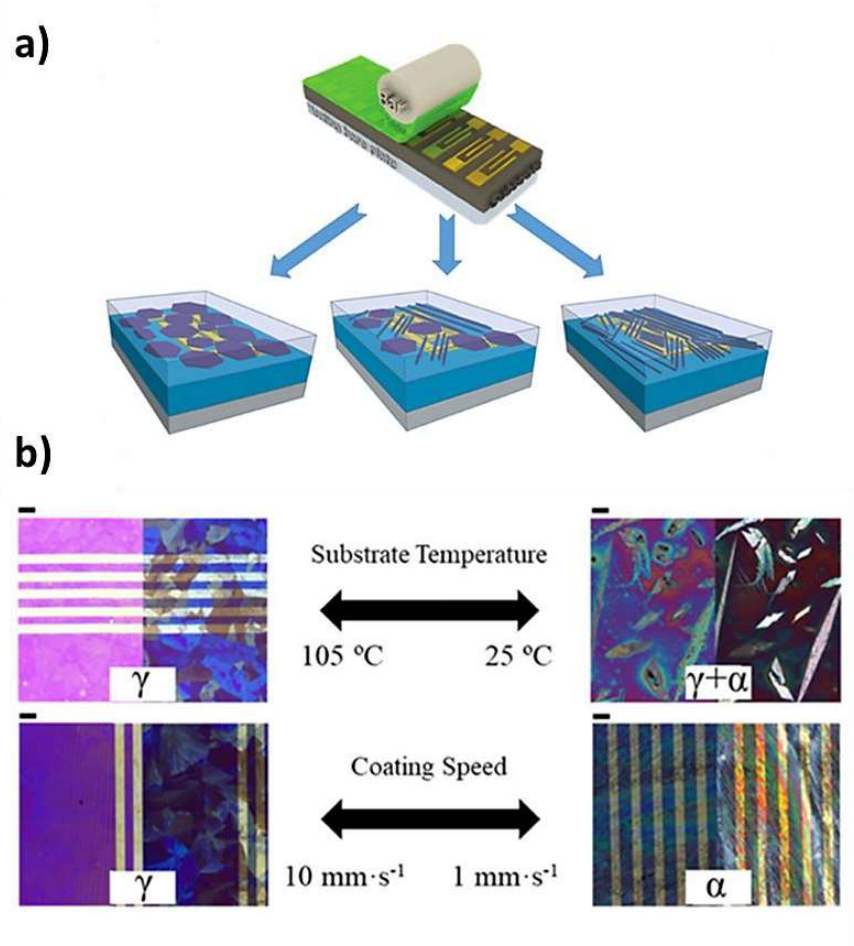


Figure 1.13. a) Conceptual illustration of how crystal growth and polymorph formation can be programmed during solution-shearing of DB-TTF:PS. b) Representative optical microscopy images of some of the films prepared of DB-TTF:PS by varying the substrate temperature or the coating speed (left and right parts of the images correspond to with and without polarizer). Scale bar: 100 μm for all images.Figures were extracted from [34].

Substrate Temperature:

The substrate temperature is a critical parameter in controlling the deposition of OSCs when using techniques such as thermal evaporation or drop-casting.[32] In solution-shearing deposition processes, the chosen temperature is typically based on the solvent's boiling point to regulate the crystallization rate. However, systematic studies exploring the influence of the stage temperature on thin-film crystallization remain limited. Optical microscopy images of the films of DB-TTF:PS deposited at different temperatures are shown in **Figure 1.13b**. The film morphology and crystallinity are highly dependent on the substrate temperature. At low substrate temperatures, needle-shaped crystals are observed, whereas films deposited at higher temperatures exhibit plate-like crystalline domains. X-ray characterization demonstrated that, when keeping constant the coating speed at 10 mm. s^{-1}, at low temperature a mix of α and γ polymorphs were obtained, while solely the polymorph γ was formed at high temperature (**Figure 1.13b**). [29]

Ink formulation: Blending with polymer binders:

The ink formulation also has a strong influence on the thin film properties. For instance, concentration directly affects the thin film thickness. In addition, the selection of the solvent is also relevant since it has an impact on the nucleation and crystallization process. The solvent determines the OSC solubility, molecule solvation, and molecule–solvent interactions. In general, high boiling point solvents are chosen to control better the evaporation rate. Lower evaporation rates permit more efficient migration and reorganization of the molecules during crystallization and tend to give rise to thermodynamic polymorphs.

As previously mentioned, a very powerful strategy employed in the last few years

to fabricate crystalline OSC thin films of small molecules is the use of polymeric blends, [35] usually mixing the OSC with an insulating polymer that acts as matrix. [35], [36], [37] This facilitates the processability of the OSC because the polymer acts as a binder and helps to overcome issues related to dewetting, which hampers film uniformity. The choice of polymer binder can profoundly influence various aspects of the thin film characteristics and, in turn, the device's performance.[38] The binding polymer has a key role in the materials phase, separation, OSC crystallization, density of charge carrier traps, and environmental stability.[32],[33] For example, different polymer binders were employed to investigate their effect on the performance of OFETs based on the semiconductor 2,8-difluoro-5,11-bis(triethylsilylethynyl)anthradithiophene (diF-TES-ADT).[39] It was found that blends with poly (methyl methacrylate) (PMMA) yielded rougher films with smaller crystalline domains compared with the blends with PS. Electrically, the blends with PS exhibited an enhanced mobility and lower hysteresis, which was attributed to the less polar nature of PS that results in reduced charge trapping. Considering the molecular weight, small differences were found with the PMMA films. However, a notable improvement in mobility was observed in the PS films of lower molecular weight, giving devices with mobility values exceeding 1 $cm^2 . V^{-1} . s^{-1}$.

1.4.2 Post-deposition annealing procedures

Annealing processes are widely used to improve molecular organization after film formation. These processes can help in making films more crystalline and in reducing the charge traps. Additionally, annealing steps can be employed for carrying out crystal phase transformations, typically to convert a kinetic crystal phase to a thermodynamic one. The annealing processes can be performed by the application of temperature or solvent vapors.[35]

Thermal Annealing

Thermal post-annealing operates as a controlled heat treatment method, leveraging elevated temperatures to facilitate molecular rearrangement within the material. This controlled heating triggers a series of mechanisms, including the diffusion of point defects, the migration of grain boundaries, and the recrystallization of the material. By promoting these processes, annealing can mitigate defects and enhance crystalline order. [40]

Iino et al. reported, as shown in **Figure 1.14a**, spin coated thin films of the asymmetric OSC 2-decyl-7-phenyl-[1]benzothieno[3,2-b][1]benzothiophene (Ph-BTBT-10) that crystallises in a metastable phase where the molecules adopt a lamellar single layer structure with an interlayer spacing corresponding to the molecular length.[40] However, after a thermal annealing process, there is a conversion to the bulk phase, in which the molecules crystallize following a lamellar bilayer with a head-to-head arrangement and a stacking periodicity twice the molecular length (i.e., 5.3 nm). Such phase transformation significantly impacted the OFET mobility, enhancing it by about one order of magnitude and reaching values above 10 $cm^{2}.V^{-1}.s^{-1}$ after the thermal annealing process at 120 ^{o}C (**Figure 1.14b**).[41] Thermal annealing has also been applied to improve the molecular conformation in polymer OSCs. J. Kim et al. showed that hole and electron mobilities could be improved in thienylenevinylene-based donor-acceptor polymer OSCs after annealing, since the thermal treatment induced a more ordered intra-chain conformation (i.e., increasing the backbone planarity) and inter-chain packing (**Figure 1.14 c,d**).[41]

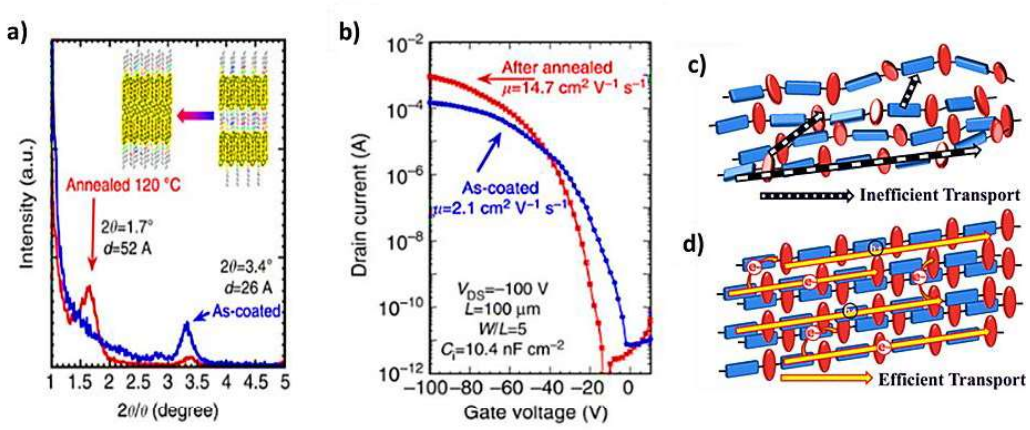


Figure 1.14. a) Out-of-plane small-angle X-ray diffraction patterns for crystalline films based on Ph-BTBT-C10 as-coated and after annealing, with a schematic illustration of the crystalline structure. b) Transfer characteristics of OFETs fabricated with polycrystalline thin films both as coated and after thermal annealing. Schematic illustration of the change in polymer chain conformation by the annealing process: (c) non-annealed polymer film and (d) annealed polymer film. Extracted and adapted from [33], [35].

Solvent Vapor Annealing

Solvent vapor annealing (SVA) involves exposing an OSC thin film to solvent vapors that can interact with the material. This process induces swelling and reorganization at the molecular level, allowing for controlled crystallization and improved molecular ordering. The choice of solvent, annealing time, and temperature are critical parameters that influence the extent of morphological changes.

H. Khan et al. have demonstrated the effect of SVA in spin-cast films of 6,13-bis(triisopropylsilylethynyl) pentacene (TIPS-Pn) (**Figure 1.15**).[42] It was observed that SVA in the molecular regime can cause significant OFET performance improvements by promoting lamellar crystallization, but allowing the solvent to percolate and form a liquid phase state results in catastrophic

reorganization and dewetting of the film, making the process counterproductive. By optimizing the experimental conditions (i.e., annealing time and vapor pressure) the charge carrier mobility was improved by nearly two orders of magnitude.

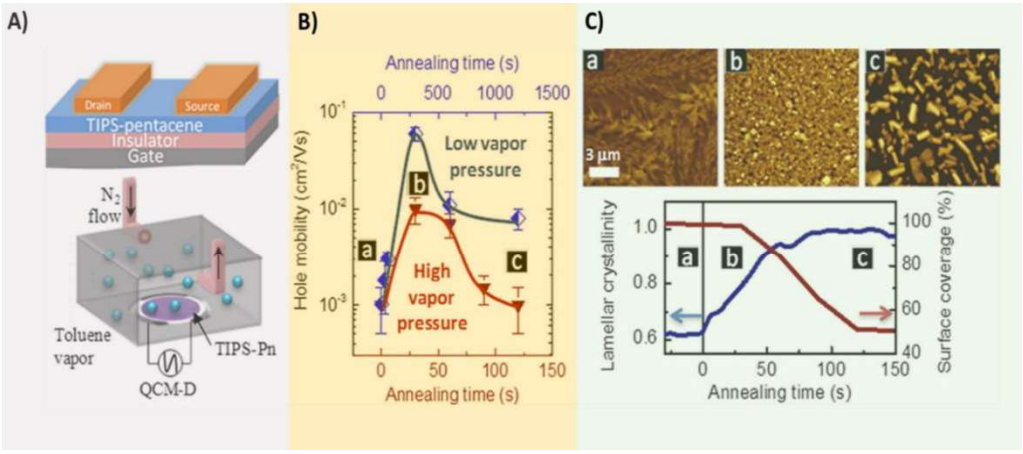


Figure 1.15. A) Bottom-gate/top-contact OFETs of 6,13-bis(triisopropylsilylethynyl) pentacene (TIPS-Pn) and in situ using quartz crystal microbalance with dissipation (QCM-D) measurements during solvent vapor annealing on quartz sensors coated with a spin-casted TIPS-Pn thin film. B) Electrical performance of the TIPS-Pn OFETs exposed to solvent vapor in the saturation (red) and low vapor pressure regimes (black) C) AFM images (20 × 20 μm^2) taken at different annealing times and fractional surface with respect to annealing time. Extracted from reference [42].

1.5 Organic field-effect transistors (OFETs)

1.5.1. Operation principle

There are various methods available for measuring charge transport in OSCs, but the most employed one is undoubtedly using the field-effect transistor configuration. Transistors, which are three-electrode devices, operate based on field-effect doping. This process involves modulating the number of mobile charges within the semiconductor layer by applying a voltage to an electrode that is separated from the semiconductor by a dielectric layer. As depicted in **Figure 1.16**, an electrical drain current (I_D) flows between two contacts (i.e., source and drain) and is controlled at the third terminal (i.e., gate) by a voltage signal that creates an electric field through a dielectric. Charge transport takes place within the semiconductor at the interface with the dielectric layer.

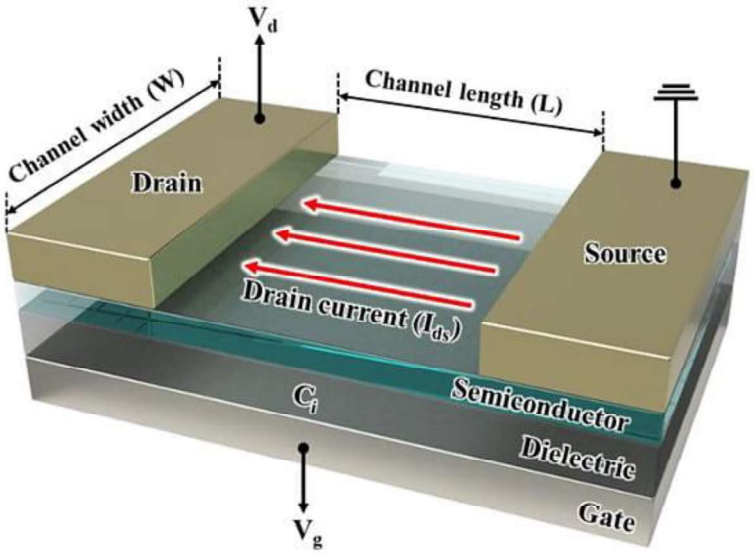


Figure 1.16. Schematic of bottom-gate/top-contact OFET. Extracted from [43]

The operating principle of an OFET can be outlined in three stages by examining the relationship between the drain voltage (V_D) and $|V_G-V_{th}|$, where V_G represents the gate voltage and Vth is the threshold voltage (**Figure 1.17**). When V_G exceeds V_{th}, charge carriers begin to accumulate at the OSC/dielectric interface, forming a conducting channel. Subsequently, if V_D is less than $|V_G-V_{th}|$, the OFET operates in the linear regime, where the distribution of charge carriers' density becomes nearly symmetric, as depicted in **Figure 1.17(a)**. In this regime, the drain current increases linearly with the drain voltage and can be described by the following equation:

$$I_D = \frac{w}{L}\mu \cdot C \cdot (V_G - V_{th}) \cdot V_D \qquad \textbf{(1-1)}$$

Here, I_D represents the drain current, W and L denote the width and length of the channel, respectively, μ is the field-effect mobility, C is the gate capacitance per unit area, V_G is the gate voltage, V_D is the drain voltage, and V_{th} is the threshold voltage.

As V_D increases, the density of charge carriers near the drain electrode diminishes. At a certain point when $V_D=|V_G-V_{th}|$, the channel becomes "pinched off" (**Figure 1.17b**). The pinch-off point indicates the maximum I_D; beyond this point, even if the drain voltage continues to increase ($V_D> |V_G-V_{th}|$), I_D remains constant. At this stage, the transistor operates in the saturation regime, and its behavior can be described by the following equation (**Figure 1.17c**):

$$l_D = \frac{w}{2L}\mu \cdot C \cdot (V_G - V_{th})^2 \qquad \textbf{(1-2)}$$

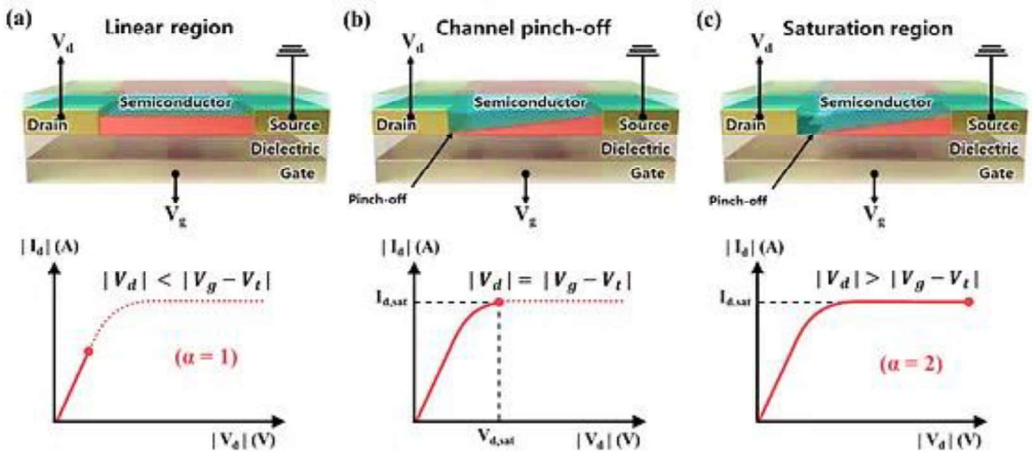


Figure 1.17. Schematic representation of the working principle of OFETs according to the charge carrier density modification in the channel with the applied drain voltage (V_D) and gate voltages (V_G) .(a) Channel formation when $V_D < |V_G - V_{th}|$, (b) channel pinch off at the drain electrode occurring when $V_D = |V_G - V_{th}|$ and (c) saturation regime occurring when $V_D > |V_G - V_{th}|$ and opposite charge carriers cover drain electrode. Extracted from [43].

Figure 1.18 shows a simplified electronic energy level diagram to illustrate the operating principle of OFETs from the perspective of the energy level. In the absence of a gate voltage, the OSC layer remains free of mobile charges, resulting in no charge transport, since the highest occupied molecular orbital (HOMO) and the lowest unoccupied molecular orbital (LUMO) of the OSC do not correspond to the Fermi levels (EF) of the source/drain electrodes. In a p-type OSC, the application of a negative gate voltage causes an upward shift in the energy levels of the HOMO/LUMO of the OSC, bringing the HOMO level closer to the EF of the source/drain electrodes. As a result, charges flow between the source and drain contacts when a negative drain voltage is applied. Conversely, in an n-type OSC, electrons serve as the main charge carriers, and charge injection and conduction are associated with the LUMO level. To facilitate charge accumulation and current flow, positive voltages (V_G and V_D) must be applied. From this schematic, the alignment of the EF of the metal electrodes to the

HOMO and LUMO energies of the p- and n-type OSCs, respectively, is critical for efficient charge injection into the material, enabling the fabrication of high-performance devices.

The fundamental operating principle of OFETs makes them an excellent platform for conducting structure-property correlation studies of materials. However, the fabrication processes of OFETs involve numerous parameters that can impact device performance. As a result, it is challenging to directly compare the electrical characteristics of devices based on the same OSC but using different preparation methods.

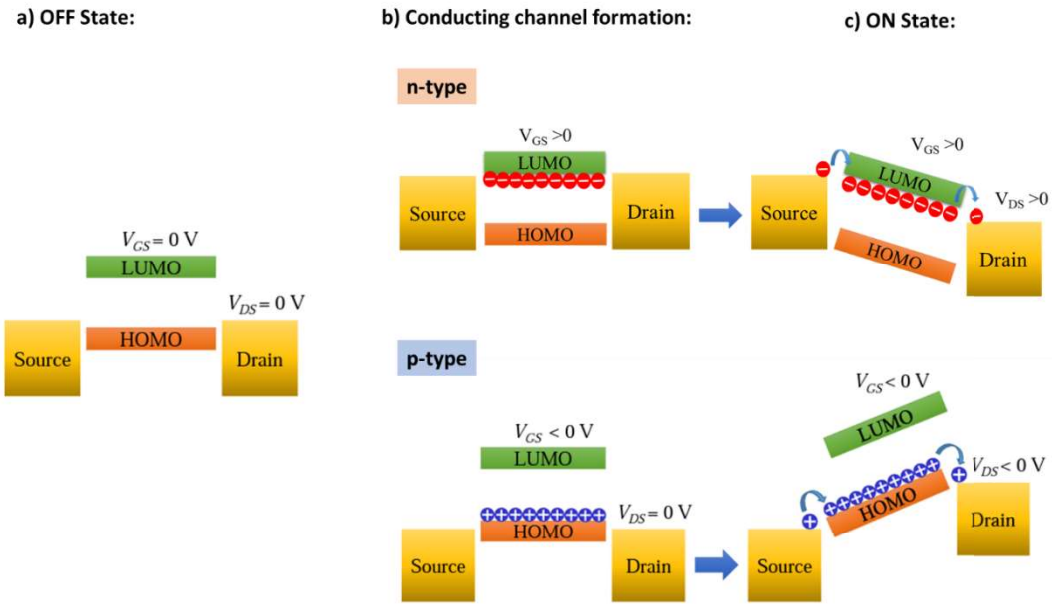


Figure 1.18. Schematic representation of the energy levels in an OFET. a) Ideal device in the off state, when no V_D and V_G are applied. b) Shift of the HOMO/LUMO energy levels by applying negative (positive) V_G and accumulation of holes (electrons) near the OSC/dielectric interface. c) Hole (electron) transport when a negative (positive) V_D is applied.

1.5.2 Device geometries

OFETs can be arranged mainly into four different geometries (**Figure 1.19**). The selection of device geometry is influenced by several factors. The TGBC (top gate/bottom contact) and BGTC (bottom gate/top contact) are commonly preferred as they maximize the area of charge injection, particularly at the interface between the source electrode and the semiconductor, where charge injection occurs. Additionally, the dielectric/semiconductor interface plays a crucial role in charge transport and should ideally have minimal defects. Consequently, when small molecule semiconductors are deposited via evaporation the BGTC or BGBC (bottom gate/bottom contact) geometries are preferred, primarily due to the rough top surface achieved through vacuum deposition of the organic layer. Among all the mentioned geometries, the used ones in this thesis are the BGBC and BGTC.

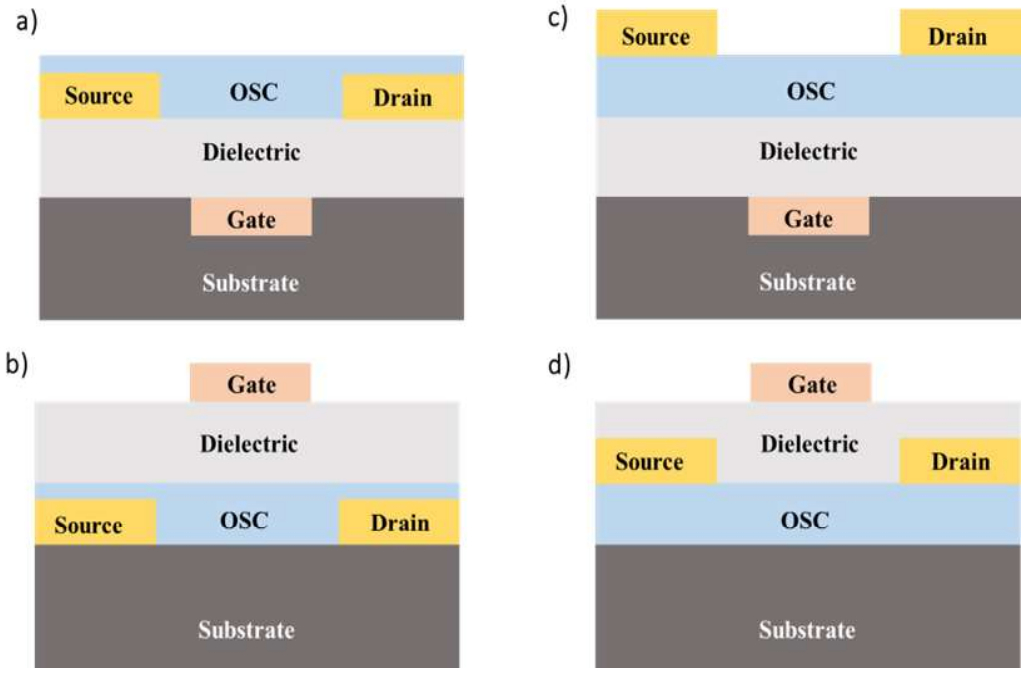


Figure 1.19. OFET architectures: a) Bottom-gate/bottom-contact (BGBC), b) bottom-gate/top-contact (BGTC), c) top-gate/bottom-contact (TGBC) and d) top-gate/top-contact (TGTC).

1.5.3 Electrical characterization and OFET parameters

In an OFET two essential device electrical characteristics are typically analyzed: Transfer and Output characteristics. On one hand, the output characteristics are obtained when the I_D is measured by sweeping the source-drain voltage (V_D) at constant gate voltages (V_G), as depicted in **Figure 1.20 (a)**. Additionally, the transfer characteristics are obtained by measuring I_D as a function of V_G at constant V_D, as shown in **Figure 1.20 (b)**. Furthermore, the mobility profile can be extracted from the transfer characteristics as a function of V_G, which offers insights into the quality or ideality of an OFET device.

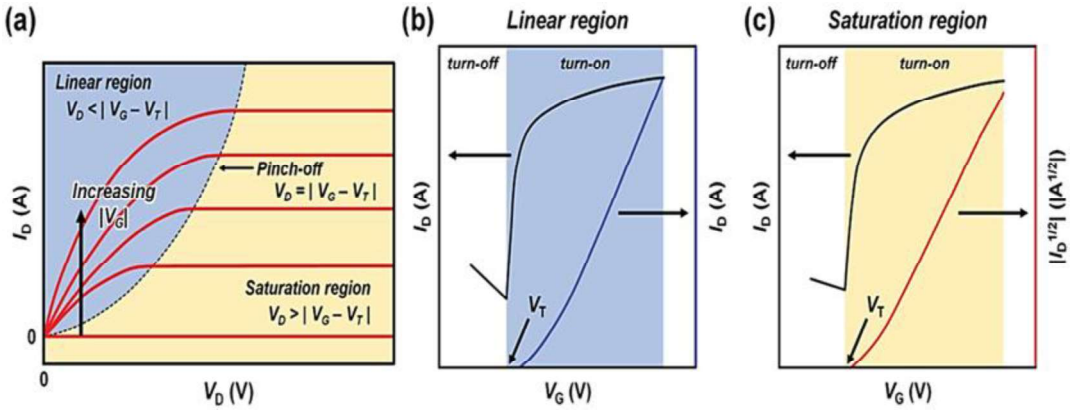


Figure 1.20. (a) OFET output characteristic depending on different gate voltages (V_G). Operating area and conversion values used for extracting OFET parameters in (b) linear and (c) saturation region. Extracted from reference [45].

There are several fundamental parameters in an OFET device that are critical to evaluating its quality and performance, such as field-effect mobility, threshold voltage, on/off current ratio, and sub-threshold swing, to name a few. These parameters can be extracted from the output and transfer curves and are described individually below.

Field-effect mobility

The field-effect mobility (μ) in an OSC represents the ability of charge carriers to move with semiconductors under varying electric fields. It is defined as the ratio of its drift velocity to the applied electric field, which reflects the moving ability of electrons in semiconductors under different electric fields. It is one of the most important parameters in OFET devices and it can be estimated from the transfer curves.

In an ideal scenario, the field-effect mobility extracted from the OFET properties aligns with intrinsic material mobility. However, practical devices typically show lower mobility values due to the presence of defects, contact resistance, and traps, which are influenced by the fabrication process and device configuration. Consequently, this value is a device parameter, not an intrinsic material property. Despite challenges in device-to-device comparisons, field-effect mobility is the most important figure of merit for evaluating the OFET performance. It can be calculated in the linear regime and the saturation regime according to the corresponding transfer characteristics.

In the linear regime, the conductivity (σ) increases with rising gate voltage, which corresponds to an increase in the number of charge carriers, as described by the following formula:

$$\sigma = e \cdot n \cdot \mu \qquad \textbf{(1-3)}$$

Here, n represents the number of charge carriers, e is elementary charge, and μ is mobility of charge carriers. To estimate the mobility, one can use equation 1-4 in the linear regime by plotting I_D against $V_{G,}$ as follows:

$$\mu^{lin} = \frac{L}{W \cdot C \cdot V_D} \frac{\partial I_D}{\partial V_G} \quad \textbf{(1-4)}$$

By performing a linear fit on the slope of the curve, the average device mobility can be determined. Additionally, mobility values at various gate voltages can be estimated to create a mobility profile, as previously described.

In the saturation regime, device mobility in saturation regime can be obtained by plotting the square root of the absolute value of I_D against V_G and then calculating the slope of the curve through a linear fit using the equation 1-5. This approach also allows for the extraction of the mobility profile (mobility vs. gate voltage) can be extracted.

$$\mu^{sat} = \left(\frac{\partial \sqrt{|I_{DS}|}}{\partial V_{GS}} \right)^2 \frac{2L}{W} \cdot \frac{1}{C} \quad \textbf{(1-5)}$$

Generally, mobility calculated in the saturation regime is higher than that extracted in the linear regime mainly due to the significant impact of contact resistance in the latter. Mobility profiles often exhibit gate voltage dependence, which can be attributed to factors such as contact resistance, traps, and defects. Field-effect mobility is influenced by several factors, including the purity of the OSC material, its crystal structure, the size of the crystal domains, the metal-OSC contact, and the overall device configuration.[34], [35] While the mobility of amorphous silicon is about 1 $cm^2/V \cdot s$, high-performance OFETs can achieve field-effect mobility values comparable or exceed this standard (**Figure 1.21**).

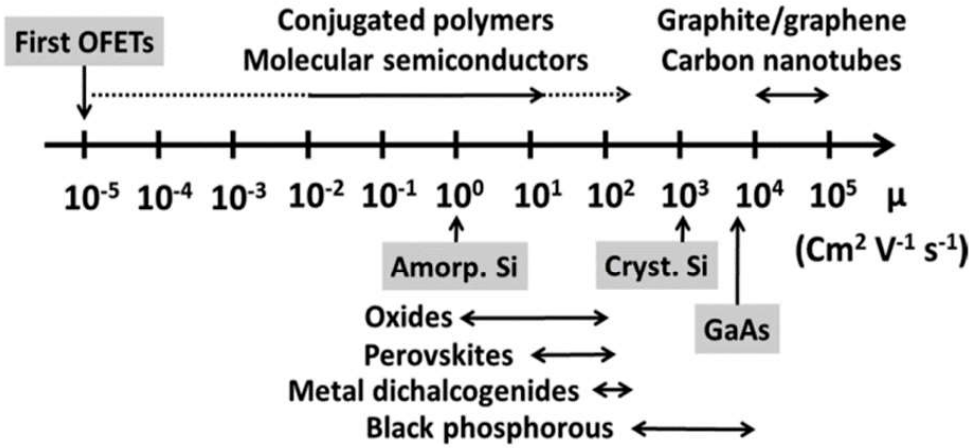


Figure 1.21. Scale of charge carrier mobility at room temperature for various semiconducting materials. Extracted from [12].

Threshold voltage and switch-on voltage

The threshold voltage represents the minimum voltage required to initiate transistor conduction. In an ideal case, the threshold voltage should be 0 V, or as low as possible to enable low power operations. A commonly used method to determine V_{th} consists in plotting I_D against V_G in the linear regime or plotting the square root of the absolute value of I_D against V_G in the saturation regime (**Figure 1.22**). The threshold voltage is determined then by the intercept point with the V_G axis. This parameter is influenced by several factors, such as contact resistance, misalignment of energy levels between the OSC and the source/drain metal, density of interfacial traps, and the built-in potential across the depletion region.[34][35]

Another closely related parameter is the switch-on voltage (V_{on}), which helps determine when a transistor turns on. V_{on} is the voltage at which the accumulation channel starts forming, but the OFETs are not on. This can be identified by plotting the absolute value of the source-drain current *vs* the gate voltage on a semi-logarithmic scale (see **Figure 1.22**). In this plot, the switch-on voltage is the point where the current begins to increase with the gate voltage. Ideally, there should be no difference between the threshold voltage and the switch-on voltage, with both values being zero in a perfectly functioning OFET.

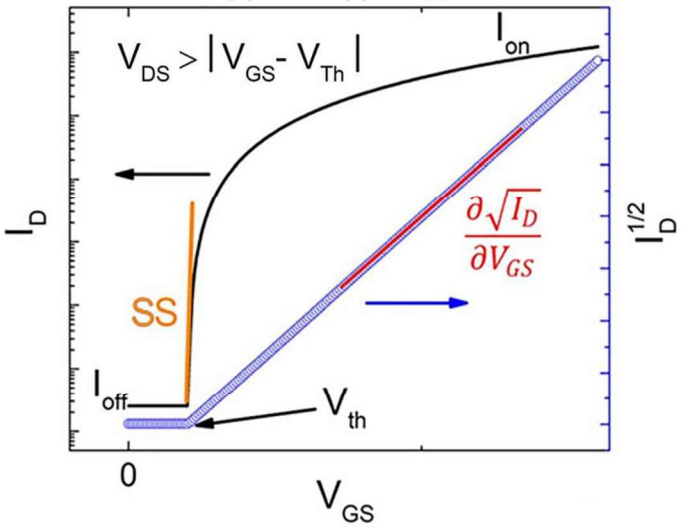


Figure 1.22. OFET parameters extraction from a typical transfer curve measured in the saturation. Extracted from [46].

On/Off current ratio

The on/off current ratio is the ratio of the on current to the off current (**Figure 1.22**) and serves as an indicator of the device's switching performance at a given gate voltage. A high on/off current ratio in OFETs signifies better device stability, improved resistance to interference, and enhanced load-driving capabilities. Conversely, OFETs with a low on/off current ratio indicates lower switching characteristics. Achieving a high on/off current ratio, ideally greater than 10^6, is crucial in logic circuits. Ioff represents a form of leakage current in the device and negatively affects energy consumption. The on/off current ratio is significantly influenced by factors including the device geometry, the mobility of the OSC, and the capacitance of the dielectric.[29-31]

Sub-threshold swing

The sub-threshold swing (SS) is a measure of how sharply an OFET turns on and is defined as the voltage needed to increase the source-drain current by one order of magnitude. This value is obtained from the slope of the transfer curve in a semi-logarithmic scale at low V_G, close to V_{on} (**Figure 1.22**).

$$SS = \frac{\partial V_G}{\partial (log\ I_D)} \qquad \textbf{(1-6)}$$

Therefore, the sub-threshold swing is typically expressed in V/dec.

A lower SS value indicates that the device can be turned on at a lower gate voltage, resulting in reduced power consumption of the final device.

The sub-threshold swing is affected by the quality of the OSC/dielectric interface and can also be used to estimate the interfacial charge carrier traps density (N_t) using the following equation:

$$N_t = \frac{C}{e^2}\left[\frac{e \cdot SS}{k_B \cdot T\, ln\, 10} - 1\right] \quad \textbf{(1-7)}$$

Here e is the electron charge, k_B is the Boltzmann constant, and T is the temperature

Contact resistance

In OFETs, contact resistance (R_c) refers to the electrical resistance at the interface between the electrodes and the OSC, which can limit the development of high-performance organic devices. High contact resistance can lead to inaccurate extraction of the device parameters. As previously noted, contact resistance is affected by the device's geometry. For instance, top contact/bottom gate (TCBG) and bottom gate/top contact (BGTC) configurations exhibit larger contact area. In TCBG devices, contact resistance is influenced not only by the charge injection and extraction processes at electrodes/OSC interface (Rint),[46] but also on the transport of charges through the OSC bulk region to the accumulation channel (Rbulk) (**Figure 1.23**). Additionally, traps at the OSC/electrodes interface can further impact the overall Rc. [47]

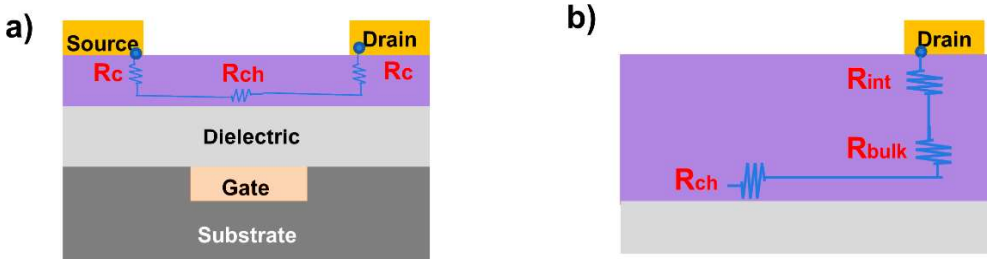


Figure 1.23. a) Scheme of contact and channel resistances in bottom-gate top-contact OFETs. b) detailed view highlighting the contribution of the interface and bulk resistance (R_C = Rint + Rbulk) in top-contact OFETs.

Various techniques exist to determine contact resistance by electrically measuring one or several OFETs. Among the most used methods are the Y-function method,[48] the transfer-length method (TLM), [49] and the four-point probe method.[50] Additionally, Kelvin probe force microscopy (KPFM)[51] can be utilized to assess contact resistance in top-contact devices.

The TLM method involves fabricating test structures with varying channel lengths. By measuring the device's resistance at different channel lengths, the contact resistance can be extracted from the following equation:

$$R = R_c + \frac{L}{W \cdot C \cdot \mu(V_G - V_{th})} \quad \textbf{(1-8)}$$

By plotting the total resistance of the devices at a specific drain voltage *vs* their channel length, the contact resistance (R_C) be estimated from the slope of the linear fit. Using this method, one can determine how the contact resistance varies with the gate voltage. However, to apply this methodology successfully, sufficiently homogeneous devices are required, which cannot always be guaranteed.

Charge trapping

An electronic trap refers to any imperfection within a semiconductor that generates localized electronic states. These states, which are spatially and energetically distributed, exist within the band gap of the OSC around the point of imperfection. Traps can be divided into two categories based on their relative energetic positions at a given temperature:

a) Shallow Traps

Shallow traps are located around a few k_BT (where k_B is the Boltzmann constant, and T is the temperature) from the band edges. These traps can temporarily capture and restrain charge carriers, which can then be released back into the energy band by thermal energy.

b) Deep Traps

Deep traps are located around several k_BT from the band edges. These traps can also capture and restrain charge carriers, but the energy required to release them back into the energy band is much higher.

The charge carrier traps have a different influence on charge carrier transport depending on the prevailing transport mechanism:

1. **Multiple Trapping and release (MTR) Model**: In this model, charges traveling through delocalized states are trapped by localized shallow trap states within the band gap and subsequently released back into the energy band by thermal energy (as illustrated by the blue arrows in **Figure 1.24**).

2. **Band-like Model**: In this model, traps can scatter the charge carriers, leading to a reduction in mobility.

3. **Hopping transport model**: At high trap densities, trapped charge carriers can contribute to transport by thermally activated hopping or tunneling between localized states (shown by the orange arrows in **Figure 1.24**).

In summary, semiconductor traps can have a significant impact on charge carrier transport in organic semiconductors, depending on their energetic position and the dominant transport mechanism. Traps typically give rise to hysteresis in the electrical characteristic curves, high threshold voltages, low bias stress stability, slow device switchability, and high contact resistance. Understanding and controlling the trap properties is crucial for improving the performance of organic electronic devices.

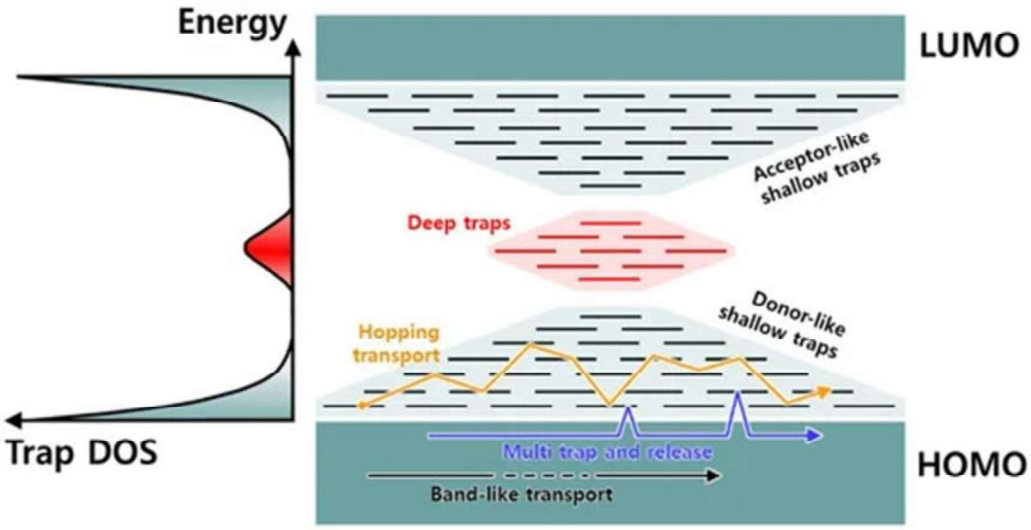


Figure 1.24. Schematic diagram of trap de density of states (DoS) function and corresponding trap states (shallow trap and deep trap) there are three types of transport mechanisms: (i) band-like transport, represented by a black arrow; (ii) multiple-trap and release (MTR), represented by a blue arrow; and (iii) activated hopping transport between localized states thermally, represented by an orange arrow. Reprinted from [44].

1.6 Objectives

In this thesis, we employed the bar-assisted meniscus shearing (BAMS) technique to process blends of p-type and n-type small molecule OSCs with polymer binders, aiming to create high-performance OFETs. Our primary focus was to comprehensively investigate the impact of various parameters involved in the OSC deposition process on the performance of these OFETs. Additionally, the application of annealing steps to promote phase transformations of evaporated and solution processed OSC films was explored to enhance the OFET performance.

The specific objectives of this thesis can be outlined as follows:

i. Process from solution charge transfer complexes formed by the benzothienobenzothiophene derivative C_8O-BTBT-OC_8 and F_xTCNQ to explore their potential implementation as the active layer in OFETs.

ii. Optimize the solution processing by BAMS at high throughput of OSC films based on [1]benzothieno[3,2- b][1]benzothiophene (BTBT) and dinaphtho-[2,3-b:2 ′ ,3 ′ -f]thieno[3,2- b]thiophene (DNTT) derivatives, and blends of these materials with binding polymers, in order to optimize the OFET performance.

iii. Explore the polymorph transformations in evaporated and solution-processed thin films based on Ph-BTBT-10 employing thermal annealing procedures to improve the electrical properties of the prepared OFETs.

1.7 References

[1] G. Inzelt, “Rise and rise of conducting polymers,” Journal of Solid State Electrochemistry, vol. 15, no. 7–8, pp. 1711–1718, Jul. 2011, doi: 10.1007/s10008-011-1338-3.

[2] C. K. Chiang, Y. W. Park, A. J. Heeger, H. Shirakawa, E. J. Louis, and A. G. MacDiarmid, “Conducting polymers: Halogen doped polyacetylene,” J Chem Phys, vol. 69, no. 11, pp. 5098–5104, 1978, doi: 10.1063/1.436503.

[3] Y. Sun, Y. Liu, and D. Zhu, “Advances in organic field-effect transistors,” Journal of Materials Chemistry, vol. 15, no. 1. pp. 53–65, Jan. 2005. doi: 10.1039/b411245h.

[4] B. Geffroy, P. le Roy, and C. Prat, “Organic light-emitting diode (OLED) technology: Materials, devices and display technologies,” Polymer International, vol. 55, no. 6. pp. 572–582, Jun. 2006. doi: 10.1002/pi.1974.

[5] Y. Cui, L. Hong, and J. Hou, “Organic Photovoltaic Cells for Indoor Applications: Opportunities and Challenges,” ACS Appl Mater Interfaces, vol. 12, no. 35, pp. 38815–38828, Sep. 2020, doi: 10.1021/acsami.0c10444.

[6] G. P. Neupane, W. Ma, T. Yildirim, Y. Tang, L. Zhang, and Y. Lu, “2D organic semiconductors, the future of green nanotechnology,” Nano Materials Science, vol. 1, no. 4, pp. 246–259, Dec. 2019, doi: 10.1016/j.nanoms.2019.10.002.

[7] J. H. Burroughes, C. A. Jones, R. H. Friend, “New semiconductor device physics in polymer diodes and transistors”, Nature, vol.335, no.8, pp 137-141, Sep.1988. doi.org/10.1038/335137a0

[8] G. Horowitz, D. Fichou, X. Peng, Z. Xu, and F. Garnier, “A FIELD-EFFECT TRANSISTOR BASED ON CONJUGATED ALPHA-SEXITHIENYL,” Solid state Communications, vol.72, no.4, pp.381-384, Oct.1989, doi.org/10.1016/0038-1098(89)90121-X

[9] “Molecular and Polymer Semiconductors, Conductors, and Superconductors: Overview.”

[10] H. M. Schrickx, P. Sen, N. Balar, and B. T. O’Connor, “Strain alignment of conjugated polymers: Method, microstructure, and applications,” Cell Rep Phys Sci, vol.5, no.7, pp. 102076, Jul. 2024, doi: 10.1016/j.xcrp.2024.102076.

[11] L. Bürgi, T. J. Richards, R. H. Friend, and H. Sirringhaus, “Close look at charge carrier injection in polymer field-effect transistors,” J Appl Phys, vol. 94, no. 9, pp. 6129–6137, Nov. 2003, doi: 10.1063/1.1613369.

[12] A. F. Paterson et al., “Recent Progress in High-Mobility Organic Transistors: A Reality Check,” Advanced Materials, vol. 30, no. 36, pp. 181079, Sep. 06, 2018. doi: 10.1002/adma.201801079.

[13] J. Liu et al., “High mobility emissive organic semiconductor,” Nat Commun, vol. 6, no.10032, Dec. 2015, doi: 10.1038/ncomms10032.

[14] V. Coropceanu, J. Cornil, D. A. da Silva Filho, Y. Olivier, R. Silbey, and J. L. Brédas, “Charge transport in organic semiconductors,” Chemical Reviews, vol. 107, no. 4. pp. 926–952, Apr. 2007. doi: 10.1021/cr050140x.

[15] G. Schweicher, G. Garbay, R. Jouclas, F. Vibert, F. Devaux, and Y. H. Geerts, “Molecular Semiconductors for Logic Operations: Dead-End or Bright Future?,” Advanced Materials, vol. 32, no. 10. Wiley-VCH Verlag, Mar. 01, 2020. doi: 10.1002/adma.201905909.

[16] J. Y. Lee, S. Roth, and Y. W. Park, “Anisotropic field effect mobility in single crystal pentacene,” Appl Phys Lett, vol. 88, no. 25, Jun. 2006, doi: 10.1063/1.2216400.

[17] N. Boden, R. J. Bushby, J. Clements, B. Movaghar, K. J. Donovan, and T. Kreouzis, “Mechanism of charge transport in discotic liquid crystals 1 NOVEMBER 1995-II.”

[18] V. Coropceanu, J. Cornil, D. A. da Silva Filho, Y. Olivier, R. Silbey, and J. L. Brédas, “Charge transport in organic semiconductors,” Chemical Reviews, vol. 107, no. 4. pp. 926–952, Apr. 2007. doi: 10.1021/cr050140x.

[19] O. Ostroverkhova, “Organic Optoelectronic Materials: Mechanisms and Applications,” Chemical Reviews, vol. 116, no. 22. American Chemical Society, pp. 13279–13412, Nov. 23, 2016. doi: 10.1021/acs.chemrev.6b00127.

[20] G. Schweicher, Y. Olivier, V. Lemaur, and Y. H. Geerts, “What currently limits charge carrier mobility in crystals of molecular semiconductors?,” Israel Journal of Chemistry, vol. 54, no. 5–6. Wiley-VCH Verlag, pp. 595–620, 2014. doi: 10.1002/ijch.201400047.

[21] T. Yang et al., “Understanding, Optimizing, and Utilizing Nonideal Transistors Based on Organic or Organic Hybrid Semiconductors,” Advanced Functional Materials, vol. 30, no. 20. Wiley-VCH Verlag, May 01, 2020. doi: 10.1002/adfm.201903889.

[22] Z. Lu, C. Wang, W. Deng, M. T. Achille, J. Jie, and X. Zhang, “Meniscus-guided coating of organic crystalline thin films for high-performance organic field-effect transistors,” Journal of Materials Chemistry C, vol. 8, no. 27. Royal Society of Chemistry, pp. 9133–9146, Jul. 21, 2020. doi: 10.1039/d0tc01887b.

[23] F. G. Del Pozo et al., “Single crystal-like performance in solution-coated thin-film organic field-effect transistors,” Adv Funct Mater, vol. 26, no. 14, pp. 2379–2386, Apr. 2016, doi: 10.1002/adfm.201502274.

[24] X. Gu, L. Shaw, K. Gu, M. F. Toney, and Z. Bao, “The meniscus-guided deposition of semiconducting polymers,” Nature Communications, vol. 9, no. 1. no.534, Dec, 2018. doi: 10.1038/s41467-018-02833-9.

[25] O. Yildiz et al., “Role of Meniscus Shape on Crystallization of Molecular Semiconductors and Fluid Dynamics During Meniscus-Guided Coating,” Adv Funct Mater, vol.34, no.18, pp.2314131,May.2024, doi: 10.1002/adfm.202314131.

[26] F. Leonardi, S. Casalini, Q. Zhang, S. Galindo, D. Gutiérrez, and M. Mas-Torrent, “Electrolyte-Gated Organic Field-Effect Transistor based-on a Solution Sheared Organic Semiconductor Blend.” Advanced Materials, vol.28, no.46, pp.10311-110316, Dec 14,2016, doi.org/10.1002/adma.201602479

[27] S. Riera-Galindo, A. Tamayo, and M. Mas-Torrent, “Role of Polymorphism and Thin-Film Morphology in Organic Semiconductors Processed by Solution Shearing,” ACS Omega, vol. 3, no. 2, pp. 2329–2339, Feb. 2018, doi: 10.1021/acsomega.8b00043.

[28] Y. Yao, H. Dong, and W. Hu, “Charge Transport in Organic and Polymeric Semiconductors for Flexible and Stretchable Devices,” Advanced Materials, vol. 28, no. 22, pp. 4513–4523, Jun. 2016, doi: 10.1002/adma.201503007.

[29] S. Galindo, A. Tamayo, F. Leonardi, and M. Mas-Torrent, “Control of Polymorphism and Morphology in Solution Sheared Organic Field-Effect Transistors,” Adv Funct Mater, vol. 27, no. 25, pp.1700526,Jul. 2017, doi: 10.1002/adfm.201700526.

[30] M. Mas-Torrent et al., “Organic field-effect transistors (OFETs) of highly oriented films of dithiophene-tetrathiafulvalene prepared by zone casting,” Org Electron, vol. 9, no. 1, pp. 143–148, 2008, doi: 10.1016/j.orgel.2007.09.007.

[31] A. Tamayo et al., “Mobility anisotropy in the herringbone structure of asymmetric Ph-BTBT-10 in solution sheared thin film transistors,” J Mater Chem C Mater, vol. 9, no. 22, pp. 7186–7193, Jun. 2021, doi: 10.1039/d1tc01288f.

[32] S. Riera-Galindo, A. Tamayo, and M. Mas-Torrent, “Role of Polymorphism and Thin-Film Morphology in Organic Semiconductors Processed by Solution Shearing,” ACS Omega, vol. 3, no. 2, pp. 2329–2339, Feb. 2018, doi: 10.1021/acsomega.8b00043.

[33] H. M. Nguyen, A. V. Mader, S. De, and J. Vapaavuori, “Understanding nanodomain morphology formation in dip-coated PS-: B -PEO thin films,”

Nanoscale Adv, vol. 3, no. 17, pp. 4996–5007, Sep. 2021, doi: 10.1039/d1na00263e.

[34] A. Tamayo, S. Riera-Galindo, A. O. F. Jones, R. Resel, and M. Mas-Torrent, "Impact of the Ink Formulation and Coating Speed on the Polymorphism and Morphology of a Solution-Sheared Thin Film of a Blended Organic Semiconductor," Adv Mater Interfaces, vol. 6, no. 22, pp. 1900950, Nov. 2019, doi: 10.1002/admi.201900950.

[35] M. J. Ford et al., "High Mobility Organic Field-Effect Transistors from Majority Insulator Blends," Chemistry of Materials, vol. 28, no. 5, pp. 1256–1260, Mar. 2016, doi: 10.1021/acs.chemmater.5b04774.

[36] J. Yang, Z. Zhao, S. Wang, Y. Guo, and Y. Liu, "Insight into High-Performance Conjugated Polymers for Organic Field-Effect Transistors," Chem, vol. 4, no. 12. Elsevier Inc, pp. 2748–2785, Dec. 13, 2018. doi: 10.1016/j.chempr.2018.08.005.

[37] S. Riera-Galindo, F. Leonardi, R. Pfattner, and M. Mas-Torrent, "Organic Semiconductor/Polymer Blend Films for Organic Field-Effect Transistors," Advanced Materials Technologies, vol. 4, no. 9. pp.1900104, Sep. 01, 2019. doi: 10.1002/admt.201900104.

[38] J. Soeda, T. Okamoto, C. Mitsui, and J. Takeya, "Stable growth of large-area single crystalline thin films from an organic semiconductor/polymer blend solution for high-mobility organic field-effect transistors," Org Electron, vol. 39, pp. 127–132, Dec. 2016, doi: 10.1016/j.orgel.2016.09.006.

[39] T. Salzillo, F. D'Amico, N. Montes, R. Pfattner, and M. Mas-Torrent, "Influence of polymer binder on the performance of diF-TES-ADT based organic field effect transistor," CrystEngComm, vol. 23, no. 4, pp. 1043–1051, Jan. 2021, doi: 10.1039/d0ce01467b.

[40] H. Iino, T. Usui, and J. I. Hanna, "Liquid crystals for organic thin-film transistors," Nat Commun, vol. 6, Apr. 2015, doi: 10.1038/ncomms7828.

[41] J. Kim et al., "Optimal ambipolar charge transport of thienylenevinylene-based polymer semiconductors by changes in conformation for high-performance organic thin film transistors and inverters," Chemistry of Materials, vol. 25, no. 9, pp. 1572–1583, May 2013, doi: 10.1021/cm303908f.

[42] H. Ullah Khan et al., "Solvent vapor annealing in the molecular regime drastically improves carrier transport in small-molecule thin-film transistors," ACS Appl Mater Interfaces, vol. 5, no. 7, pp. 2325–2330, Apr. 2013, doi: 10.1021/am3025195.

[43] S. Kim, H. Yoo, and J. Choi, "Effects of Charge Traps on Hysteresis in Organic Field-Effect Transistors and Their Charge Trap Cause Analysis through Causal

Inference Techniques," Sensors, vol. 23, no. 4. MDPI, Feb. 01, 2023. doi: 10.3390/s23042265.

[44] M. Kim et al., "Donor–Acceptor-Conjugated Polymer for High-Performance Organic Field-Effect Transistors: A Progress Report," Advanced Functional Materials, vol. 30, no. 20. Wiley-VCH Verlag, May 01, 2020. doi: 10.1002/adfm.201904545.

[45] Z. A. Lamport, H. F. Haneef, S. Anand, M. Waldrip, and O. D. Jurchescu, "Tutorial: Organic field-effect transistors: Materials, structure and operation," J Appl Phys, vol. 124, no. 7, Aug. 2018, doi: 10.1063/1.5042255.

[46] D. Natali, J. Chen, F. Maddalena, F. García Ferré, F. Di Fonzo, and M. Caironi, "Injection Length in Staggered Organic Thin Film Transistors: Assessment and Implications for Device Downscaling," Adv Electron Mater, vol. 2, no. 8, pp.1600097, Aug. 2016, doi: 10.1002/aelm.201600097.

[47] M. Waldrip, O. D. Jurchescu, D. J. Gundlach, and E. G. Bittle, "Contact Resistance in Organic Field-Effect Transistors: Conquering the Barrier," Advanced Functional Materials, vol. 30, no. 20. pp.1904576, May. 2020. doi: 10.1002/adfm.201904576.

[48] C. Diouf et al., "'y function' method applied to saturation regime: Apparent saturation mobility and saturation velocity extraction," Solid State Electron, vol. 85, pp. 12–14, Jul.2013, doi: 10.1016/j.sse.2013.03.007.

[49] S. B. Mitta et al., "Electrical characterization of 2D materials-based field-effect transistors," 2D Materials, vol. 8, no. 1. pp.012002, Jan. 2021. doi: 10.1088/2053-1583/abc187.

[50] I. Miccoli, F. Edler, H. Pfnür, and C. Tegenkamp, "The 100th anniversary of the four-point probe technique: The role of probe geometries in isotropic and anisotropic systems," Journal of Physics Condensed Matter, vol. 27, no. 22. Institute of Physics Publishing, Jun. 10, 2015. doi: 10.1088/0953-8984/27/22/223201.

[51] W. Melitz, J. Shen, A. C. Kummel, and S. Lee, "Kelvin probe force microscopy and its application," Surface Science Reports, vol. 66, no. 1. Elsevier B.V., pp. 1–27, Jan.2011. doi: 10.1016/j.surfrep.2010.10.001.

Chapter 2:

Organic semiconductors based on charge transfer complexes of a BTBT derivative

Article I:

Charge transfer complexes of a benzothienobenzothiophene derivative and their implementation for organic field-effect transistors

2.1 Introduction and Objectives

Recent scientific research has increasingly focused on organic charge-transfer complexes (CTCs) compounds,[1] a class of substances that have been under study for decades. These compounds are binary systems comprising charge-donating (D) and charge-accepting (A) materials. In contrast to their parent compounds, which typically display unipolar semiconductor behavior, CTCs can exhibit a wide array of electrical properties, including ambipolar semiconductor behavior, metallic characteristics, and even superconductivity.[2], [3] A notable example illustrating this phenomenon is the binary compound tetrathiafulvalene–7,7,8,8-tetracyanoquinodimethane (TTF–TCNQ), discovered in 1973,[4] which shows metallic electrical conductivity compared to the insulating properties of its components.

In CTCs, the interaction between the highest occupied molecular orbital (HOMO) of the donor and the lowest unoccupied molecular orbital (LUMO) of the acceptor gives rise to a certain degree of electronic coupling. This coupling can be modulated by various factors, including the energy level differences, ionization potential, electron affinity, and supramolecular organization. As a result, a new energy band emerges in the CTC, influencing the degree of charge transfer (ρ) between the HOMO and LUMO (**Figure 2.1a**). Thus, this leads to the formation of a ground state with partial ionicity. The extent of charge transfer ultimately dictates the electrical characteristics of the final complexes. Adjustments between the HOMO (D) and LUMO (A) levels will play a role in ρ, while the supramolecular organization of the final complex will mainly define the bandwidth.[3] Theoretical efforts, including density functional theory (DFT) calculations and molecular dynamics simulations, aim to offer insights into establishing reliable degree charge transfer predictions and calculations.[4]

However, establishing reliable estimates remains a challenge due to the complex interplay between inter- and intra-molecular interactions.

The crystallization of CTCs has also a key influence on their electrical properties. Typically, alternating (or mixed) sequences of D and A molecules within a stack yield an insulating or semiconducting material. However, segregated stacks of equally spaced D and A molecules show high conductivities. Segregated stacks forming dimers along the stack are again insulating or semiconducting opening an energy gap due to a Peierls transition.[4], [5] Schematic representation of these assemblies is given in **Figure 2.1b**.

CTCs have long captivated organic chemists, offering opportunities for creating innovative compounds with tailored electrical properties, and with the primary goal to achieve metallic conductors and superconductors. Additionally, the interest in CTCs has recently resurfaced since it has been shown that they can also show other appealing properties such as photoluminescence,[6] photoconductivity,[7], [8] magnetoconductance,[9] thermo-electricity,[6] and ambipolarity.[10]

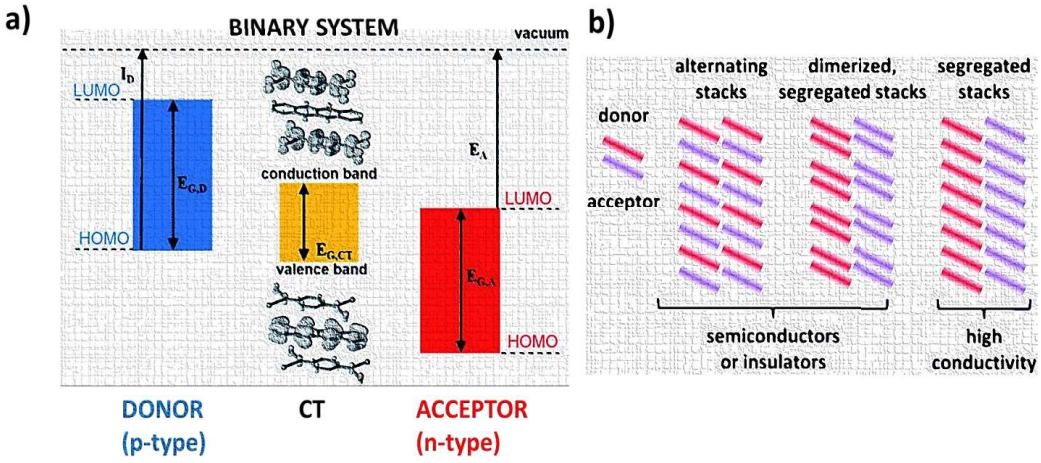


Figure 2.1. a) The donor band structure (blue), acceptor band structure (red), and an approximation of the CT band structure (yellow). The charge densities corresponding to the HOMO and the LUMO bands for the case of tetracene-tetracyanoquinodimethane (tetracene–TCNQ) CTC are indicated. b) Schematic representations of crystalline packings of 1:1 CTCs for mixed stack and segregated stack motifs. Adapted from ref.[5], [11], [12].

In the field of OFETs, CTCs are also attracting great interest since they can potentially exhibit ambipolar character. CTCs have been implemented as active layer in OFETs mainly as single crystals produced through methods such as drop casting,[13] or as thin films prepared by co-evaporation.[14] For instance, K. P. Goetz et al. fabricated single crystals based on dibenzotetrathiafulvalene–7,7,8,8-tetracyanoquinodimethane (DBTTF-TCNQ). They found that this 1:1 complex can crystallize in two polymorphs (α and β) that show different co-facial overlap and degree of charge transfer.[15] Both materials exhibited ambipolar transport when implemented in OFETs. However, the α polymorph, with a charge transfer degree of 0.5, showed an electron-dominating transport, while the β phase was nearly neutral, and the transport was hole-dominant (**Figure 2.2**).

In parallel,A. Babuji et al. explored surface doping via charge-transfer complex (CTC) formation in co-evaporated films of 2,7-dioctyl[1]benzothieno[3,2-

b][1]benzothiophene (C_8-BTBT) as the OSC and 2,2′-(perfluoronaphthalene-2,6-diylidene)dimalononitrile (F_6TCNNQ) as p-type dopant.[11] They demonstrated that CTC surface doping effectively increases the density of free carriers in the film, enhances the field-effect mobility and reduces the OFET threshold voltage (V_{th}).

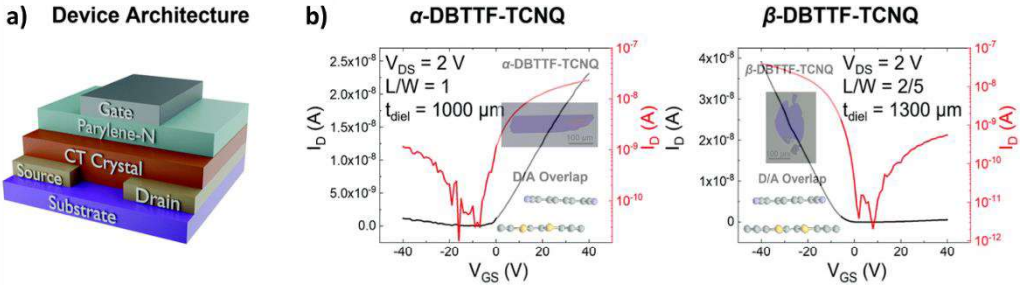


Figure 2.2. OFETs based on single crystals of two polymorphs (α and β) of DBTTF-TCNQ fabricated by evaporation showing distinct electrical characteristics. The scale bars in the images are 100 µm. Extracted from reference [15].

Despite all these exciting results achieved with these materials, for practical applications, there is a need to solution-process the organic layer using scalable methodologies. However, the low solubility of CTCs in organic solvents poses serious challenges, and strategies are being developed to produce films from solutions effectively.

The objective of this part of the thesis was to explore the possibility to solution-process CTCs to fabricate crystalline thin films to be used as active layers in OFETs. Specifically, the study aimed to develop and characterize CTCs formed between a BTBT derivative (i.e. C_8O-BTBT-OC_8) and TCNQ derivatives with different LUMO levels (i.e., TCNQ, F_2TCNQ, and F_4TCNQ) prepared using the cost-effective solution-based technique bar-assisted meniscus shearing (BAMS). Subsequently, the electrical properties of the films were investigated.

2.2 Summary of the results

The organic semiconductor 2,7-bis(octyloxy)[1]benzothieno[3,2-*b*]-benzothiophene (C_8O-BTBT-OC_8) has been acknowledged as a promising p-type organic semiconductor.[16] However, the formation of CTCs with this derivative had not been previously reported. Here, attempts were made to grow single crystals of CTCs based on C_8O-BTBT-OC_8 and the three above-mentioned TCNQ derivatives (**Figure 2.3a**). No complex was formed with the non-fluorinated acceptor, despite the favorable energy levels for charge transfer. On the other hand, complexes (C_8O-BTBT-OC_8)(F_2TCNQ) and (C_8O-BTBT-OC_8)(F_4TCNQ), were successfully crystallized and characterized. The crystal structure of the prepared complexes revealed a 1:1 stoichiometry and that the molecules stack along the *a*-axis, with molecules of the donor and acceptor alternating in an A-D-A-D pattern. The interplanar distances between C_8O-BTBT-OC_8 and F_2TCNQ or F_4TCNQ were similar, suggesting strong interactions. Moreover, through a spectroscopic analysis, an ionicity of 0.15 was estimated for (C_8O-BTBT-OC_8) (F_2TCNQ), which increased to 0.29 for (C_8O-BTBT-OC_8)(F_4TCNQ) in agreement with the more electron acceptor character of F_4TCNQ **(Figure 2.3a**). The results were further supported by DFT calculations.[17]

Subsequently, thin films of the CTCs were prepared by BAMS technique (**Figure 2.3b**), which is a solution-based technique compatible with roll-to-roll processes, under ambient conditions.[18], [19] This was performed by preparing a solution of the two individual components at a ratio of 1:1. In addition, the use of polystyrene (PS) as a binding polymer was also explored. After an optimization process modifying the deposition rate, the substrate temperature, and solvents, homogenous and crystalline films were successfully achieved for the CTC (C_8O-BTBT-OC_8) (F_4TCNQ). A combination of X-ray diffraction

(XRD) and spectroscopic analysis confirmed that these films maintained the same crystalline phase as the single crystals.

The (C_8O-BTBT-OC_8) (F_4TCNQ) films were then implemented in OFETs. The devices exhibited an n-type behavior with average electron mobility of $(1.0 \pm 0.2) \times 10^{-3}$ cm^2. V^{-1}. s^{-1} and a threshold voltage of 1.6 ± 6.4 V for the films with PS binder (**Figure 2.3.c**), while the mobility of pristine films was $(1.4 \pm 0.3) \times 10^{-4}$ cm^2. V^{-1}. s^{-1} and the threshold voltage 11.3 ± 5.2 V. This result was also in line with DFT calculations, which pointed to electron transport as the primary mode in this co-crystal system. It should be noted that the addition of the PS binder increases the device mobility by one order of magnitude and reduces the threshold voltage. Such device improvement can be attributed to a decrease in the interfacial charge trap density produced by the passivation of the SiO_2 dielectric with PS. Remarkably, the devices based on the CTC blended with PS not only exhibited a higher electrical performance but also the shelf-stability was significantly improved; devices stored and measured in ambient conditions were still working after 30 days.

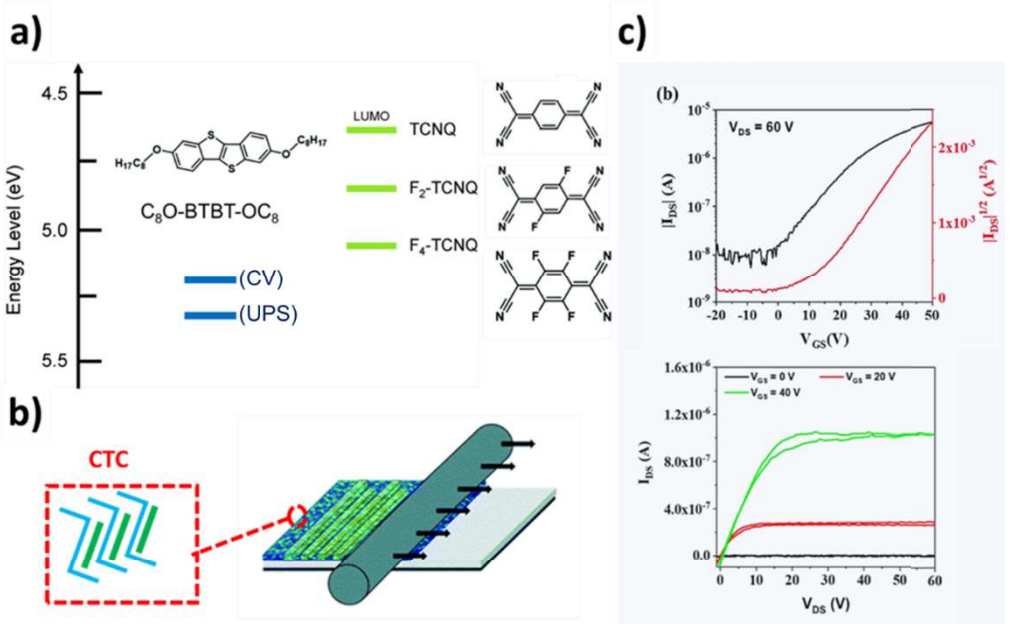


Figure 2.3. a) Molecular structures of the donor (C_8O-BTBT-OC_8) and acceptor (F_4TCNQ) compounds, and HOMO level (blue) estimated by Cyclic Voltammetry (CV) and Ultra-Violet Photoelectron Spectroscopy (UPS) for C_8O-BTBT-OC_8 and LUMO (green) energy levels of TCNQ, F_2TCNQ, and F_4TCNQ. b) Schematic illustration of co-assembling of the donor (C_8O-BTBT-OC_8) and acceptor (F_4TCNQ) to form thin films and illustration of the BAMS technique. c) Transfer and output characteristics of the OFETs based on (C_8O-BTBT-OC_8) (F_4TCNQ): PS. The channel length is 150 μm and the width/length ratio is 100.

2.3 Conclusions

In summary, we successfully prepared and characterized two novel CTC crystals using the organic semiconductor C_8O-BTBT-OC_8: (C_8O-BTBT-OC_8) (F_2TCNQ) and (C_8O-BTBT-OC_8) (F_4TCNQ). Both complexes crystallize in a 1:1 stoichiometry, forming alternating stacks of C_8O-BTBT-OC_8 with either F_2TCNQ or F_4TCNQ. Spectroscopic analysis revealed ionicity values of 0.16 for (C_8O-BTBT-OC_8) (F_2TCNQ) and 0.29 for (C_8O-BTBT-OC_8) (F_4TCNQ), indicating a higher charge transfer with the stronger electron acceptor F_4TCNQ. Moreover, homogeneous thin films of (C_8O-BTBT-OC_8) (F_4TCNQ) and (C_8O-BTBT-OC_8)(F_4TCNQ) blended with polystyrene (PS) were successfully prepared using the BAMS technique in ambient conditions. X-ray diffraction (XRD) and spectroscopic techniques confirmed that the films retained the same phase as the single crystal. Notably, these films exhibited n-type behaviour and good ambient stability.

All in all, we can conclude that, although challenging, large-area crystalline films of CTCs can be prepared by employing solution-based techniques compatible with scalable processes. Thus, this work opens the door to the possibility to continue exploring the properties of these materials not only for performing fundamental studies but also to develop practical applications.

2.4 References

[1] J. Zhang, W. Xu, P. Sheng, G. Zhao, and D. Zhu, “Organic Donor-Acceptor Complexes as Novel Organic Semiconductors”, Acc Chem Res, vol. 50, no. 7, pp. 1654–1662, Jul. 2017, doi: 10.1021/acs.accounts.7b00124.

[2] C. Mathur, R. Gupta, and R. K. Bansal, “Organic Donor-Acceptor Complexes As Potential Semiconducting Materials”, Chemistry - A European Journal, vol. 30, no. 23, Apr. 2024. doi: 10.1002/chem.202304139.

[3] D. Shen, W. C. Chen, M. F. Lo, and C. S. Lee, “Charge-transfer complexes and their applications in optoelectronic devices”, Mater Today Energy, vol. 20, Jun. 2021, doi: 10.1016/j.mtener.2021.100644.

[4] R. E. Peierls, W Kohn Fogle, and J. H. Perlstein, “Quantum Theory of Solids”, 1953.

[5] A. Opitz et al., “Thin films of electron donor-acceptor complexes: Characterisation of mixed-crystalline phases and implications for electrical doping”, Mater Adv, vol. 3, no. 2, pp. 1017–1034, Jan. 2022, doi: 10.1039/d1ma00578b.

[6] X. Li et al., “Transparent charge transfer complex with high thermoelectric performance”, Joule, vol. 7, no. 12, pp. 2814–2829, Dec. 2023, doi: 10.1016/j.joule.2023.10.008.

[7] C. Browning et al., “Synthesis, spectroscopic properties, and photoconductivity of black absorbers consisting of Pt (Bipyridine)(Dithiolate) charge transfer complexes in the presence and absence of nitrofluorenone acceptors”, J Am Chem Soc, vol. 136, no. 46, pp. 16185–16200, Nov. 2014, doi: 10.1021/ja506583k.

[8] H. Wang et al., “Photoconductive Charge Transfer Complexes as Charge Transport Layers for High Performance Inverted Perovskite Solar Cells”, Adv Funct Mater, vol. 32, no. 30, pp. 2201935, Jul. 2022, doi: 10.1002/adfm.202201935.

[9] T. H. Lee et al., “Magnetoconductance responses in organic charge-transfer-complex molecules”, Appl Phys Lett, vol. 99, no. 7, pp. 33071-33073, Aug. 2011, doi: 10.1063/1.3627170.

[10] R. Sanada, D. Yoo, R. Sato, K. Iijima, T. Kawamoto, and T. Mori, “Ambipolar Transistor Properties of Charge-Transfer Complexes Containing Perylene and

Dicyanoquinonediimines", Journal of Physical Chemistry C, vol. 123, no. 19, pp. 12088–12095, May 2019, doi: 10.1021/acs.jpcc.9b01453.

[11] A. Babuji et al., "Charge-Transfer Complexes in Organic Field-Effect Transistors: Superior Suitability for Surface Doping", ACS Appl Mater Interfaces, vol. 14, no. 39, pp. 44632–44641, Oct. 2022, doi: 10.1021/acsami.2c09168.

[12] K. P. Goetz, D. Vermeulen, M. E. Payne, C. Kloc, L. E. McNeil, and O. D. Jurchescu, "Charge-transfer complexes: New perspectives on an old class of compounds", J Mater Chem C Mater, vol. 2, no. 17, pp. 3065–3076, May 2014, doi: 10.1039/c3tc32062f.

[13] Y. Liu, Y. Han, X. Zhao, Y. Tong, Q. Tang, and Y. Liu, "Single-crystal tetrathiafulvalene microwire arrays formed by drop-casting method in the saturated solvent atmosphere", Synth Met, vol. 198, pp. 248–254, 2014, doi: 10.1016/j.synthmet.2014.10.039.

[14] H. Wada, D. de Caro, L. Valade, T. Ozawa, Y. Bando, and T. Mori, "Thin-film phases of organic charge-transfer complexes formed by chemical vapor deposition", Thin Solid Films, vol. 518, no. 1, pp. 299–304, Nov. 2009, doi: 10.1016/j.tsf.2009.06.040.

[15] K. P. Goetz et al., "Polymorphism in the 1:1 Charge-Transfer Complex DBTTF–TCNQ and Its Effects on Optical and Electronic Properties" Adv Electron Mater, vol. 2, no. 10, pp. 1600203, Oct. 2016, doi: 10.1002/aelm.201600203.

[16] T. Salzillo et al., "Enhancing Long-Term Device Stability Using Thin Film Blends of Small Molecule Semiconductors and Insulating Polymers to Trap Surface-Induced Polymorphs", Adv Funct Mater, vol. 30, no. 52, pp.2006115, Dec. 2020, doi: 10.1002/adfm.202006115.

[17] A. Ashokan, C. Hanson, N. Corbin, J. L. Brédas, and V. Coropceanu, "Electronic, vibrational, and charge-transport properties of benzothienobenzothiophene-TCNQ co-crystals", Mater Chem Front, vol. 4, no. 12, pp. 3623–3631, Dec. 2020, doi: 10.1039/d0qm00420k.

[18] S. Galindo, A. Tamayo, F. Leonardi, and M. Mas-Torrent, "Control of Polymorphism and Morphology in Solution Sheared Organic Field-Effect Transistors", Adv Funct Mater, vol. 27, no. 25, pp.1700526, Jul. 2017, doi: 10.1002/adfm.201700526.

[19] I. Temiño, F. G. Del Pozo, M. R. Ajayakumar, S. Galindo, J. Puigdollers, and M. Mas-Torrent, “A Rapid, Low-Cost, and Scalable Technique for Printing State-of-the-Art Organic Field-Effect Transistors”, Adv Mater Technol, vol. 1, no. 5, pp. 1600090, Aug. 2016, doi: 10.1002/admt.201600090.

Article I: Charge transfer complexes of a benzothienobenzothiophene derivative and their implementation as active layer in solution-processed thin film organic field-effect transistors

Lamiaa Fijahi, Tommaso Salzillo, Adrian Tamayo, Marco Bardini, Christian Ruzie, Claudio Quarti, David Beljonne, Simone D'Agostino, Yves H. Geerts and Marta Mas-Torrent

Chapter 3:

High throughput printing of DNTT derivatives

Article II: High throughput processing of dinaphtho[2,3-b:2',3'-f]thieno[3,2-b]thiophene (DNTT) organic semiconductors

3.1 Introduction and Objectives

The solubility and processability of organic semiconductors (OSCs) are key for developing practical applications in printing electronic devices.[1] One strategy to enhance the OSCs solubility involves functionalizing the molecular cores of benchmark OSCs with solubilizing groups that do not negatively interfere with the intermolecular packing of the materials.[2] Thus, many OSCs have been synthesized bearing linear or branched alkyl chains to improve their solubility in organic solvents. However, when processing OSCs as thin films using high-speed coating techniques, highly concentrated solutions (i.e., 10-20 $mg.ml^{-1}$) are required, which is challenging to achieve.[3], [4] Further, molecular design can also be employed to modify the electronic structure of OSCs and increase their stability in environmental conditions. [5]

As an example, pentacene has been used as the standard OFET material for a long time. However, since this material is not soluble it has to be processed by evaporation. In addition, pentacene air stability is low, which is reflected in the devices with an increase in the OFF current, a decrease in mobility, and a shift of the threshold voltage.[6][7] This is because benzene rings are linearly fused. To overcome this issue, an effective strategy for improving the (photo)oxidation stability of p-type OSCs is the incorporation of fused thiophene rings to form π-extended thienoacenes,[8], [9] which not only stabilizes the HOMO energy level but also enables the formation of a herringbone-type molecular packing similar to that of pentacene. Such type of molecular arrangement is known to be the most suitable one to realize high carrier mobility. The dinaphthothienothiophene (DNTT) and [1]Benzothieno[3,2-b]benzothiophene (BTBT) families have been widely used as standard OFET materials and have replaced pentacene for basic studies and applied research.[10]

Both OSC families show π-cores that assemble giving excellent electronic properties and stability, but they exhibit very poor processability. In particular, evaporated thin films of DNTT and BTBT have shown great OFET mobility as p-type OSCs.[11] However, the impossibility of processing this material from solution represents a serious drawback for using it in the field of printed electronics. For this reason, DNTT and BTBT derivatives bearing long alkyl chains have been synthesized to improve the solubility of the parent compound.[12] Further, it has been shown that the alky chains can facilitate molecular ordering in the solid state via van der Waals interactions.[13]

In particular, the 2,9-Dioctylnaphtho[2,3- b]naphtha[2',3':4,5]thieno[2,3-d]thiophene (C_8-DNTT) and 2,9-Didecyldinaphtho[2,3- b:2',3'-f]thieno[3,2-b]thiophene (C_{10}-DNTT) are two of the most studied soluble DNTT derivatives.[14] OFETs based on these materials have shown excellent hole mobilities, close to 8 $cm^2.V^{-1}.s^{-1}$ when deposited by vacuum deposition techniques and up to 10 $cm^2.V^{-1}.s^{-1}$ using solution-processed techniques.[15] [16], [17], [18], [19] Despite their excellent semiconducting properties and improved solution processability, C_8-DNTT and C_{10}-DNTT solubilities are still limited, making it challenging to prepare the highly concentrated solutions that are required for using high-throughput printing techniques. Additionally, more recently, it has been shown that the modification of the π-core shape from linear to crooked enhances the material solubility 30 times.[20] Numerous molecular designs based on bent π-conjugated materials have also been reported with the aim of removing molecular vibrations to achieve high performance (**Figure 3.1**).

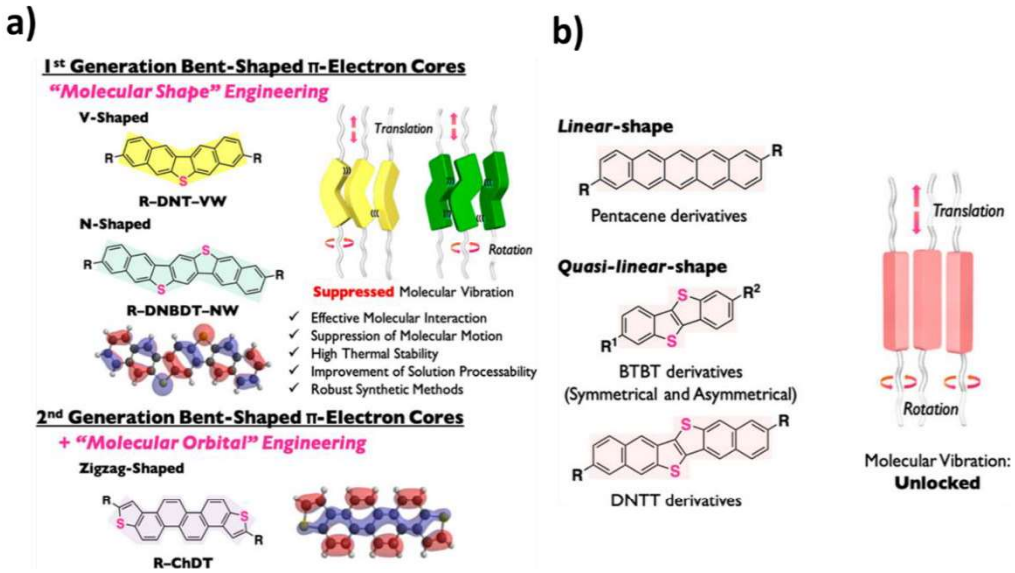


Figure 3.1. a) Molecular designs of first- and second-generation bent-shaped OSCs were carried out to reduce molecular vibrations. b) Molecular structures of representative organic semiconductors.[21]

As mentioned, DNTT derivatives with long alkyl groups or branched alkyl groups still exhibit limited solubility, posing challenges for high-throughput printing techniques. Few studies have reported the solution deposition of alkylated DNTT derivatives for OFET thin-film fabrication, using methods such as spin-coating, solution confinement, or low-rate solution shearing techniques.[22] We investigated the potential of three soluble DNTT derivatives to be processed using the bar-assisted meniscus shearing (BAMS) technique at high speed (i.e., 10 $mm.s^{-1}$).

The selected derivatives included the alkylated DNTT derivatives C_8-DNTT and C_{10}-DNTT, along with the S-core analogue 3,10-didecylnaphtho[2,1-b]naphtha[1',2':4,5] thieno[2,3-d]thiophene (S-DNTT-10) (**Figure 3.2**). Additionally, blends of these OSCs with polystyrene (PS) were also prepared, since it is known that the higher viscosity of the blended solutions can also help the thin film formation at fast coating speed. Subsequently, we conducted a thorough investigation into the properties of these thin films and evaluated the performance of the fabricated OFETs.

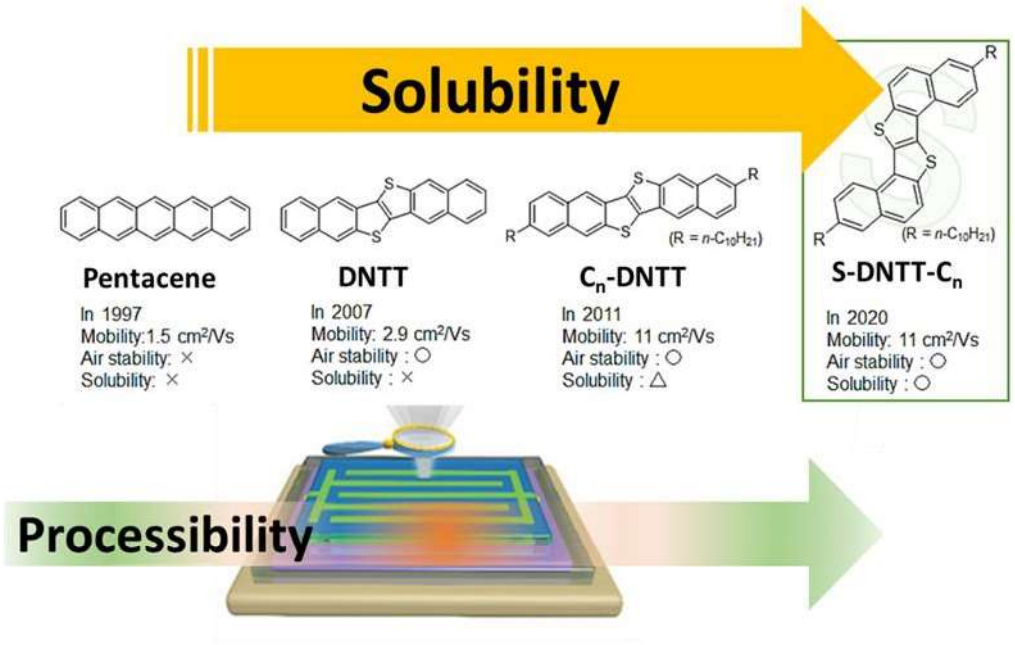


Figure 3.2. Organic semiconductors designed to improve solution processability and air stability (from pentacene to DNTT derivatives). Adapted from: https://www.tcichemicals.com/US/en/product/organic-electronics/organic-transistor/featured-articles/D5796.

3.2 Summary of the results

Thin films of the three above-mentioned materials were prepared by BAMS using solutions with a concentration of 22.60 mg.ml^{-1}. In the case of the C_8-DNTT and C_{10}-DNTT OSCs, a higher deposition temperature (i.e., 120 °C) was applied to avoid precipitation of the materials. In contrast, the preparation of thin films by BAMS of S-DNTT-10 was easier due to the higher solubility, which make it possible to use a lower coating temperature (i.e., 105 °C). The varying conditions for depositing these OSCs led to more cracks in the films made from the linear BTBT-core derivatives. Consequently, devices based on Cn-DNTT derivatives with long alkyl chains exhibited mobilities around 0.04 $cm^2 \cdot V^{-1} \cdot s^{-1}$. Moreover, implementing the use of PS contributed to achieving devices with reduced hysteresis and lower threshold voltage, suggesting an improvement in

the organic semiconductor/dielectric interface and a reduction in charge trapping. In the other hand, OFETs based on S-DNTT-10 demonstrated mobility values of almost two orders of magnitude higher than the films based on the linear Cn-DNTT derivatives, with an average mobility of 1.7 ± 0.6 cm^2. V^{-1}. s^{-1} and a V_{th} of −5.0 ± 0.8 V. This might be mainly due to the more homogeneous films with larger crystalline domains obtained with this semiconductor. Furthermore, the S-DNTT-10:PS blended films gave rise to an average mobility of 0.4 ± 0.2 cm^2.V^{-1}. s^{-1} and a V_{th} of 5.8 ± 0.4 V, indicating that, unlike other OSCs, the inclusion of PS did not enhance the electrical performance in this case. For comparison, representative saturation transfer characteristics of OFETs fabricated with the three OSCs are shown in **Figure 3.3**.

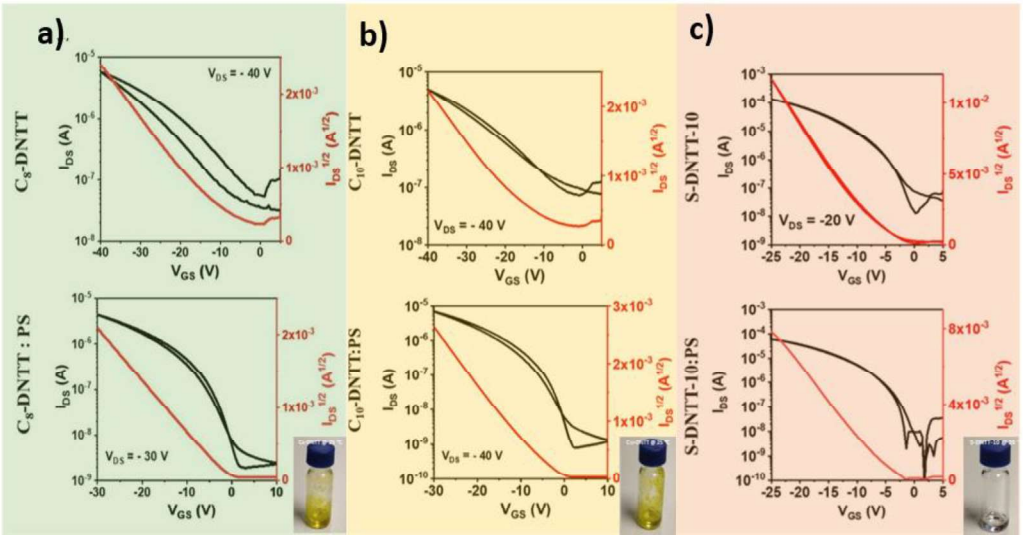


Figure 3.3. Saturation transfer characteristics of a) C_8-DNTT, b) C_{10}-DNTT, and c) S-DNTT-10 and their blends with PS. Insets: Images of the OSC solutions 2% wt. in chlorobenzene under ambient conditions.

3.3 Conclusions

In summary, here we investigated the viability of processing at high-speed functionalized DNTT derivatives and evaluated the impact of the different chemical modifications on the processability of the DNTT and the resulting thin film properties. We demonstrated that with the BAMS technique, both alkylated linear DNTT derivatives and S-DNTT-10 can be processed at high coating rates, resulting in crystalline thin films showing a good OFET performance. However, for depositing the alkylated linear DNTT derivatives the films have to be prepared at higher temperatures, and some cracks are observed in the films. On the other hand, the modification of the π-core shape from linear to S-shape gives rise to more soluble derivatives, which are much easier to process at a lower coating temperature. As a result, S-DNTT-10 films are more homogenous and reveal an OFET mobility almost two orders of magnitude higher than the devices based on films of the alkylated linear DNTT derivatives.

Consequently, our findings underscore the potential of DNTT derivatives for practical implementation in printed devices. Additionally, it was elucidated that the modification of the π-core shape represents a promising route for enhancing the solubility and, consequently, the processability, of organic semiconductors.

3.4 References

[1] M. M. Torrent and C. Rovira, “Novel small molecules for organic field-effect transistors: Towards processability and high performance”, Chem Soc Rev, vol. 37, no. 4, pp. 827–838, Mar. 2008, doi: 10.1039/b614393h.

[2] S. Inoue et al., “Effects of Substituted Alkyl Chain Length on Solution-Processable Layered Organic Semiconductor Crystals”, Chemistry of Materials, vol. 27, no. 11, pp. 3809–3812, Jun. 2015, doi: 10.1021/acs.chemmater.5b00810.

[3] S. Riera-Galindo, A. Tamayo, and M. Mas-Torrent, ‘Role of Polymorphism and Thin-Film Morphology in Organic Semiconductors Processed by Solution Shearing’, ACS Omega, vol. 3, no. 2, pp. 2329–2339, Feb. 2018, doi: 10.1021/acsomega.8b00043.

[4] X. Gu, L. Shaw, K. Gu, M. F. Toney, and Z. Bao, “The meniscus-guided deposition of semiconducting polymers”, Nature Communications, vol. 9, no. 534, Dec. 2018. doi: 10.1038/s41467-018-02833-9.

[5] K. Liu, B. Ouyang, X. Guo, Y. Guo, and Y. Liu, “Advances in flexible organic field-effect transistors and their applications for flexible electronics”, npj Flexible Electronics, vol. 6, no. 1, pp., Dec. 01, 2022. doi: 10.1038/s41528-022-00133-3.

[6] A. Maliakal, K. Raghavachari, H. Katz, E. Chandross, and T. Siegrist, “Photochemical stability of pentacene and a substituted pentacene in solution and in thin films”, Chemistry of Materials, vol. 16, no. 24, pp. 4980–4986, Nov. 2004, doi: 10.1021/cm049060k.

[7] M. Kitamura and Y. Arakawa, “Pentacene-based organic field-effect transistors”, Journal of Physics Condensed Matter, vol. 20, no. 18. pp. 184011, May. 2008, doi: 10.1088/0953-8984/20/18/184011.

[8] K. Takimiya, S. Shinamura, I. Osaka, and E. Miyazaki, “Thienoacene-based organic semiconductors”, Advanced Materials, vol. 23, no. 38, pp. 4347–4370, Oct. 11, 2011. doi: 10.1002/adma.201102007.

[9] M. E. Cinar and T. Ozturk, “Thienothiophenes, Dithienothiophenes, and Thienoacenes: Syntheses, Oligomers, Polymers, and Properties”, Chemical Reviews, vol. 115, no. 9. pp. 3036–3140, May. 2015. doi: 10.1021/cr500271a.

[10] K. Takimiya, I. Osaka, T. Mori, and M. Nakano, “Organic semiconductors based on [1]benzothieno[3,2- B][1]benzothiophene substructure”, Acc Chem Res, vol. 47, no. 5, pp. 1493–1502, May. 2014, doi: 10.1021/ar400282g.

[11] M. J. Kang, E. Miyazaki, I. Osaka, K. Takimiya, and A. Nakao, “Diphenyl derivatives of dinaphtho[2,3- b:2′,3′-f]thieno[3,2- b]thiophene: Organic

semiconductors for thermally stable thin-film transistors" ,ACS Appl Mater Interfaces, vol. 5, no. 7, pp. 2331–2336, Apr. 2013, doi: 10.1021/am3026163.

[12] K. Niimi, M. J. Kang, E. Miyazaki, I. Osaka, and K. Takimiya, "General synthesis of dinaphtho[2,3- b:2′,3′- f]thieno[3,2- b]thiophene (DNTT) derivatives", Org Lett, vol. 13, no. 13, pp. 3430–3433, Jul. 2011, doi: 10.1021/ol2010837.

[13] H. Y. Gao et al., "In-plane Van der Waals interactions of molecular self-assembly monolayer", Appl Phys Lett, vol. 106, no. 8, pp.081606, Feb. 2015, doi: 10.1063/1.4907777.

[14] M. J. Kang et al., "Alkylated dinaphtho[2,3-b:2′,3′-f]thieno[3,2-b]thiophenes (Cn-DNTTs): Organic semiconductors for high-performance thin-film transistors", Advanced Materials, vol. 23, no. 10, pp. 1222–1225, Mar. 2011, doi: 10.1002/adma.201001283.

[15] R. Hofmockel et al., "High-mobility organic thin-film transistors based on a small-molecule semiconductor deposited in vacuum and by solution shearing", Org Electron, vol. 14, no. 12, pp. 3213–3221, 2013, doi: 10.1016/j.orgel.2013.09.003.

[16] M. Sawamoto, H. Sugino, M. Nakano, and K. Takimiya, "High-performance solution-processed organic thin-film transistors based on a soluble DNTT derivative", Org Electron, vol. 46, pp. 68–76, 2017, doi: 10.1016/j.orgel.2017.04.001.

[17] M. Sawamoto, M. J. Kang, E. Miyazaki, H. Sugino, I. Osaka, and K. Takimiya, "Soluble Dinaphtho[2,3-b:2′,3′-f]thieno[3,2-b]thiophene Derivatives for Solution-Processed Organic Field-Effect Transistors", ACS Appl Mater Interfaces, vol. 8, no. 6, pp. 3810–3824, 2016, doi: 10.1021/acsami.5b10477.

[18] K. Kawabata, S. Usui, and K. Takimiya, "Synthesis of Soluble Dinaphtho[2,3-b:2′,3′- f]thieno[3,2- b]thiophene (DNTT) Derivatives: One-Step Functionalization of 2-Bromo-DNTT", Journal of Organic Chemistry, vol. 85, no. 1, pp. 195–206, 2020, doi: 10.1021/acs.joc.9b02585.

[19] Y. Yamaguchi et al., "Solution-Processable Organic Semiconductors Featuring S-Shaped Dinaphthothienothiophene (S-DNTT): Effects of Alkyl Chain Length on Self-Organization and Carrier Transport Properties", Chemistry of Materials, vol. 32, no. 12, pp. 5350–5360, 2020, doi: 10.1021/acs.chemmater.0c01740.

[20] T. Okamoto, "Next-generation organic semiconductors driven by bent-shaped π-electron cores", Polym J, vol. 51, no. 9, pp. 825–833, Sep. 2019, doi: 10.1038/s41428-019-0180-9.

[21] T. Okamoto et al., "Bent-Shaped p-Type Small-Molecule Organic Semiconductors: A Molecular Design Strategy for Next-Generation Practical

Applications", Journal of the American Chemical Society, vol. 142, no. 20, pp. 9083–9096, May 20, 2020. doi: 10.1021/jacs.9b10450.

[22] Z. Zhou et al., "Field-Effect Transistors Based on 2D Organic Semiconductors Developed by a Hybrid Deposition Method", Advanced Science, vol. 6, no. 19, pp. 1900775, Oct. 2019, doi: 10.1002/advs.201900775.

Article II: High throughput processing of dinaphtho[2,3-b:2',3'-f]thieno[3,2-b]thiophene (DNTT) organic semiconductors

Lamiaa Fijahi, Jinghai Li, Adrián Tamayo, Martina Volpi, Guillaume Schweicher, Yves H. Geerts and Marta Mas-Torrent

Chapter 4:

Crystal structure influence on the charge transport of Ph-BTBT-10 films

Article III: Phase transformations in evaporated Ph-BTBT-10 thin films and impact on the device performance

4.1 Introduction and Objectives

In recent years, significant efforts have been dedicated to exploring new π-conjugated molecules with high charge-carrier mobility for manufacturing thin films for organic field-effect transistors (OFETs). To facilitate wet deposition methods, the π-conjugated cores of OFET materials are often chemically modified with long hydrocarbon chains, improving their solubility in common organic solvents. In the crystal packing, these chains create bulky insulating layers between the semiconducting π-π stacks along the polycrystalline thin film, which can limit vertical transport while potentially favoring 2D transport. The primary challenges for optimizing the performance of materials with intrinsically high mobility include the poor homogeneity of solution-deposited thin films, their thermal stability and the control of their structure and morphology.

In 2014, Iino and co-workers tested a new molecule, 2-decyl-7-phenyl-[1]benzothieno[3,2-b][1]benzothiophene (Ph-BTBT-10, **Figure 4.1**) in OFETs, which emerged as a high-performance organic semiconductor (OSC) with mobilities around 10 $cm^2 V^{-1} s^{-1}$.[1] Ph-BTBT-10 bears a phenyl group attached to the large π-conjugated fused ring system of the benzothienobenzothiophene (BTBT) core and has a long, flexible decyl hydrocarbon chain to the opposite end to facilitate the formation of liquid crystal phases.[2]

Previous reports revealed that Ph-BTBT-10 exhibits two types of crystal structures: the so-called bulk and thin-film phases.[6], [10] The bulk phase features a bilayer-type structure with an interlayer spacing of 5.30 nm with a head-to-head molecular rearrangement, as shown in **Figure 4.1**.[10] In contrast, the thin-film phase comprises a periodic unit structure of a single layer with antiparallel molecular orientation within the layers (Figure 4.1).[6] This phase, with an interplanar spacing of 2.65 nm on the (001) plane, is a metastable

structure that forms on the substrate surface.[6] The thin-film phase transitions to the thermodynamically stable bulk structure upon thermal annealing above 110 °C.[3], [6] Further, at the smectic E (SmE) phase transition temperature of ~150 °C, the bilayer structure rearranges back into a single-layer packing. Additionally, the phase diagram of Ph-BTBT-10 includes a second, more disordered smectic A state, which is observed above 215 °C.

Previously, it was reported that spin-coated films of Ph-BTBT-10 crystallize forming a herringbone structure in the single-layer structure that gives an OFET mobility of 0.8 $cm^2 \cdot V^{-1} \cdot s^{-1}$. However, after annealing at 120 ºC such Ph-BTBT-10 films to convert them to the bilayer bulk crystal structure, a dramatic enhancement of the OFET mobility up to 13.9 $cm^2 \cdot V^{-1} \cdot s^{-1}$ was observed.[3], [4], [5] The performance of devices based on Ph-BTBT-10 is influenced by various factors such as the preparation method, the thermal history of the samples, orientation disorder, and the potential co-existence of different phases.[6] [7] The interaction between these phases and the corresponding transitions has been recently studied through structural and computational analyses to understand the underlying mechanisms.[7], [8], [9], [10] The investigations have been especially devoted to the understanding of the phase transition mechanism, with emphasis on the lattice transformation that allows the formation of the SmE monolayer structure starting from the bilayer bulk crystal. Such transformation can occur via either translational displacement of the Ph-BTBT-10 molecules or flip-flop movements. Hofer et al. [11] provided a detailed structural analysis of the SmE phase in Ph-BTBT-10 thin films using grazing-incidence X-ray diffraction (GIXD) and specular X-ray diffraction (XRR). The authors showed that molecular disorder in the bulk phase is responsible for the observed peak-broadening phenomena in the XRR spectra. Such disorder comes from the fact that the known head-to-head stacking within the crystalline phase is disturbed by

the statistic integration of reversed (or flipped) molecules. It was found that 7–15 % of the molecules are integrated in a reversed way, and these fractions are correlated with cooling rates during the sample preparation procedure.

In summary, Ph-BTBT-10 is a greatly promising high mobility OSC but with a complex polymorphism scenario. Our work in this chapter focuses on the fabrication of high-quality Ph-BTBT-10 thin films via two different techniques: solution shearing technique (i.e., BAMS) and thermal evaporation. A detailed examination of the films phase transitions and structural properties has been carried out together with an analysis of the crystal structure impact on the performance of the corresponding OFET devices.

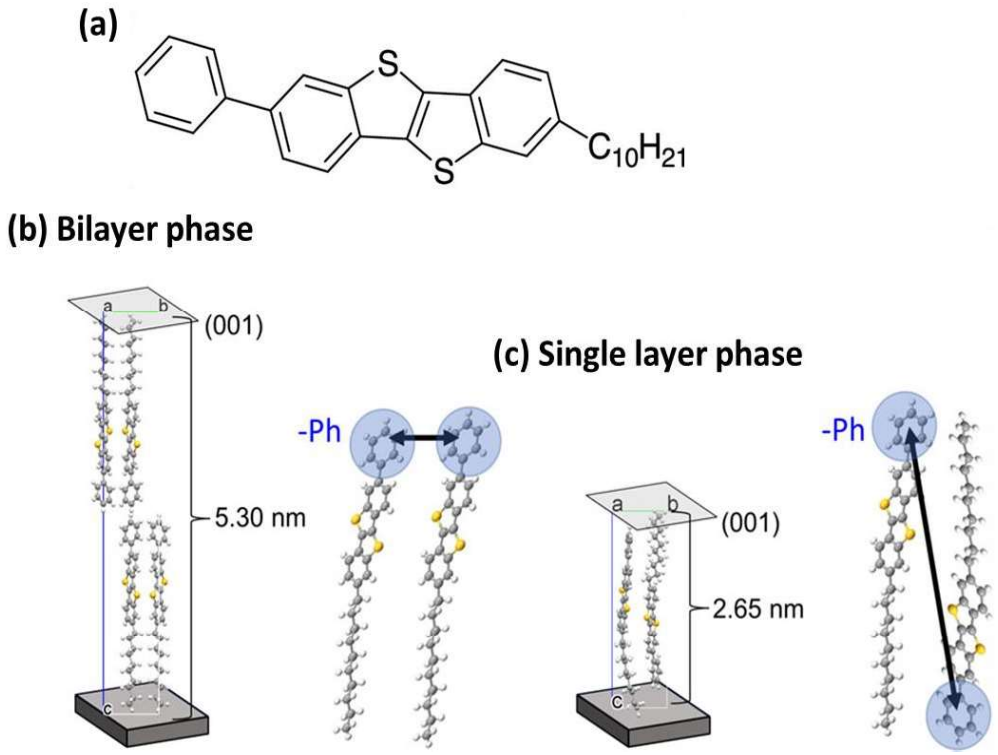


Figure 4.1. (a) Chemical structure of Ph-BTBT-10. Crystalline polymorphs of Ph-BTBT-10 in thin films: (b) Bilayer and (c) single layer phase. Extracted from reference [12].

4.2 Summary of the results of the evaporated Ph-BTBT-10 films

OFET devices based on Ph-BTBT-10 have been primarily fabricated using solution-based techniques, leveraging Ph-BTBT-10's solubility in organic solvents. Here (**Article III**), Ph-BTBT-10 thin films were thermally evaporated on Si/SiOx substrates. By performing XRR characterization at different heating and cooling temperatures, it was observed that the Ph-BTBT-10 evaporated films belonged to the single-layer phase and converted to a bilayer and SmE phases at 110 °C and 160 °C, respectively. The transitions observed in this study are consistent with previously reported data in the literature found for solution-deposited films.[5], [13] Additionally, when slowly cooling down the films to room temperature, the bilayer structure was formed confirming that is the most thermodynamically stable form. Further, it was found that rapid cooling from the SmE phase led to the preservation of the single-layer phase, indicating the kinetic control over the phase transitions.

The as-evaporated films and evaporated films annealed at 130 °C and 140 °C were then investigated using XRR and Kelvin Probe Force Microscopy (KPFM). Films annealed at 130 °C exhibited a mixture of single-layer and bilayer phases, while those annealed at 140 °C transitioned completely to the bilayer structure. By KPFM it was found that the bilayer structure exhibited minimal surface potential variation due to the nullification of electrical dipoles, whereas the single-layer structures displayed higher variability in surface potential due to defects and net dipole moments.

When integrated into OFETs, the films demonstrated a notable increase in mobility and a reduction in threshold voltage with increased annealing

temperature. The as-evaporated thin film devices exhibited an average OFET mobility of 0.2 ± 0.15 $cm^2 \cdot V^{-1} \cdot s^{-1}$ and a threshold voltage of -21.2 ± 2.0 V. Devices annealed at 130 °C demonstrated a mobility of 1.5 ± 0.4 $cm^2 \cdot V^{-1} \cdot s^{-1}$ and a threshold voltage of -17 ± 2 V. Finally, the mobility increased further up to 4.1 ± 0.3 $cm^2 \cdot V^{-1} \cdot s^{-1}$ in the films annealed at 140 °C, with a threshold voltage of -10.0 ± 0.9 V. Thus, the devices based on bilayer structure achieved the highest mobility, indicating that the conversion from the single-layer phase to the bilayer phase optimizes the electrical properties (**Figure 4.2a-b**). This performance enhancement was attributed partly to a reduced charge trapping and decreased electrostatic disorder after annealing, which was evident from the estimated density of interfacial hole traps. The as-evaporated devices showed a trap density of approximately $6 \cdot 10^{12}$ $eV^{-1} \cdot cm^{-2}$, which was reduced to $2 \cdot 10^{12}$ $eV^{-1} \cdot cm^{-2}$ in the devices annealed at 140 ^{o}C (**Figure 4.2c**).

In summary, this research highlights the critical role of thermal treatments in modulating the polymorphic structure of Ph-BTBT-10 thin films, thereby optimizing their electrical properties. The findings provide valuable insights into improving the performance of Ph-BTBT-10-based electronic devices through precise control of thin film deposition and annealing processes.

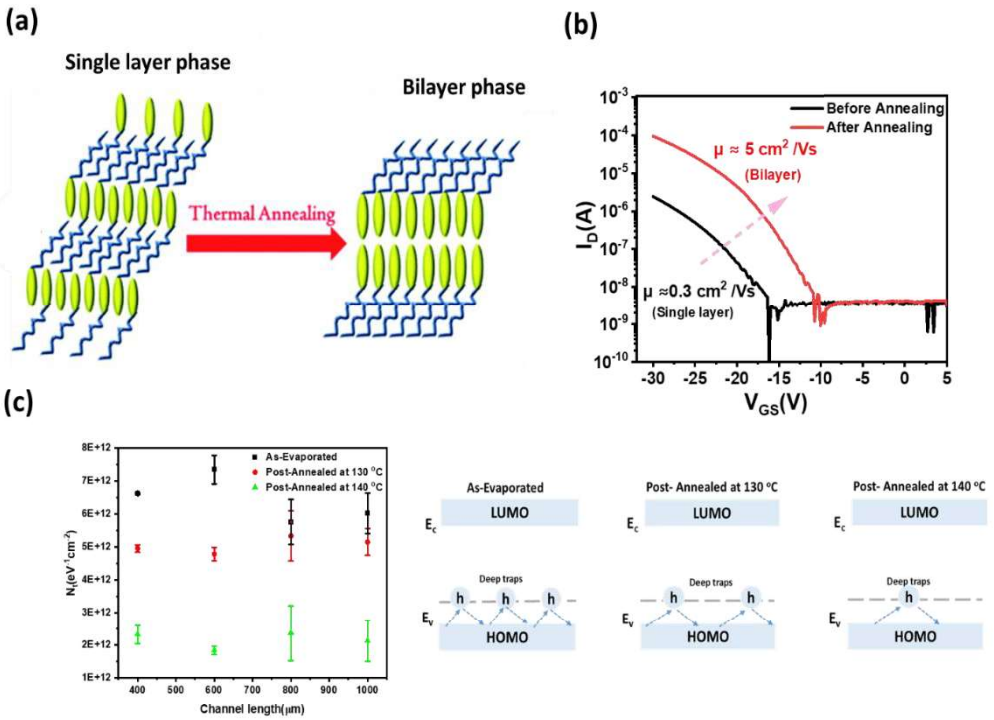


Figure 4.2. (a) Schematic illustration of the transition from the single layer structure to the bilayer structure upon thermal annealing (yellow ellipse represents a rigid core and blue line represents the side alkyl chains). Extracted from [14]. (b) Saturation transfer characteristics of OFETs of evaporated Ph-BTBT-10 before and after annealing (V_D=-20V). Channel length L=1000 μm. (c) Interfacial traps estimation using the sub-threshold swing and schematic diagrams of the trap distribution in the devices.

Article III: Phase transformations in evaporated Ph-BTBT-10 thin films and impact on the device performance

Lamiaa Fijahi, Shunya Yan, Ann Maria James, Adrián Tamayo, Jinghai Li, Carmen Ocal, Esther Barrena, Roland Resel, Marta Mas-Torrent

Phase transformations in evaporated Ph-BTBT-10 thin films and impact on the device performance

Lamiaa Fijahi,[1] Shunya Yan,[1] Ann Maria James,[2] Adrián Tamayo,[1] Jinghai Li,[1] Carmen Ocal,[1] Esther Barrena,[1,*] Roland Resel,[2,*] Marta Mas-Torrent[1,*]

[1] Institut de Ciència de Materials de Barcelona, ICMAB-CSIC, Campus UAB, 08193 Bellaterra, Spain. E-mail: e.barrena@csic.es; mmas@icmab.es
[2] Institute of Solid State Physics, Graz University of Technology, Petersgasse 16, Graz 8010, Austria. E-mail: roland.resel@tugraz.at

Abstract:

This paper reports on the phase transformation occurring in evaporated thin films of the organic semiconductor Ph-BTBT-10 by performing in situ temperature-dependent X-ray reflectivity (XRR) studies. The films crystallise in a single layer structure which converts to a bilayer phase in the temperature range of 110-140 °C; at further elevated temperatures, a liquid-crystal phase is formed. XRR combined with Kelvin Probe Force Microscopy data points out that only at the highest annealing temperature the phase transformation is completed. In a subsequent step, the films have been investigated as active layers in organic-field-effect transistors. An enhanced performance is observed in the annealed films with a higher mobility and reduced level of charge traps. The best electrical characteristics are realised when the bilayer transformation is fully accomplished.

KEYWORDS: Organic semiconductor, Ph-BTBT-10, OFET, polymorphism, X-ray reflectivity, Kelvin Probe Force Microscopy

1. Introduction

In recent years, significant advancements have been achieved in the development of organic semiconductors (OSCs) as active layers in organic field-effect transistors (OFETs), showcasing high performance and opening up wide possibilities for innovative applications in areas such as flexible/wearable electronics and Internet of Things (IoT).[1,2] One major advantage of OSCs is the possibility to tune the thin film structural and electrical characteristics, or the material processability, by chemical design.[3–7]

Small molecule OSCs tend to form ordered crystalline films, which typically result in a high charge carrier mobility. However, since the molecules are bound to each other through non-directional weak intermolecular interactions, small molecule OSCs can commonly crystallise forming different polymorphs.[8] Such polymorphs exhibit different overlaps of their frontier orbitals (i.e., charge transfer integrals), which significantly influences the material charge transport mobility. Noticeably, the mobility of different polymorphs can vary by orders of magnitude.[9,10] Another key aspect to be considered is the stability of the OSC polymorphs since they often exhibit a metastable character.[11–13]

The processing conditions play a pivotal role on the OSC crystallisation. It is known that when OSCs are processed from solution, parameters such as solvent, concentration, temperature or deposition rate effect the molecules self-assembly. [9,14,15] Likewise, thermally evaporated OSCs are affected by factors

such as deposition rate, base pressure and substrate temperature.[16,17] Alternatively, post-processing methods, such as solvent vapour annealing or thermal treatments can also enhance thin film crystallinity or induce the formation of specific polymorphs.[18–21] Typically, these processes offer the advantage to give rise to the most thermodynamically stable form.

A notable example of the impact of the molecular packing on the charge transport properties can be found with the p-type OSC 2-Decyl-7-phenyl[1]benzothieno[3,2-b][1]benzothiophene (Ph-BTBT-10), Figure 1a. Ph-BTBT-10 shows polymorphism, mainly caused by the asymmetry of its molecular structure.[22–28] This molecule crystallises in the bulk following a lamellar bilayer head-to-head arrangement (Figure 1c), resulting in a stacking periodicity twice the molecular length (i.e., 5.3 nm), with the aromatic units arranged in a herringbone manner. Additionally, a metastable thin film phase has also been reported, where the molecules adopt a lamellar single layer structure with an interlayer spacing corresponding to the molecular length (Figure 1b). Further, the asymmetric nature of the molecule also favours the formation of liquid crystalline states at temperatures above 145°C with a head-to-tail arrangement of the molecules and a single layer periodicity.

Ph-BTBT-10 has also been investigated as an active layer in OFETs giving excellent mobility values.[22,29–31] Ph-BTBT-10 devices have been mainly fabricated employing solution-based techniques taking advantage of its good

solubility in organic solvents. It was previously found that the as-prepared thin films often crystallise in the single-layer phase, but a thermal annealing process can convert them to the bulk bilayer phase, leading to a significant increase in device mobility.[22] In addition, it was reported that molecular orientation disorder inside the bilayer phase can also be present in the films, which could potentially hamper the device's performance.[23]

In this paper we deeply investigate the phase transitions taking place in evaporated films of Ph-BTBT-10 whilst they are heated and cooled at different temperatures at controlled rate. Structural transitions from the single layer phase to the bulk structure and the Smectic E phase have been found. The effect of performing an annealing post-treatment in the evaporated thin films was also investigated by X-ray reflectivity (XRR) and Kelvin Probe Force Microscopy (KPFM). It was found that to ensure reaching the full bilayer phase the temperature and time annealing need to be optimised. Finally, the films were implemented as active layers in OFETs. An optimised device performance, reaching an average mobility of around 4 $cm^2 \cdot V^{-1} \cdot s^{-1}$, was realised when the complete bulk phase transformation was achieved. Remarkably, a clear adverse impact on the electrical performance was noticed in the films where the full phase transformation was not accomplished.

2. Results and discussion

Thin films of Ph-BTBT-10 with a thickness of 20 nm were prepared by physical vapour deposition on bare Si/SiO_x substrates. The thin film morphology as well as the crystalline properties of the Ph-BTBT-10 films were investigated by XRR analysis. The XRR curves were recorded on the as-deposited film and at various temperatures during a controlled heating process (0.67 °C·min^{-1}), providing insights into the structural transition of Ph-BTBT-10 from the single layer (thin film) phase to the bilayer phase (Figure 2a). A single layer phase is found at low temperatures (from 25 ºC to 100 ºC) exhibiting characteristic peaks at 0.236 and 0.473 Å^{-1}.[32] The bilayer structure is observed in the temperature range from 110 °C up to 140 °C, and is characterized by additional peaks at 0.118 Å^{-1} and 0.355 Å^{-1}and 0.592 Å^{-1}.[23] Furthermore, at a temperature of 160 ºC and above, the bilayer structure melts leading to the single-layer smectic E (SmE) liquid-crystal structure.[24] These temperature transitions are quite in agreement with published data in literature (the temperature transition from the single layer to the bulk phase was reported to be 115 °C and the transition to SmE at 143 °C).[22,23] As shown in Figure 2b, during the controlled cooling (0.67 °C·min^{-1}), the phase transition from SmE to the bilayer structure was discerned at a temperature of 125 °C. Under the specified experimental conditions, a transition from the bilayer structure to the single layer phase was not detected, which can be attributed to the fact that the bilayer phase is the most

thermodynamically stable polymorph. However, it should be noticed that films annealed at 180ºC exhibiting the SmE phase, when they were rapidly cooled to room temperature, a single layer structure was preserved (Figure S1).

Following, the conversion of the single layer structure to the bilayer phase thermal annealing was investigated in detail. For this purpose, we studied the structural features of two thin films upon a thermal treatment in vacuum: one was annealed at 130 ºC (10 min) and the other film at 140 ºC (20 min). The films were cooled down to room temperature in vacuum. Besides Kiessig fringes, the XRR curves of these films reveal also diffraction features allowing structural analysis based on the Bragg peaks positions (Figure 2b, Figure S2). The three order reflections observed for the as-deposited Ph-BTBT-C10 films indicate the formation of the single layer phase (black curve in the Figure 2b),[32] whereas the distinctive fingerprints of the bilayer structure are observed for the annealed film at 140ºC (blue curve), as described above.[32] In contrast, the XRR curve for the thin film annealed at 130°C points out to the presence of a certain mixture of both, bilayer and single layer.

The films were also characterized by Kelvin Probe Force Microscopy (KPFM), which provides simultaneously the topography and surface potential. We have recently demonstrated that KPFM can be a powerful tool to distinguish different polymorphic forms of Ph-BTBT-10 and their coexistence at the nanoscale.[27] We reported that the bilayer packing does not lead to significant surface potential

differences with the substrate due to the compensation of the electrical dipole existing for each half bilayer (in which all molecules have the same orientation), resulting in a zero net electrical dipole. In contrast, for the single-layered packing of Ph-BTBT-10 obtained at room temperature, we have found that structural defects in the form of flipped molecules result in local uncompensated electric fields (i.e., a net electrical dipole). Depending on the direction of the net electrical dipole, it can result in a larger or lower surface potential compared to the bi-layer phase. Figure 3a shows a representative topographical image of the as-prepared films, consisting of terraced mounds. A height profile is shown in Figure 3c along the line indicated in the topographical image. The measured step height of 2.8± 0.1 nm corresponds to one molecule high terraces of Ph-BTBT-10, in agreement with the XRR data. The surface potential image is shown in Figure 3b, which displays a rather uniform surface potential, except in some areas with lower values that are attributed to defects in the underlying film. Upon post-annealing at 130 °C, the morphology develops two kinds of differentiated regions. The characteristic mounds observed in the non-annealed films are still visible at the top-right part of Figure 3d. Remarkably, this region is distinguished by a higher surface potential (Figure 3e). A magnified area is shown in the supporting information (Figure S3). The rest of the image displays quite large terraces (several microns), some of them with the step height of the bilayer stacking (5.5± 0.1 nm). Both regions, mounds and large terraces, are clearly

distinguished in the surface potential in larger-scale images (Figure S4). Thus, from KPFM and XRR it can be concluded that the film is a mixture of the single layer and bilayer structural phases laterally separated. On the other hand, the morphology suffered a drastic change in the films that were post-annealed at 140 °C. The topmost surface of the entire film displays now terraces with two heights (≈ 2.7 and 5.5 nm), meaning that the topmost layer corresponds to molecular assemblies forming either a single layer or bilayer terraces. Remarkably, the surface potential has become much more homogeneous. In view of this result and the XRR data, it is concluded a full conversion of the film into the bilayer structure.

The as prepared and annealed films were then investigated as active layers in OFETs. For this, the Si/SiO_x was used as gate/dielectric and gold source and drain contacts were evaporated on top of the films. The transfer characteristics are shown in Figure 4 and their corresponding output characteristics are displayed in Figure S5 and Figure 4. The three films displayed a p-type behaviour with good modulation of the current and low hysteresis. Nevertheless, it is visible from the transfer curves that the measured drain-source current (I_{DS}) increases in the annealed samples, which is accompanied by a shift of the curves towards less negative gate-source voltages (V_{GS}). The average OFET mobility and threshold voltage calculated for the as-evaporated thin films devices was 0.2 ± 0.15 $cm^2 \cdot V^{-1} \cdot s^{-1}$ and -21.2 ± 2.0 V, respectively. A significant increase in

the mobility together with a reduction of the threshold voltage was observed with the devices based on annealed films: 1.5 ± 0.4 $cm^2 \cdot V^{-1} \cdot s^{-1}$ and -17 ± 2 V, respectively, for the films annealed at 130 °C, and 4.1 ± 0.3 $cm \cdot^2 V^{-1} \cdot s^{-1}$ and -10.0 ± 0.9 V, for the films annealed at 140 °C. These data are summarised in Table S1. Thus, the first annealing treatment leads to a device mobility improvement of almost one order of magnitude, which increases almost three-fold when the films are annealed at higher temperatures. This result elucidates the impact of the Ph-BTBT-10 polymorphism on the electrical properties in evaporated films. The bilayer structure leads to enhanced mobility, and the highest mobility is only realised when the conversion from the single layer to the bulk form is maximised.

Furthermore, the shift of the threshold voltage to less negative values in the annealed films can be associated to a reduction of charge trapping. Thus, we proceed to estimate the density of the interfacial hole traps from the subthreshold swing (SS) (see experimental section). We observed a gradual reduction of the traps density from the non-annealed films to the films treated with an increasing annealing temperature, going from around $6 \cdot 10^{12}$ $eV^{-1} \cdot cm^{-2}$ in the as-deposited devices down to $2 \cdot 10^{12}$ $eV^{-1} \cdot cm^{-2}$ in the devices annealed at 140ºC (Figure 5). We have previously shown that films with single-lamellar packing have a variable level of electrostatic disorder that causes a broadening of the highest occupied molecular orbital (HOMO) levels, as observed by ultraviolet

photoelectron spectroscopy. [27] Among other factors, electrostatic disorder is associated with charge trapping.[33] Thus, the temperature treatment simultaneously increases the device mobility and reduces the interfacial traps, while converting the single layer phase to a bilayer structure.

3. Conclusions

In conclusion, herein the structural properties of evaporated Ph-BTBT-10 thin films were investigated in-depth. XRR data carried out at different temperatures allowed for the identification of the single layer, bilayer and SmE phases. Subsequently, the as-deposited thin films belonging to the single layer structure were annealed to be converted to the bulk bilayer form. Thanks to a combined characterization by XRR and KPFM, it was proved that only the films annealed at 140 ºC had been fully transitioned to the bilayer structure, while the single layer phase was still partially present in the films annealed at 130 ºC. The OFET devices based on the evaporated Ph-BTBT-10 thin films exhibited enhanced mobility and reduced levels of charge traps after the films had been annealed. However, the best mobility was only realised in the films that had been fully transformed to the bulk phase.

Thus, this work elucidates the importance of controlling thin film polymorphism to achieve high performing and reproducible devices. Temperature post-annealing treatment is a promising route to reach thermodynamic polymorphs, but it is key to realise a full phase transformation to

ensure an optimised performance and a low device-to-device variability.

4. Experimental section

Materials

Ph-BTBT-10 was purchased from TCI and used without any additional purification. Arsenic p-doped silicon substrates were purchased from Siegert wafer (SiO_x thickness was 200 nm, C = 17.26 $nF \cdot cm^{-2}$).

Thin films growth

Physical vapor-deposited Ph-BTBT-10 films (20 nm thick) for in situ XRR studies with temperature were prepared in a high-vacuum chamber with a base pressure of (10^{-6} mbar) using a resistively heated tungsten boat and a quartz microbalance for in-situ thickness control. The substrate surface was kept at room temperature, and the deposition rate was (0.28 $Å \cdot s^{-1}$).

Thermal treatment

The in situ XRR studies with temperature were performed at a temperature range from 25 ºC to 180 ºC in a controlled and continuous manner using a commercially available domed hotstage DHS900 under inert (nitrogen) conditions, AntonPaar.[34] The sample series were annealed with at defined heating and cooling rate of 0.67 $ºC \cdot min^{-1}$.

Thin-film characterization

X-ray diffraction measurements were carried out with a D-5000 model Siemens diffractometer that used Cu Kα radiation 1.5418 Å. Surface topography, phase and thin film thickness were examined by a 5500LS SPM system from Agilent Technologies and subsequent data analysis was performed by using Gwyddion 2.56 software. X-ray reflectivity (XRR) measurements were made using a Panalytical Empyrean reflectometer. On the primary side, a multilayer mirror was used to render the parallel beam; on the secondary part, a combined set up with a receiving slit, a Soller slit and a PANalytical PIXCEL3D detector was used. The 2θ (angular scans) have been transformed to scattering vector notation using $q_z = 4\pi/\lambda \sin\theta$, where q_z is the scattering vector perpendicular to the substrate surface, λ is the wavelength of the CuKα radiation (1.5418 Å) and θ is the scattering angle.

AFM data were acquired by using a Cypher ES Environmental AFM instrument, from Asylum Research (Oxford Instruments), the topographic measurement was performed in Tapping mode at RT with an N_2 gas environment to minimize moisture and oxidizing effects. The silicon tips (from BudgetSensors) with a Ti/Ir (5/20 nm) coating and a nominal spring constant of 2.8 (N/m) were employed. Data were analysed using the Igor Pro software provided by Asylum Research (AR).

Device fabrication and characterization

Si/SiO_x (200 nm thick) substrates were cleaned by ultrasonication (15 min in acetone plus 15 min in isopropanol) before being introduced into the evaporation chamber. The substrates underwent a heat treatment at 250 °C for 15 minutes to eliminate all gases and water absorbed on the SiO_x surface. Then, Ph-BTBT-10 films were evaporated at a deposition rate of ≈2 Å/min under high vacum conditions. Following this, the prepared films were heated at 130 °C for 10 minutes or 140 °C for 20 minutes. Finally, 30 nm of gold was thermally evaporated on the films using a shadow mask to form the top-contract electrodes, with a channel width (W) of 15 mm and channel lengths (L) ranging from 1000 to 200 μm. After evaporation, samples were stored in a glovebox.

The transfer and output characteristics of the devices were measured with an Agilent B1500A semiconductor device analyser connected to the samples with a Karl SUSS probe station, at ambient conditions. The devices were carefully isolated by scratching the film edges before performing the measurements. The characteristic field-effect mobility (μ) and threshold voltage (V_{th}) parameters of the transistors were extracted in the saturation regime using the following classic MOSFET equations:

$$\mu = \left(\frac{\partial\sqrt{|I_{DS}|}}{\partial V_{GS}}\right)^2 \cdot \frac{2L}{W} \cdot \frac{1}{C}$$

$$I_{DS} = \frac{W}{2L}\mu C(V_{GS} - V_{th})^2$$

where W and L are the width and length of the channel, respectively, and C is the dielectric capacitance per unit area.

The density of traps (N_t) was calculated employing the sub-threshold swing (*SS*) [35] according to:

$$SS = \frac{\partial V_{GS}}{\partial(\log I_{DS})}, \qquad N_t = \frac{C}{e^2} \cdot \left[\frac{e \cdot SS}{k_B \cdot T \cdot ln10} - 1\right]$$

Where e is the electron charge, k_B is the Boltzmann constant, C is the capacitance per unit area of the dielectric, T the absolute temperature and V_{GS} and I_{DS} the applied gate voltage and the measured drain current, respectively.

Supporting Information.

Additional electrical measurements and KPM and X-ray data.

Acknowledgements

This work was funded by European Union's Horizon 2020 research and innovation programme under the Marie Skłodowska-Curie grant agreement No 811284 (UHMob) and by MCIN/AEI/10.13039/501100011033/ERDF,UE with project SENSATION PID2022-141393OB-I00, and through the "Severo Ochoa" Programme for Centers of Excellence in R&D (FUNFUTURECEX2019-000917-S) and by the Generalitat de Catalunya (2021-SGR-00443). This study is part of the Advanced Materials programme (In-CAEM project) and is partially supported by MCIN with funding from European Union NextGenerationEU (PRTR-C17.I1). S.Y. is financially supported by the China Scholarship Council (CSC) under Grant No. 202006990034. This work has been carried out within the framework of the doctoral PhD program of Material Science, Department of Physics of the Universitat Autonoma de Barcelona (UAB).

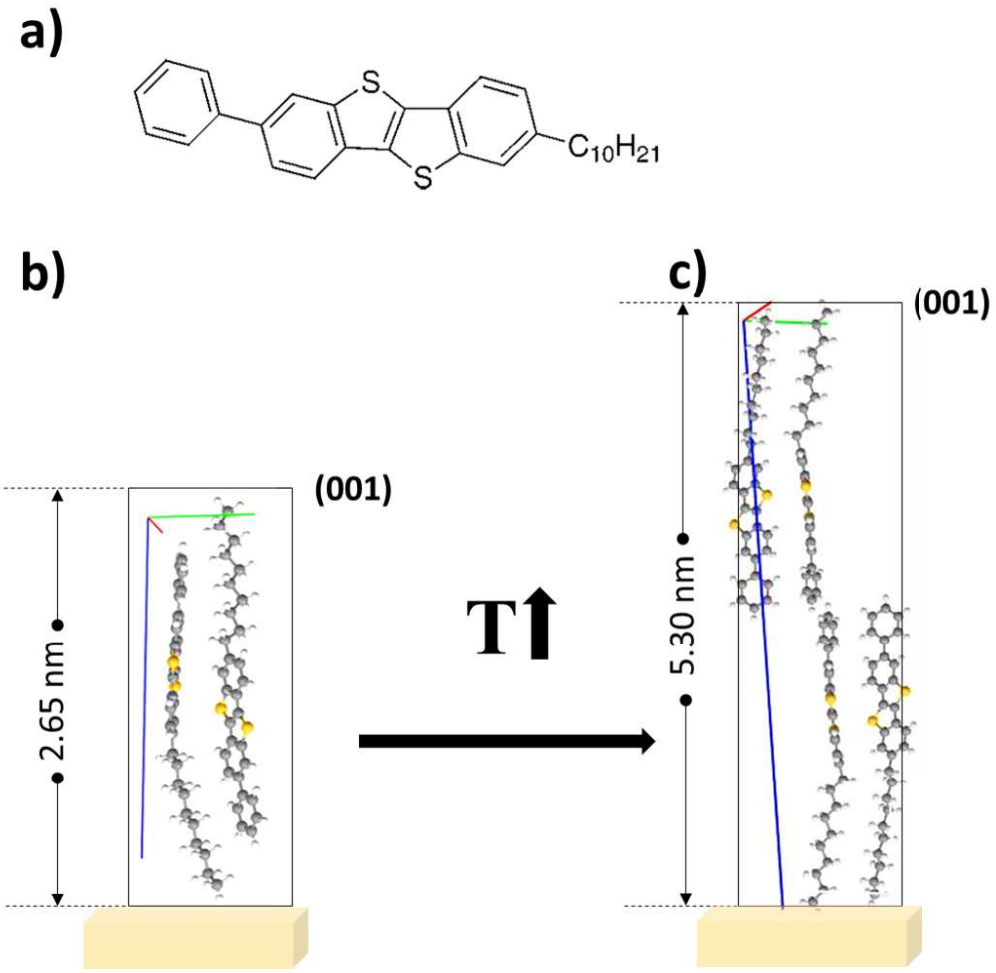


Figure 1. a) Molecular structure of Ph-BTBT-10. Crystalline polymorphs of Ph-BTBT-10: b) single layer and c) bilayer phases.

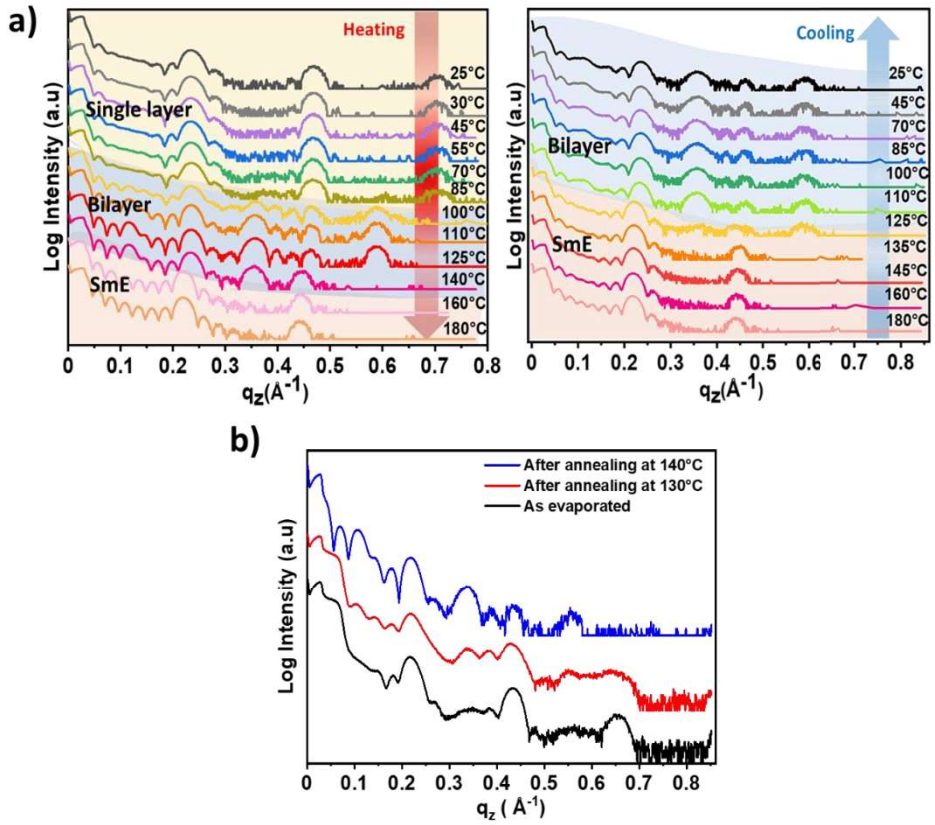


Figure 2. a) Temperature-dependent in-situ X-ray reflectivity (XRR) measurements performed on the evaporated Ph-BTBT-10 films during heating (left) and cooling (right) in the range between 25 °C and 180 °C. b) XRR Curves of the evaporated Ph-BTBT-10 films as-prepared and after annealing at 130°C and 140°C.

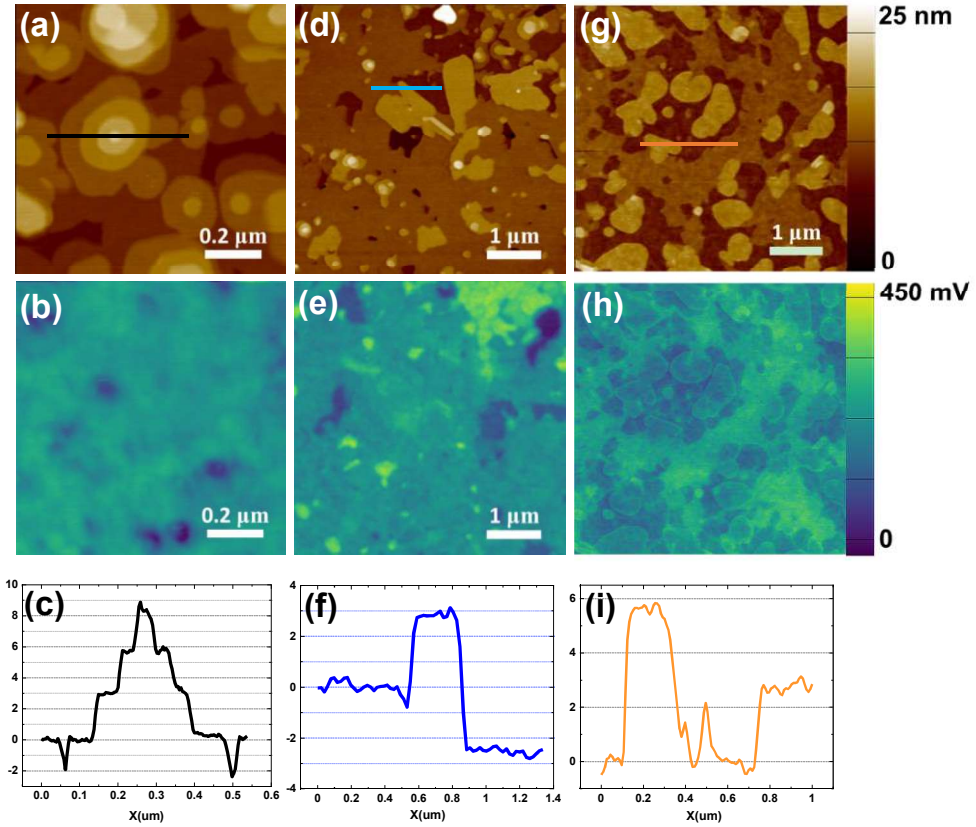


Figure 3. Images at the top are the topography of the film as deposited at room temperature (a), after post-annealing at 130°C for 10 minutes (d) and at 140°C for 20 minutes (g). Figures (b), (e) and (h) are the corresponding surface potential maps. The height profiles (along the lines indicated in the respective topographic images) are shown in (c), (f), and (i).

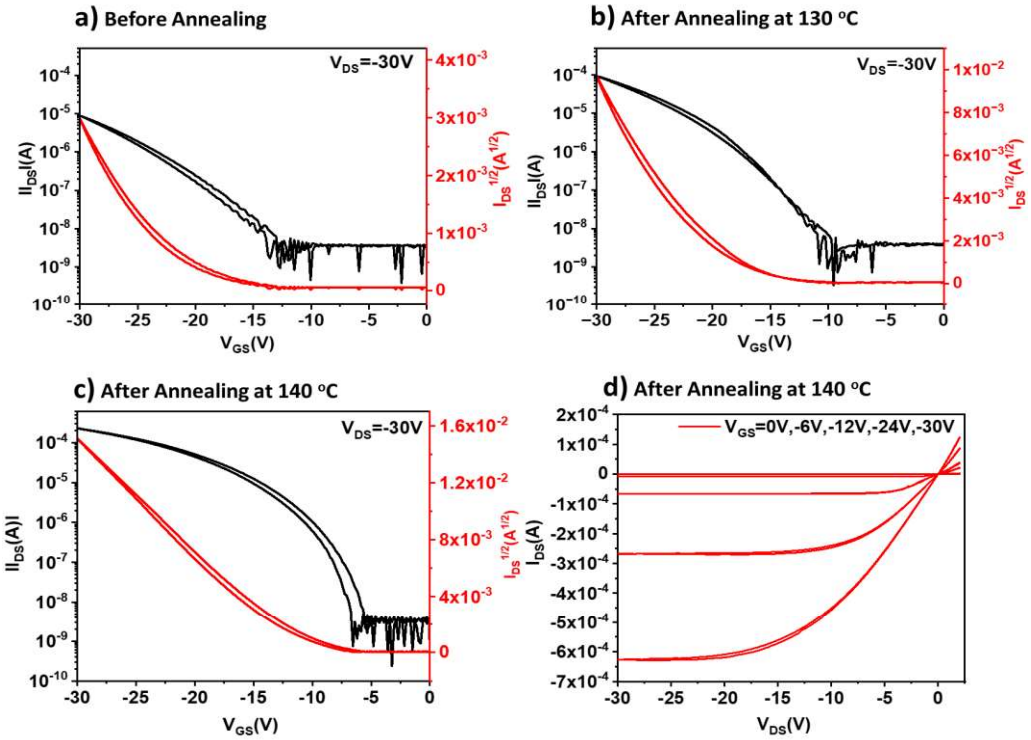


Figure 4. Transfer characteristics in the saturation regime (V_{DS}= -30V) of OFET based on Ph-BTBT-10 films a) as prepared, b) after thermal annealing at 130 ºC, and c) after thermal annealing at 140 ºC. d) Output characteristics of after thermal annealing at 140 ºC.

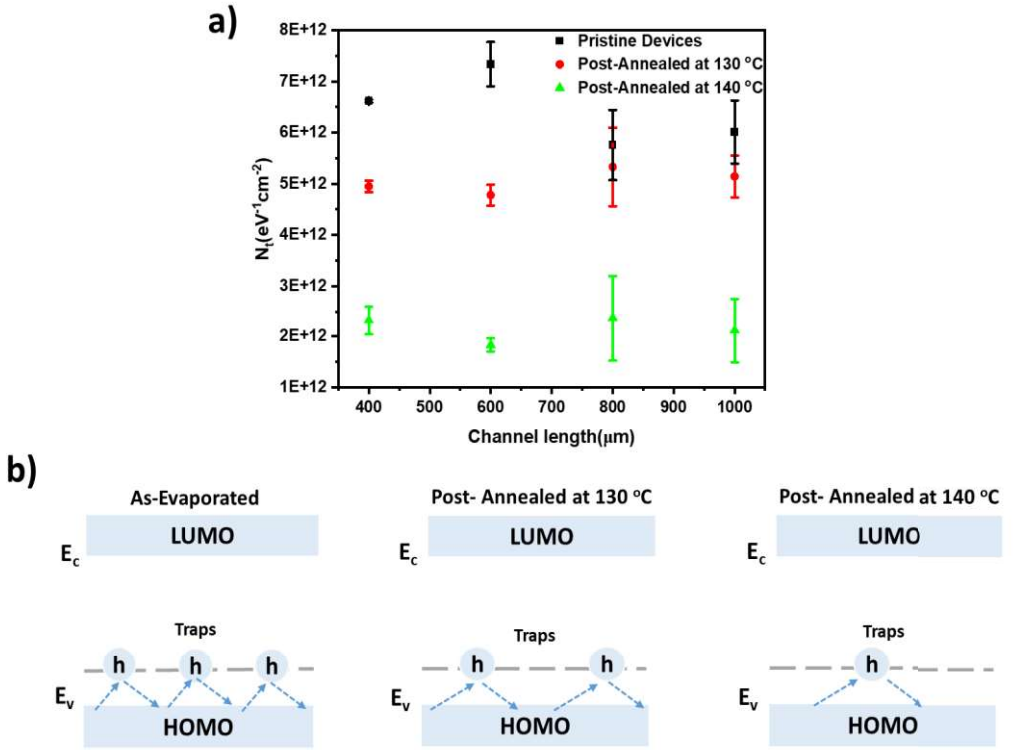
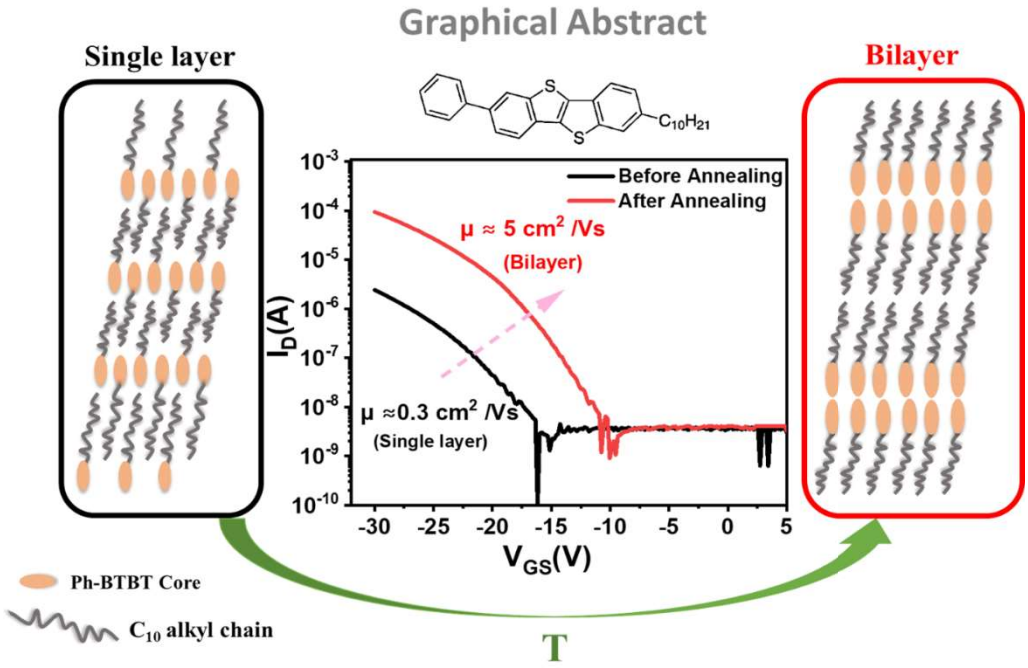


Figure 5. a) Density of interfacial hole traps estimated from the sub-threshold swing. b) Schematic diagrams of the trap distribution in the devices.

Graphical Abstract



References:

1 K. Haase, C. Teixeira da Rocha, C. Hauenstein, Y. Zheng, M. Hambsch and S. C. B. Mannsfeld, *Adv Electron Mater*, , DOI:10.1002/aelm.201800076.

2 K. Liu, B. Ouyang, X. Guo, Y. Guo and Y. Liu, *npj Flexible Electronics*, 2022, 6.

3 H. Chung, S. Chen, B. Patel, G. Garbay, Y. H. Geerts and Y. Diao, *Cryst Growth Des*, 2020, **20**, 1646–1654.

4 R. Pfattner, S. T. Bromley, C. Rovira and M. Mas-Torrent, *Adv Funct Mater*, 2016, **26**, 2256–2275.

5 L. Fijahi, J. Li, A. Tamayo, M. Volpi, G. Schweicher, Y. H. Geerts and M. Mas-Torrent, *Nanoscale*, 2022, **15**, 230–236.

6 Y. Yamaguchi, Y. Kojiguchi, S. Kawata, T. Mori, K. Okamoto, M. Tsutsui, T. Koganezawa, H. Katagiri and T. Yasuda, *Chemistry of Materials*, 2020, **32**, 5350–5360.

7 H. Minemawari, M. Tanaka, S. Tsuzuki, S. Inoue, T. Yamada, R. Kumai, Y. Shimoi and T. Hasegawa, *Chemistry of Materials*, 2017, **29**, 1245–1254.

8 H. Chung and Y. Diao, *J Mater Chem C Mater*, 2016, 4, 3915–3933.

9 Y. Diao, K. M. Lenn, W. Y. Lee, M. A. Blood-Forsythe, J. Xu, Y. Mao, Y. Kim, J. A. Reinspach, S. Park, A. Aspuru-Guzik, G. Xue, P. Clancy, Z. Bao and S. C. B. Mannsfeld, *J Am Chem Soc*, 2014, **136**, 17046–17057.

10 J. Chen, M. Shao, K. Xiao, A. J. Rondinone, Y. L. Loo, P. R. C. Kent, B. G. Sumpter, D. Li, J. K. Keum, P. J. Diemer, J. E. Anthony, O. D. Jurchescu and J. Huang, *Nanoscale*, 2014, **6**, 449–456.

11 T. Salzillo, A. Campos, A. Babuji, R. Santiago, S. T. Bromley, C. Ocal, E. Barrena, R. Jouclas, C. Ruzie, G. Schweicher, Y. H. Geerts and M. Mas-Torrent, *Adv Funct Mater*, , DOI:10.1002/adfm.202006115.

12 G. Giri, R. Li, D. M. Smilgies, E. Q. Li, Y. Diao, K. M. Lenn, M. Chiu, D. W. Lin, R. Allen, J. Reinspach, S. C. B. Mannsfeld, S. T. Thoroddsen, P. Clancy, Z. Bao and A. Amassian, *Nat Commun*, , DOI:10.1038/ncomms4573.

13 G. Giri, S. Park, M. Vosgueritchian, M. M. Shulaker and Z. Bao, *Advanced*

Materials, 2014, **26**, 487–493.

14 S. Galindo, A. Tamayo, F. Leonardi and M. Mas-Torrent, *Adv Funct Mater*, DOI:10.1002/adfm.201700526.

15 A. Tamayo, S. Riera-Galindo, A. O. F. Jones, R. Resel and M. Mas-Torrent, *Adv Mater Interfaces*, , DOI:10.1002/admi.201900950.

16 A. M. James, M. Gicevičius, S. Hofer, B. Schrode, O. Werzer, F. Devaux, Y. H. Geerts, H. Sirringhaus and R. Resel, *J Cryst Growth*, , DOI:10.1016/j.jcrysgro.2023.127539.

17 S. Izawa, K. Nakano, K. Suzuki, Y. Chen, T. Kikitsu, D. Hashizume, T. Koganezawa, T. Q. Nguyen and K. Tajima, *Sci Rep*, , DOI:10.1038/s41598-017-18881-y.

18 J. Li, A. Babuji, L. Fijahi, A. M. James, R. Resel, T. Salzillo, R. Pfattner, C. Ocal, E. Barrena and M. Mas-Torrent, *ACS Appl Mater Interfaces*, 2023, **15**, 5521–5528.

19 J. H. Bae, J. Park, C. M. Keum, W. H. Kim, M. H. Kim, S. O. Kim, S. K. Kwon and S. D. Lee, *Org Electron*, 2010, **11**, 784–788.

20 F. Dinelli, M. Murgia, F. Biscarini and D. M. De Leeuw, in *Synthetic Metals*, 2004, vol. 146, pp. 373–376.

21 K. C. Dickey, J. E. Anthony and Y. L. Loo, *Advanced Materials*, 2006, **18**, 1721–1726.

22 H. Iino, T. Usui and J. I. Hanna, *Nat Commun*, , DOI:10.1038/ncomms7828.

23 S. Hofer, J. Unterkofler, M. Kaltenegger, G. Schweicher, C. Ruzié, A. Tamayo, T. Salzillo, M. Mas-Torrent, A. Sanzone, L. Beverina, Y. H. Geerts and R. Resel, *Chemistry of Materials*, 2021, **33**, 1455–1461.

24 S. Hofer, W. Bodlos, J. Novák, A. Sanzone, L. Beverina and R. Resel, *Liq Cryst*, 2021, **48**, 1888–1896.

25 S. Kim, A. Kim, K. S. Jang, S. Yoo, J. W. Ka, J. Kim, M. H. Yi, J. C. Won, S. K. Hong and Y. H. Kim, *Synth Met*, 2016, **220**, 311–317.

26 T. Oka, N. Shioya, T. Shimoaka and T. Hasegawa, *Journal of Physical Chemistry C*, 2023, **127**, 7560–7564.

27 S. Yan, D. Cornil, J. Cornil, D. Beljonne, R. Palacios-Rivera, C. Ocal and E. Barrena, *Chemistry of Materials*, 2024, **36**, 585–595.

28 A. Tamayo, S. Hofer, T. Salzillo, C. Ruzié, G. Schweicher, R. Resel and M. Mas-Torrent, *J Mater Chem C Mater*, 2021, **9**, 7186–7193.

29 H. Wu, H. Iino and J. I. Hanna, *ACS Appl Mater Interfaces*, 2020, **12**, 29497–29504.

30 J. M. Cho and T. Mori, *Phys Rev Appl*, , DOI:10.1103/PhysRevApplied.5.064017.

31 K. He, W. Li, H. Tian, J. Zhang, D. Yan, Y. Geng and F. Wang, *ACS Appl Mater Interfaces*, 2017, **9**, 35427–35436.

32 S. Hofer, A. Hofer, J. Simbrunner, M. Ramsey, M. Sterrer, A. Sanzone, L. Beverina, Y. Geerts and R. Resel, *Journal of Physical Chemistry C*, 2021, **125**, 28039–28047.

33 H. F. Haneef, A. M. Zeidell and O. D. Jurchescu, *J Mater Chem C Mater*, 2020, 8, 759–787.

34 R. Resel, E. Tamas, B. Sonderegger, P. Hofbauer and J. Keckes, *J Appl Crystallogr*, 2003, **36**, 80–85.

35 Z. A. Lamport, H. F. Haneef, S. Anand, M. Waldrip and O. D. Jurchescu, *J Appl Phys*,DOI:10.1063/1.5042255.

Supporting Information

Phase transformations in evaporated Ph-BTBT-10 thin films and impact on the device performance

Lamiaa Fijahi,[1] Shunya Yan,[1] Ann Maria James,[2] Adrián Tamayo,[1] Jinghai Li,[1] Carmen Ocal,[1] Esther Barrena, [1,*] Roland Resel, [2,*] Marta Mas-Torrent[1,*]

[1] Institut de Ciència de Materials de Barcelona, ICMAB-CSIC, Campus UAB, 08193 Bellaterra, Spain. E-mail: e.barrena@csic.es; mmas@icmab.es
[2] Institute of Solid State Physics, Graz University of Technology, Petersgasse 16, Graz 8010, Austria. E-mail: roland.resel@tugraz.at

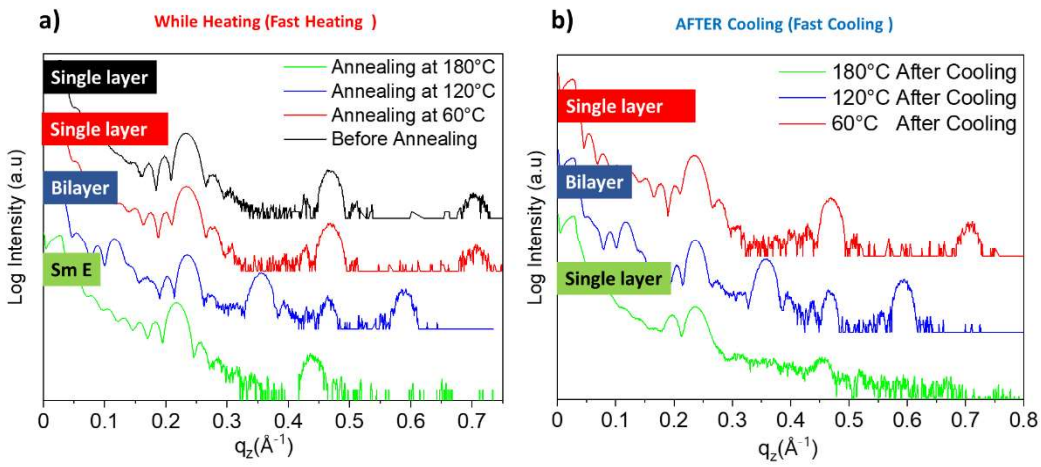


Figure S1. XRR curves of the evaporated Ph-BTBT-C10 films: a) when annealed at 60 ° C, 120 ° C and 180 ° C and b) after fast cooling.

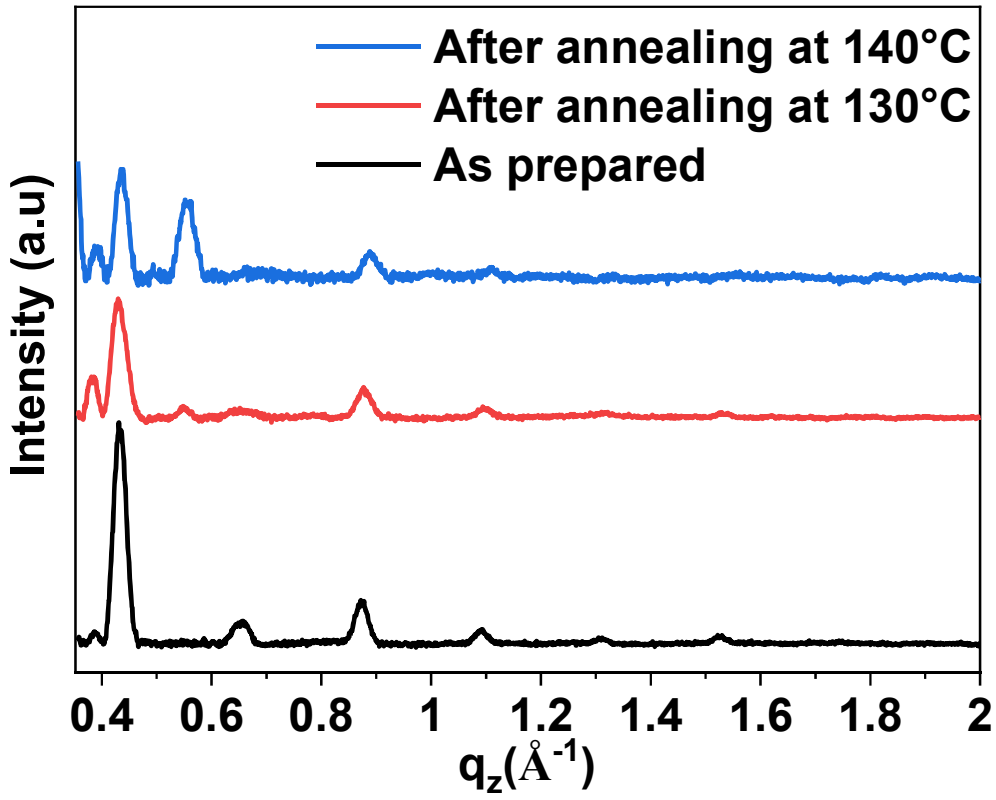


Figure S2. XRD diffractograms of the evaporated Ph-BTBT-C10 films and the same films after annealing at 130 °C for 10 minutes and 140 °C for 20 minutes.

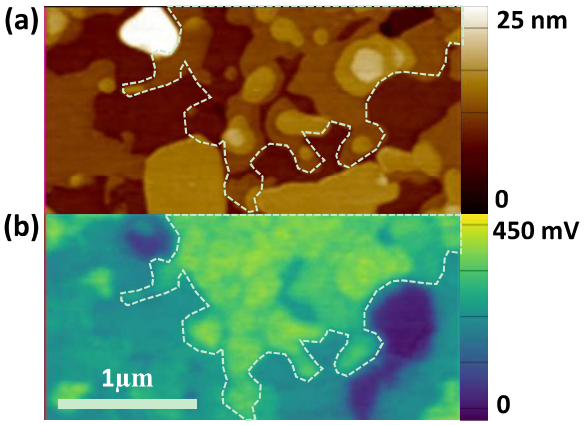


Figure S3. Topography (a) and surface potential maps (b) of the Ph-BTBT-C10 film annealed at 130°C for 10 minutes (magnifications of Figure 3d and 3e in the manuscript).

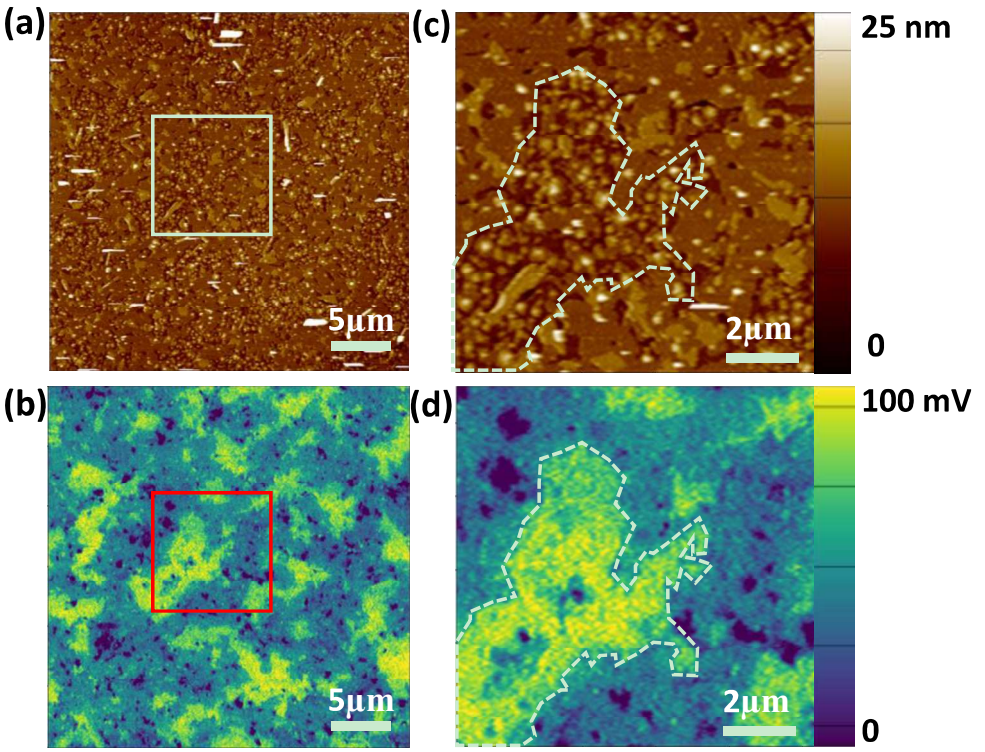


Figure S4. Topography and surface potential maps of the Ph-BTBT-C10 film annealed at 130°C for ten minutes: 30 µm image (a and b) and magnified area of 5 µm (c and d).

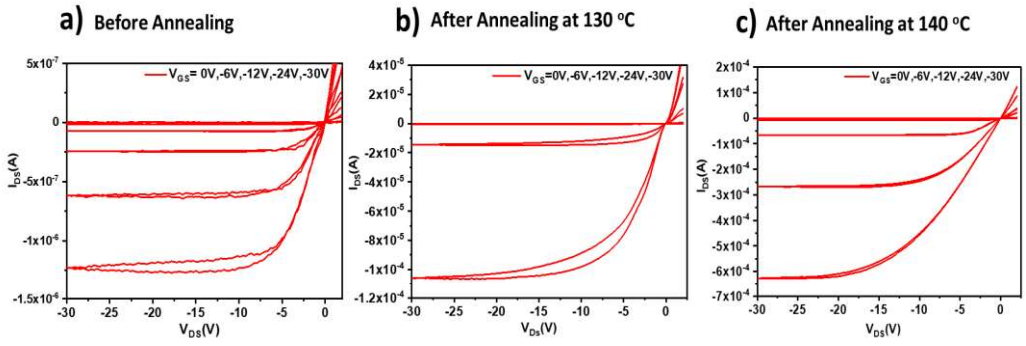


Figure S5. Output electrical characteristics of the OFETs with L=1000 µm. a) before and after post-annealing at b) 130 °C and c) 140 °C.

Table S1: Electrical characteristics extracted for devices as coated and after annealing at 130 °C and 140 °C.

	As coated	After Annealing at 130 °C	After Annealing at 140 °C
μ_{Sat} ($cm^2V^{-1}s^{-1}$)	0.2±0.15	1.5±0.4	4.1±0.3
Sat. V_{th} (V)	-21±2	-17±2	-10.0±0.9
SS ($V\ Dec^{-1}$)	3.6±0.4	3.0±0.2	1.3±0.3
N_t ($10^{12}eV^{-1}cm^{-2}$)	6.3±0.8	5.1±0.4	2.2±0.7

4.3 Results on solution-processed Ph-BTBT-10 films

- **Effect of deposition temperature on the thin-film properties**

Bottom-gate bottom-contact OFET devices were prepared using as active layer films of Ph-BTBT-10 and a blend of Ph-BTBT-10 with polystyrene (Ph-BTBT-10:PS). These films were deposited using the bar-assisted meniscus shearing (BAMS) technique, aiming to produce high-performance OFET devices through a high-throughput process.

These devices were fabricated onto Si/SiO_2 (200 nm SiO_2) substrates with interdigitated Cr/Au electrodes, patterned by photolithography and deposited by thermal evaporation. The channel's width and length were 150 μm and 100 μm, respectively (W/L = 100). Before the thin-film deposition, substrates were cleaned by acetone and isopropanol. The gold surface of the source and drain electrodes was chemically modified with a self-assembled monolayer of pentafluorobenzenethiol (PFBT, from Sigma-Aldrich).The substrates were first cleaned using ultraviolet ozone for 25 min and then immersed into a $15 \cdot 10^{-3}$ M solution of PFBT in isopropanol for 15 min. Finally, the substrates were rinsed with pure isopropanol, and then dried under a nitrogen flux. OSC thin films were deposited in ambient conditions using the BAMS technique. Solutions of Ph-BTBT-10 and Ph-BTBT-10:PS were prepared in chlorobenzene (PhCl) with a final concentration of 2.0 % w/w. In the case of blends, 280 kDa PS was chosen and the solutions of Ph-BTBT-10:PS had a weight ratio of 4:1. Before solution deposition, the solutions were heated at the substrate temperature used for the coating process. To study the influence of the coating temperature the films were deposited at 10 $mm \cdot s^{-1}$ at a temperature ranging from 85 °C to 120 °C.

In all the cases, we observed the presence of highly ordered crystalline structures with large (up to 20 μm diameter) domains by polarized optical microscopy (POM) under these deposition conditions (**Figure 4.3**). The films were also characterized by atomic force microscopy (AFM) to determine the nanomorphology of the thin film surface (**Figure 4.4**).

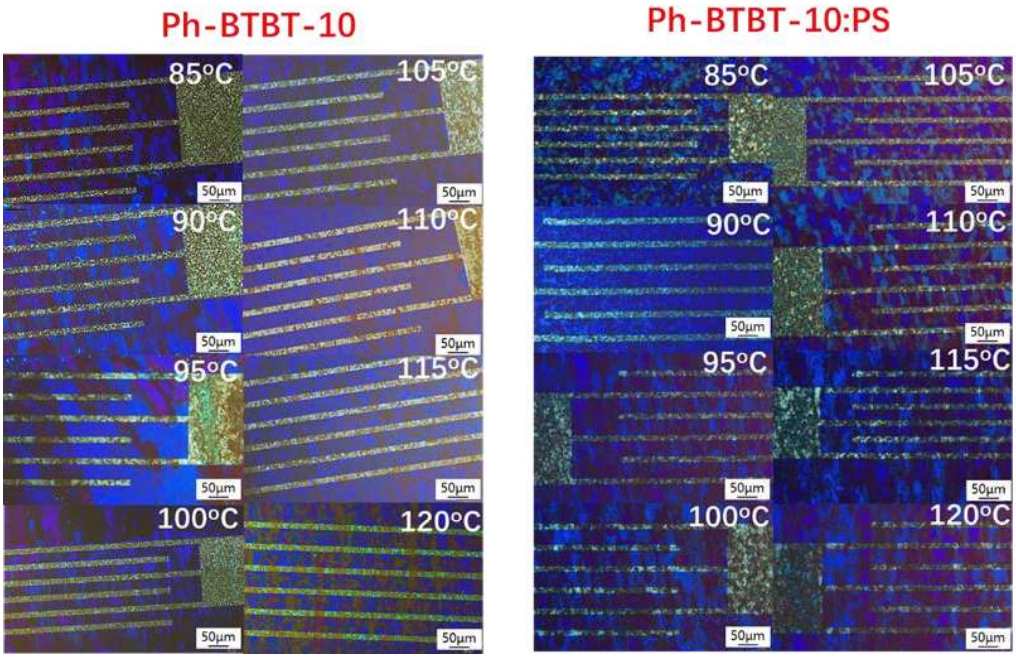


Figure 4.3. Representative polarized optical microscope images of Ph-BTBT-10 and Ph-BTBT-10:PS thin films deposited by BAMS at different deposition temperatures (from 85 °C to 120 °C). The scale bar corresponds to 50 μm.

By AFM it was determined that all the films showed a thickness of around 20 nm and a low roughness with a root-mean-square (RMS) in the range of 1-2 nm, as summarised in **Table 4.1**. Noticeably, the films based on blends seem to be more homogenous showing completed molecular layers. The height distribution function reveals steps with the most common average height of around 5.1 nm for all the films deposited at 85 °C and 105 °C, while for the films deposited at 120 °C the most abundant steps exhibit a height of around 2.65 nm (see in **Table 4.1** the step heights of three different profiles marked in **Figure 4.4**).

The characteristic heights observed in the AFM studies can be compared with the unit cell dimensions of the known crystallographic structures. The step of 5.1 nm is close to the interplanar distance of the (001) plane of the bilayer structure (d_{001}=5.3 nm), while the steps of 2.65 nm seem to correspond to the interplanar distance of a monolayer structure. Therefore, based on the AFM images, we can anticipate that in all the cases the molecules align with their long molecular axes perpendicular to the substrate surface. Additionally, the films prepared at the highest temperature (120 °C) appear to be more enriched with the monolayer phase. In contrast, films prepared at lower temperatures exhibit mainly steps corresponding to molecular bilayers, although certain coexistence of monolayer steps is also present.

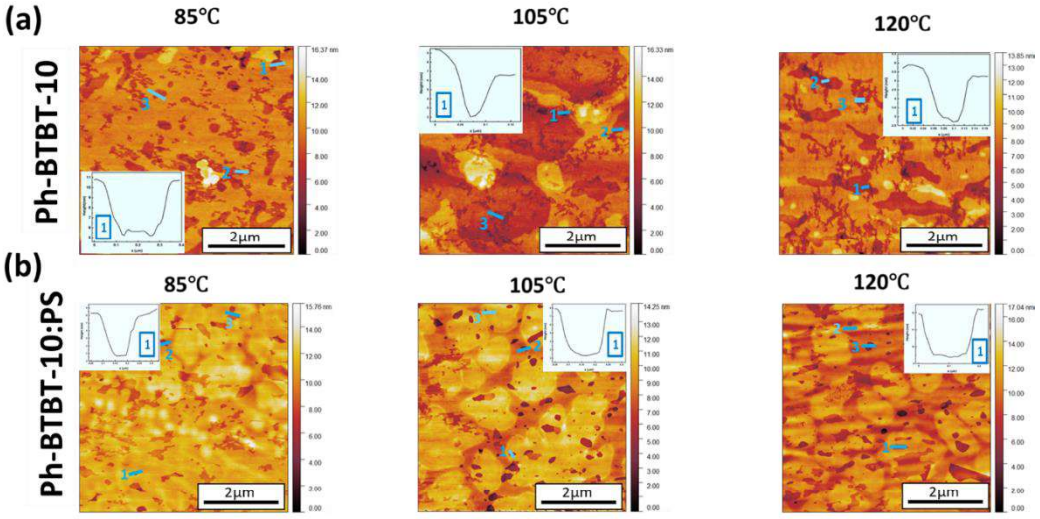


Figure 4.4. AFM topography images of (a) Ph-BTBT-10 and (b) Ph-BTBT-10:PS blend thin films deposited by BAMS at different deposition temperatures (from 85ºC to 120ºC) and at l0 mm·s^{-1} coating speed. Scale bar: 2 µm. Inset: high profiles extracted along the blue line number 1 of the images

Table 4.1: Surface roughness and height steps extracted from the Ph-BTBT-10 and Ph-BTBT-10:PS AFM images from Figure 4.4. Three height steps are included, which correspond to the three lines marked in Figure 4.4 (1, 2 and 3, from top to bottom).

	Ph-BTBT-10			Ph-BTBT-10:PS		
	85°C	105°C	120°C	85°C	105°C	120°C
Roughness (RMS) nm	1.4±0.3	1.9±0.5	1.4±0.2	1.3±0.3	1.7±0.3	1.9±0.3
Height Step (nm)	5.1±0.2	5.1±0.7	2.6±0.1	5.2±0.6	5.1±0.3	2.9±0.3
	5.0±0.4	4.9±0.5	2.7±0.1	5.1±0.6	5.2±0.1	2.6±0.1
	2.6±0.2	2.7±0.2	2.6±0.3	2.7±0.4	5.2±0.4	5.2± 0.1

XRR investigations were performed in films based on Ph-BTBT-10 and Ph-BTBT-10:PS prepared at different coating temperatures. The films based on Ph-BTBT-10 deposited at low temperatures (85-105 °C) showed distinct diffraction peaks at 2θ values of 4.9° and 8.3°, characteristic of the bulk phase (**Figure 4.5**). Noticeably, such peaks are broad, which can be indicative of disorder, as previously reported.[15] At a temperature of 110 °C and above, a decrease in the peak intensity is significantly observed, which indicates that the single-layer structure becomes more dominant in these films. A similar phenomenon is found in the blend films, although at high coating temperatures, the presence of still traces of bulk phase seems more evident. We believe that coating the films in the range 85-105 °C leads to the formation of films enriched with the bulk phase. However, above 110 °C, the crystallization is very fast due to the rapid solvent evaporation, and, therefore, the kinetic single molecule phase is favored.

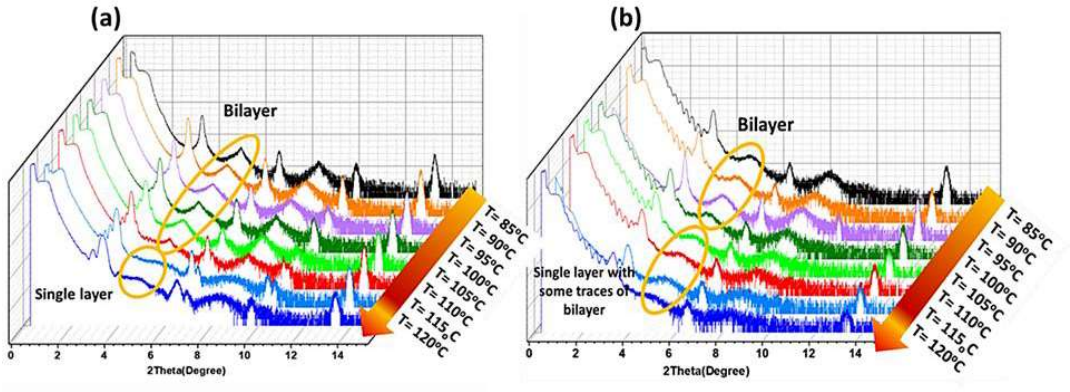


Figure 4.5. XRR curves of the Ph-BTBT-10 thin films prepared by BAMS at different deposition temperatures without (a) and with (b) PS binding polymer.

All the films were electrically characterized as active layers in OFETs under ambient conditions. **Figures 4.6** and **4.7** show the transfer characteristics (in the saturation and linear regime) and output characteristics for representative devices based on thin films of Ph-BTBT-10 and Ph-BTBT-10:PS, respectively. All the devices exhibit p-type OFET characteristics with low hysteresis, especially the blended films. In general, the devices based on films of Ph-BTBT-10:PS reveal threshold voltages (V_{th}) closer to zero compared to the pristine Ph-BTBT-10 films. It is worth noticing that the use of blends significantly enhances the device mobility of the films around one order of magnitude (**Figure 4.8**). It is known that the viscosity of the ink solutions promotes the formation of more homogenous films. At low coating temperature (i.e., 85°C), the mobility is found to be 0.04±0.02 and 0.50±0.13 $cm^2 \cdot V^{-1} \cdot s^{-1}$ for Ph-BTBT-10 and Ph-BTBT-10:PS films, respectively. On the other hand, at the highest deposition temperature (i.e., 120 °C), the highest mobility value was found to be 0.2±0.1 and 1.30±0.2 $cm^2 \cdot V^{-1} \cdot s^{-1}$ for Ph-BTBT-10 and Ph-BTBT-10:PS films, respectively. In the case of the Ph-BTBT-10 films, a gradual increase in mobility was observed with increasing the deposition temperature, which starts to be more pronounced

at 105 ^{o}C and above. In the case of the blend films, an approximately constant mobility is found at low deposition temperatures. However, a sudden increase in mobility can be observed at 100 ^{o}C, after which mobility remains constant. Thus, in both films, the mobility improves upon the formation of the monolayer structure, which was not expected considering that the bilayer structure is more favorable for charge transport. [14] This might suggest that mobility in our films is more closely related to the thin film characteristics than to the crystal structure. It should also be noted that the fact that the bilayer structure exhibits lower mobility in the here-prepared films could be attributed to the disorder present in the thin films, as indicated by the broad XRR peaks observed in the films fabricated at low temperatures.

These results highlight the critical influence of deposition temperature on the crystallization and molecular organization of Ph-BTBT-10 films and their blends. Such insights are pivotal for optimizing these materials for applications in high-performance organic electronic devices, where controlled molecular packing is key to ensure device reproducibility and significantly enhance device performance

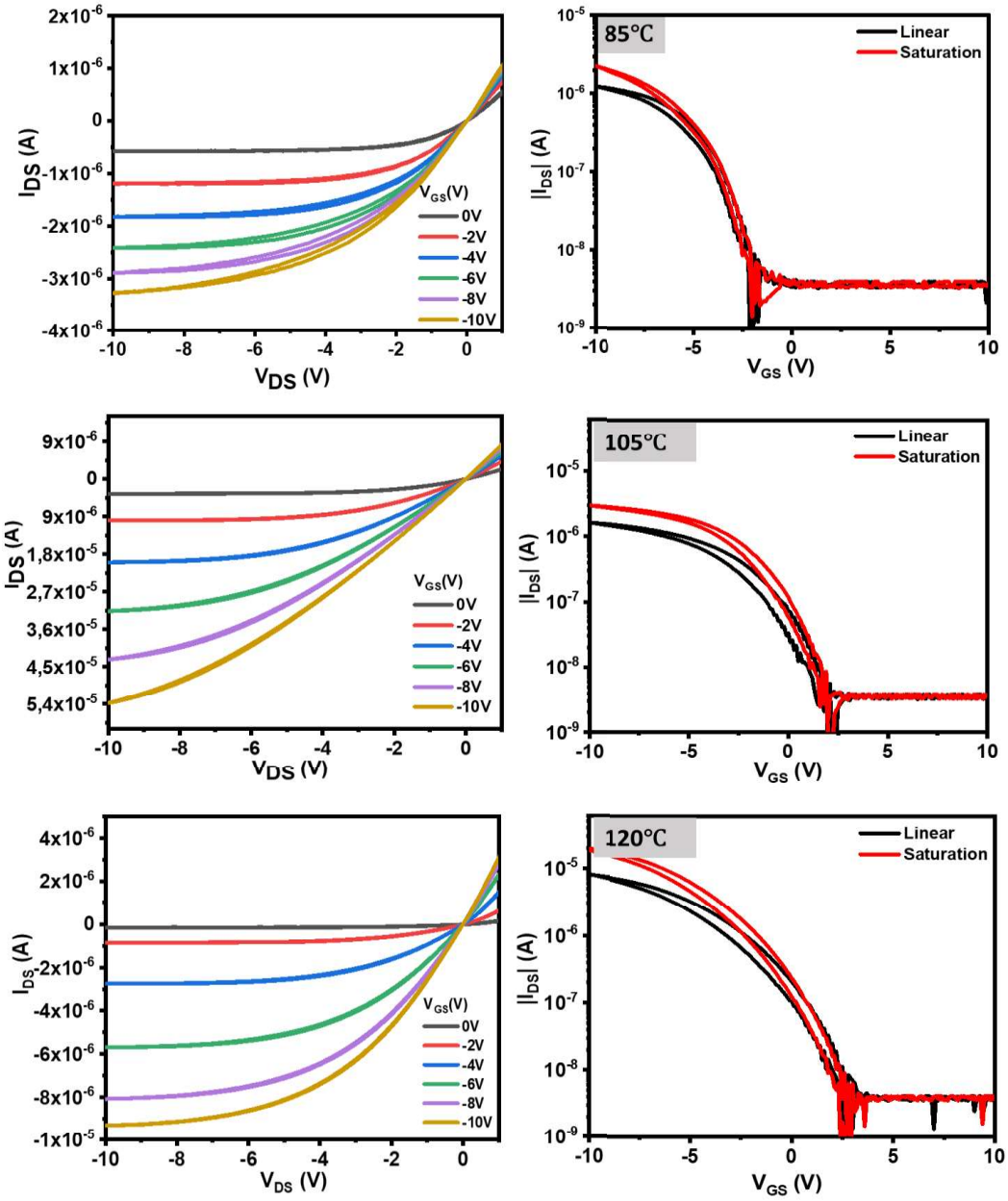


Figure 4.6. Electrical performance of the OFET devices. Representative output and transfer characteristics in linear (V_{DS} = -2 V) and saturation (V_{DS} = -10 V) regime of representative Ph-BTBT-10 based OFETs prepared at different deposition temperatures.

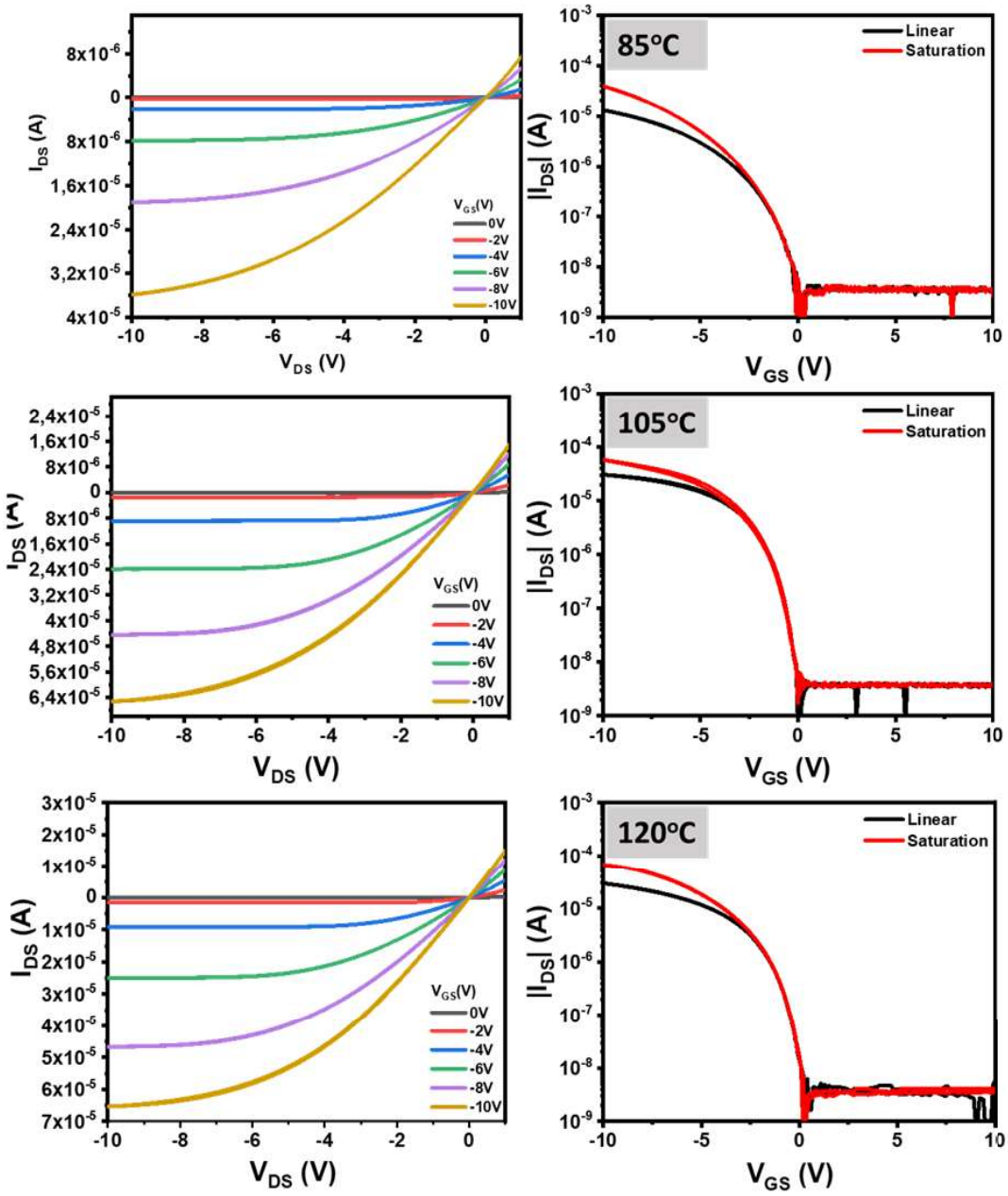


Figure 4.7. Electrical performance of the OFET devices. Output and transfer characteristics in linear (V_{DS} = -2 V) and saturation regime (V_{DS} = -10 V) of representative Ph-BTBT-10:PS based OFETs prepared at different deposition temperatures.

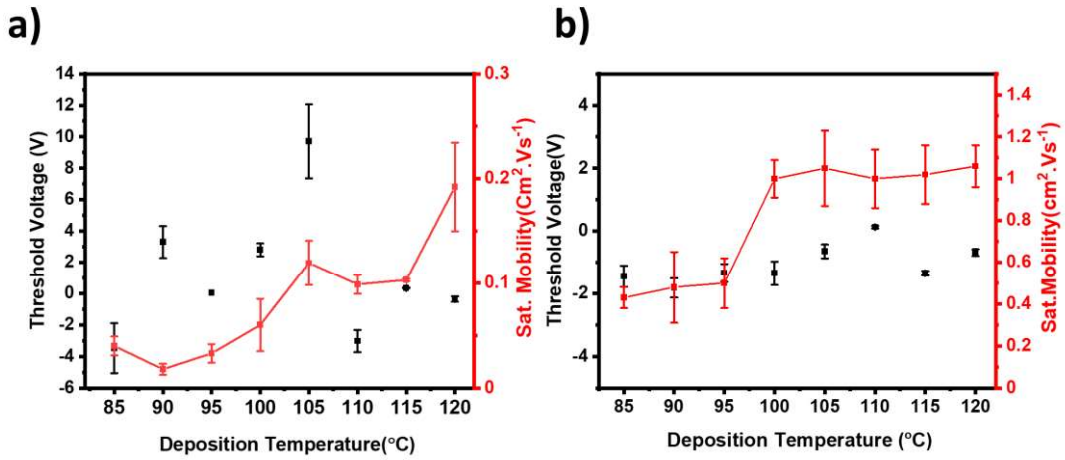


Figure 4.8. Variation of mobility and threshold voltage of a) Ph-BTBT-10 thin films and b) Ph-BTBT-10:PS thin films as a function of the deposition temperature (from 85 °C to 120 °C).

- **Effect of thermal post-annealing on the thin film structure and charge carrier mobility**

Following, we explored the influence of thermal post-annealing on thin films. Thin films of Ph-BTBT-10 and Ph-BTBT-10:PS were deposited at 10 mm·s^{-1} and at a fixed temperature of 120 °C, as previously explained. Following, the films were post-annealed at 120°C for 20 minutes at the same coating stage. That is, just after the thin film formation, the samples were left on the coating stage during the annealing process. This approach allowed us to investigate how thermal annealing impacts both the structural characteristics of the thin films and their resulting electrical performance in the OFET devices. The POM images of the annealed Ph-BTBT-10 films show an increase in the crystal size compared to the non-annealed films (**Figure 4.9**). Such an effect is, however, not found in the blend films.

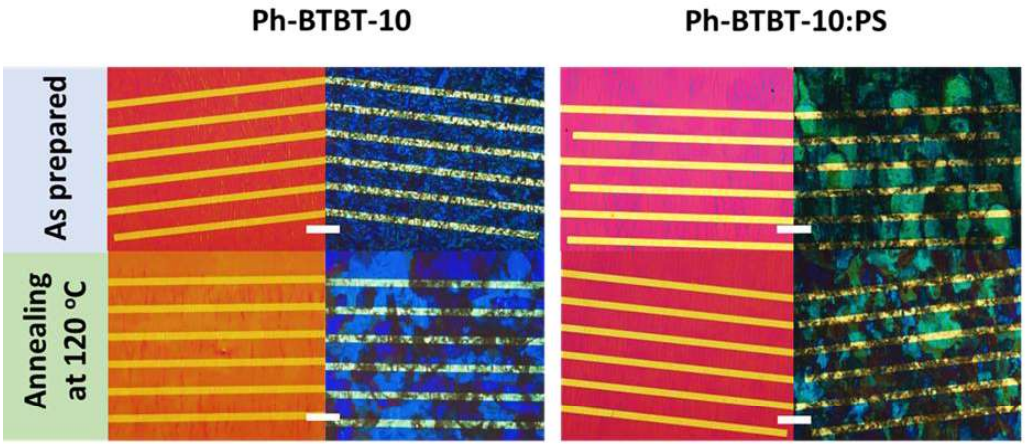


Figure 4.9. Non-polarized (left) and polarized (right) optical microscopy images of the non-annealed and annealed Ph-BTBT-10 and Ph-BTBT-10:PS thin films coated by BAMS at a speed of 10 mm·s^{-1} and at 120 °C. Scale bar: 100 μm.

To understand the possible changes in the crystal structure caused by the thermal annealing procedure, the films were investigated by XRR (**Figure 4.10**). As previously mentioned, all the films deposited at 120°C are mainly formed by monolayer phase. However, when these films are annealed distinct diffraction peaks are observed at 2θ values of 4.9° and 8.3°, corresponding to 00L peak series characteristic of the bilayer phase. Interestingly, in these films, the peak broadening, previously found in the films deposited at 85 °C which corresponded also to the bulk bilayer polymorph, is much less pronounced. This suggests that the post-annealing treatment promotes the transition from the monolayer phase to the bilayer, leading to films with a more ordered molecular arrangement compared to the bulk films obtained using low coating temperatures.

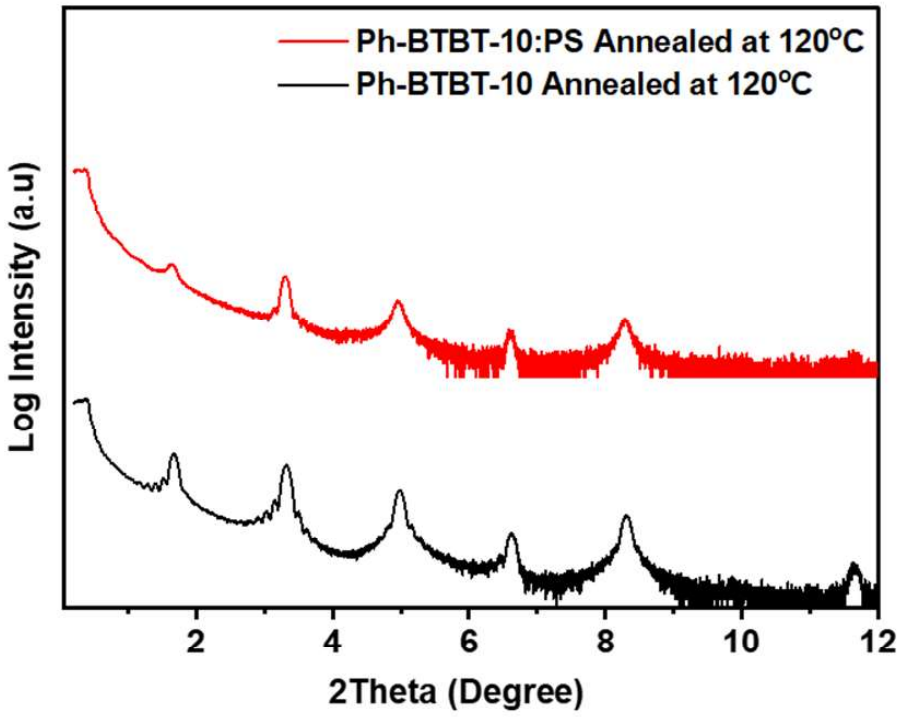


Figure 4.10. XRR curves of the Ph-BTBT-10 and Ph-BTBT-10:PS films annealed at 120 °C for 20 min.

The effect of thermal annealing on the electrical performance of Ph-BTBT-10 and Ph-BTBT-10:PS OFETs was evaluated under ambient conditions. Bottom-contact OFETs were fabricated on Si/SiOx (200 nm thick) substrates as previously described. The transfer characteristics curves of the non-annealed and annealed films are shown in **Figure 4.11**, while in **Table 4.2** the device figures of merit (i.e., mobility and threshold voltage) are summarized. The average OFET mobility calculated for the Ph-BTBT-10 thin film devices showed a clear improvement with thermal treatment, going from 0.26±0.06 $cm^2 \cdot V^{-1} \cdot s^{-1}$ for the non-annealed films to 0.40±0.10 $cm^2 \cdot V^{-1} \cdot s^{-1}$ for the annealed ones. For the blend Ph-BTBT-10:PS films, the mobility increased after annealing from 1.23±0.05 $cm^2 \cdot V^{-1} \cdot s^{-1}$ to 1.83±0.47 $cm^2 \cdot V^{-1} \cdot s^{-1}$.

It was concluded that the observed significant improvement in the OFET mobility in the post-annealed films is related to the realization of the bilayer phase with high structural order. Additionally, it has been demonstrated again that PS significantly helps in enhancing the device performance.

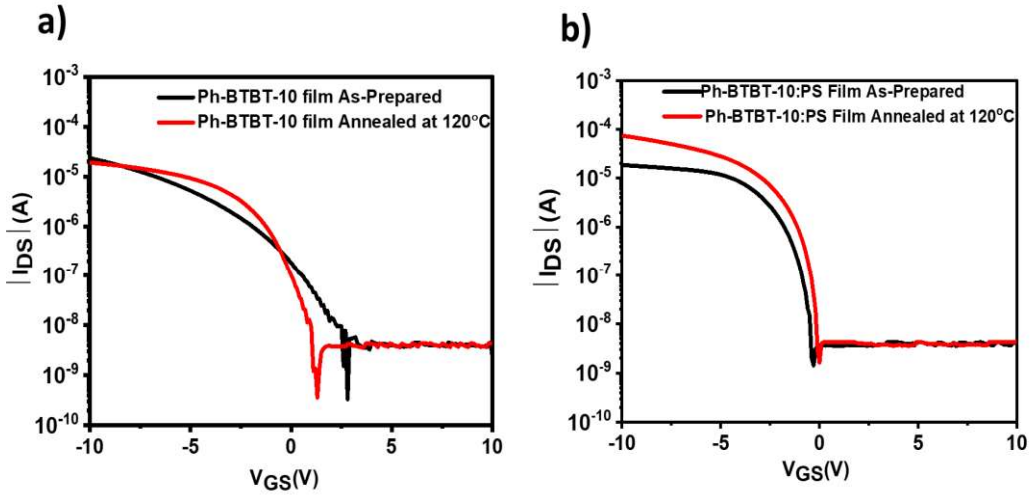


Figure 4.11. Transfer characteristics in the saturation regime (V_{DS} = -10 V) of OFETs based on (a) Ph-BTBT-10 films and (b) Ph-BTBT-10:PS films coated at 120 ºC, as prepared and after the application of a thermal annealing step (120 ºC for 20 min).

Table 4.2: Electrical characteristics extracted for devices as coated and after annealing at 120 ºC for 20 min.

	Ph-BTBT-10 coated at 120 ºC	Ph-BTBT-10 Coated and Annealed at 120ºC	Ph-BTBT-10:PS Coated at 120 ºC	Ph-BTBT-10:PS Coated at 120 ºC
μ_{Sat} ($cm^2V^{-1}s^{-1}$)	0.26±0.06	0.40±0.10	1.23±0.05	1.83±0.47
Sat. V_{th} (V)	-1.64±0.55	1.53±0.47	-0.6±0.07	-0.23±0.05

4.4 Conclusions

In this chapter, the p-type asymmetric organic semiconductor Ph-BTBT-10 was extensively studied to understand its structural properties and performance in OFET devices. Both solution and evaporation techniques were employed, with a detailed investigation into the structural thin film properties:

i. Evaporated thin films:

X-ray reflectivity (XRR) data performed at various temperatures identified single layer, bilayer, and SmE phases. As-deposited single-layer films were annealed to convert them to the bulk bilayer form. Combined characterization by XRR and KPFM showed that only the films annealed at 140°C fully transitioned to the bilayer structure, while those annealed at 130°C still partially retained the single layer phase. OFET devices based on these annealed films exhibited enhanced mobility and reduced charge traps, with the best mobility achieved in the fully bulk phase transformed films.

ii. Solution-Processed thin films:

Bottom-gate bottom-contact OFET devices were fabricated using thin films of Ph-BTBT-10 and a blend of Ph-BTBT-10:PS. These films were deposited via BAMS technique at a rate of 10 $mm \cdot s^{-1}$ and coating temperatures ranging from 85°C to 120°C to investigate the impact of deposition temperature on their crystal structure and electrical performance. XRR analysis confirmed that the films coated at lower temperature are mainly composed of disordered bilayer phase, but above 110 °C the kinetic single layer polymorph is dominant. The films coated at higher temperature exhibited higher mobility, which was hypothetically attributed to the high molecular disorder present in the bulk phase. However, when the films coated at 120 °C belonging to the single layer structure were

thermally post-annealed, the films were converted to the bilayer phase achieving high molecular order. Such devices exhibited the highest OFET performance, with a mobility of 0.4 $cm^2 \cdot V^{-1} \cdot s^{-1}$ for Ph-BTBT-10 thin films and close to 2 $cm^2 \cdot V^{-1} \cdot s^{-1}$ for the blend films.

Overall, this work demonstrates that Ph-BTBT-10 films are prone to polymorphism and disorder due to its asymmetry. It has been shown that the bulk phase favors charge transport, but in order to realise and optimize the device performance, it is the key to achieve a high percentage of bulk phase and also to avoid molecular disorder within the film. The modification of the deposition temperature and the application of post-thermal treatments are efficient routes to control the thin film's structure and to realise high performing devices. Further, in solution-processed films, PS has shown to be pivotal to significantly enhance the OFET performance

4.5 References

[1] E. Ferrari et al., “Structural Order and Thermal Behavior of Ph-BTBT-10 Monolayer Phases,” Journal of Physical Chemistry C, vol. 128, no. 10, pp. 4258–4264, Mar. 2024, doi: 10.1021/acs.jpcc.3c07365.

[2] N. Shioya et al., “Conformational Change of Alkyl Chains at Phase Transitions in Thin Films of an Asymmetric Benzothienothiophene Derivative,” Journal of Physical Chemistry Letters, vol. 13, no. 51, pp. 11918–11924, Dec. 2022, doi: 10.1021/acs.jpclett.2c03399.

[3] H. Wu, H. Iino, and J. I. Hanna, “Scalable Ultrahigh-Speed Fabrication of Uniform Polycrystalline Thin Films for Organic Transistors,” ACS Appl Mater Interfaces, vol. 12, no. 26, pp. 29497–29504, Jul. 2020, doi: 10.1021/acsami.0c05105.

[4] J. M. Cho and T. Mori, “Low-Temperature Band Transport and Impact of Contact Resistance in Organic Field-Effect Transistors Based on Single-Crystal Films of Ph-BTBT-C10,” Phys Rev Appl, vol. 5, no. 6, pp. 64017, Jun. 2016, doi: 10.1103/PhysRevApplied.5.064017.

[5] H. Iino and J. I. Hanna, “Liquid crystalline organic semiconductors for organic transistor applications,” Nature Publishing Group, vol. 49, no., pp.23-33, Jan. 2017, doi: 10.1038/pj.2016.101.

[6] H. Iino, T. Usui, and J. I. Hanna, “Liquid crystals for organic thin-film transistors,” Nat Commun, vol. 6, no.6828, Apr. 2015, doi: 10.1038/ncomms7828.

[7] W. R. Bodlos et al., “Controlled recrystallization from the melt of the organic n-type small molecule semiconductor 2-decyl-7-phenyl-[1]benzothieno[3,2-b][1]benzothiophene S,S,S′,S′-tetraoxide,” J Cryst Growth, vol. 572, no. 51, pp.126255, Oct. 2021, doi: 10.1016/j.jcrysgro.2021.126255.

[8] W. R. Bodlos et al., “Cold Crystallization of the Organic n-Type Small Molecule Semiconductor 2-Decyl-7-phenyl-[1]benzothieno[3,2- b][1]benzothiophene S, S, S′, S′-Tetraoxide,” Cryst Growth Des, vol. 21, no. 1, pp. 325–332, Jan. 2021, doi: 10.1021/acs.cgd.0c01157.

[9] S. Hofer et al., “Phase Transition toward a Thermodynamically Less Stable Phase: Cross-Nucleation due to Thin Film Growth of a Benzothieno-benzothiophene Derivative,” Journal of Physical Chemistry C, vol. 125, no. 51, pp. 28039–28047, Dec. 2021, doi: 10.1021/acs.jpcc.1c06610.

[10] H. Ebata et al., “Highly soluble [1]benzothieno[3,2-b]benzothiophene (BTBT) derivatives for high-performance, solution-processed organic field-effect

transistors," J Am Chem Soc, vol. 129, no. 51, pp. 15732–15733, Dec. 2007, doi: 10.1021/ja074841i.

[11] S. Hofer et al., "Molecular Disorder in Crystalline Thin Films of an Asymmetric BTBT Derivative," Chemistry of Materials, vol. 33, no. 4, pp. 1455–1461, Feb. 2021, doi: 10.1021/acs.chemmater.0c04725.

[12] T. Oka, N. Shioya, T. Shimoaka, and T. Hasegawa, "Structural Rearrangement of Organic Semiconductor Molecules with an Asymmetric Shape in Thin Films," Journal of Physical Chemistry C, vol. 127, no. 15, pp. 7560–7564, Apr. 2023, doi: 10.1021/acs.jpcc.3c01003.

[13] E. Ferrari et al., "Interlayer Sliding Phonon Drives Phase Transition in the Ph-BTBT-10 Organic Semiconductor," Chemistry of Materials, vol. 35, no. 15, pp. 5777–5783, Aug. 2023, doi: 10.1021/acs.chemmater.3c00209.

[14] H. Wu, H. Iino, and J. I. Hanna, "Thermally induced bilayered crystals in a solution-processed polycrystalline thin film of phenylterthiophene-based monoalkyl smectic liquid crystals and their effect on FET mobility," RSC Adv, vol. 7, no. 89, pp. 56586–56593, 2017, doi: 10.1039/c7ra11727b.

[15] A. Moser et al., "A disordered layered phase in thin films of sexithiophene," Chem Phys Lett, vol. 574, pp. 51–55, Jun. 2013, doi: 10.1016/j.cplett.2013.04.053.

Chapter 5: Conclusions

We have successfully exploited the bar-assisted meniscus shearing (BAMS) technique to deposit p-type and n-type small molecule organic semiconductors (OSCs) and blends of these OSCs with polystyrene (PS). This approach has resulted in the formation of high-quality films that exhibit excellent performance as active layers in organic field-effect transistors (OFETs). Our research focused on understanding the impact of various fabrication parameters on the thin film characteristics as well as on the OFET performance. The key conclusions from this work are:

1. Charge-transfer complexes (CTC) have been typically studied as single crystals or as evaporated thin films. Here, by optimizing the processing parameters and the ink formulation, we showed that CTC can be processed as thin films using a low-cost solution-based technique. We have studied two novel CTC crystals using the OSC C_8O-BTBT-OC_8: (C_8O-BTBT-OC_8) (F_2TCNQ) and (C_8O-BTBT-OC_8) (F_4TCNQ). Both complexes crystallise in a 1:1 stoichiometry with alternating stacks of C_8O-BTBT-OC_8 and either F_2TCNQ or F_4TCNQ. Spectroscopic analysis showed ionicity values of 0.16 for (C_8O-BTBT-OC_8) (F_2TCNQ) and 0.29 for (C_8O-BTBT-OC_8) (F_4TCNQ), indicating higher charge transfer with F_4TCNQ. Homogeneous and polycrystalline thin films of (C_8O-BTBT-OC_8) (F_4TCNQ) and its blend with PS were prepared by BAMS. The devices exhibited n-type transport, and the films based on blends showed remarkable stability in environmental conditions.

2. To process OSCs at high throughput, it is necessary to use OSCs showing a very high solubility in organic solvents (around 10-20 $mg.ml^{-1}$). Generally,

DNTT functionalized with alkyl chains exhibit limited solubility in common organic solvents. Our research demonstrated that they can be deposited at 10 $mm \cdot s^{-1}$ using BAMS applying high temperatures, although such high temperature has a detrimental impact on the film's homogeneity. By using the S-shaped π-core derivative S-DNTT-10 higher solubility is achieved, allowing for the material processing at lower coating temperatures. This results in smoother films and OFET mobility values nearly two orders of magnitude higher (2.1 $cm^2 \cdot V^{-1} \cdot s^{-1}$) compared to alkylated linear DNTT derivatives. Therefore, through molecular design, the processing of OSCs and the electrical performance of OFETs can be significantly improved.

3. Controlling polymorphism in OSCs is key to realise reproducible and high performing devices. Temperature is an appealing tool that can be exploited to modulate the OSCs crystal structure. Here, extensive studies have been conducted on the p-type OSC Ph-BTBT-10. X-ray reflectivity (XRR) data at various temperatures revealed the presence of single layer, bilayer, and SmE phases. Single-layer thin films were obtained via physical vapor deposition. These films were subsequently annealed to transform them into the bulk bilayer form. The data indicated that films annealed at 140 ºC fully transitioned to the bilayer structure, whereas those annealed at 130 ºC retained some single-layer phase. OFET devices based on these evaporated Ph-BTBT-10 thin films showed enhanced mobility and reduced charge traps after post-annealing, with the highest mobility observed in the fully bulk phase transformed films.

4. In parallel, solution-processed thin films of Ph-BTBT-10 and Ph-BTBT-10:PS were deposited using the BAMS technique at a rate of 10 $mm \cdot s^{-1}$ and coating temperatures ranging from 85 °C to 120 °C to study the impact on crystal structure and electrical performance. AFM and XRR analysis pointed out that

disordered bulk phase is formed in the films coated at lower temperatures (85-105°C). However, above 110°C the single-layer structure becomes more dominant. Electrical characterization under ambient conditions demonstrated that the OFET mobility increased with temperature, achieving the highest mobility at 120 °C. This suggested that the film molecular order might be playing a crucial role in these films, rather than the crystal phase. Further XRR analysis of thin films of Ph-BTBT-10 and Ph-BTBT:PS deposited at 120 °C and annealed at the same temperature, revealed that the annealing process caused the transition from the single-layer structure to the bilayer phase with a reduced molecular disorder. This more ordered molecular arrangement resulted in a significant improvement in the OFET mobility from 0.26±0.06 $cm^2 \cdot V^{-1} \cdot s^{-1}$ before annealing to 0.40±0.10 $cm^2 \cdot V^{-1} \cdot s^{-1}$ after annealing for the Ph-BTBT-10 films. Remarkably, Ph-BTBT-10 blend devices showed substantial enhancement in mobility and a lower threshold voltage. After annealing, the blend films reached a mobility close to 2 $cm^2 \cdot V^{-1} \cdot s^{-1}$.

Annex: Other contributions

Article IV: Synergistic effect of solvent vapour annealing and chemical doping for achieving high-performance organic field-effect transistors with ideal electrical characteristics

Article V: From synthesis to device fabrication: elucidating the structural and electronic properties of C7-BTBT-C7

Article VI: Impact of hydrophilic side chains on the thin film transistor performance of a benzothieno–benzothiophene derivative